

Gamma-Ray Observations of the Orion Molecular Clouds using the *Fermi* Large Area Telescope

Akira Okumura

Department of Physics, Graduate School of Science
The University of Tokyo

July 2009

Abstract

Gamma-ray diffuse emission above 100 MeV is mainly induced by hadronic interactions between Galactic cosmic rays (CRs) and nuclei of interstellar gas. Thus, diffuse emission from a local giant molecular cloud is thought to be proportional to the CR density, its mass, and the inverse of the square of its distance from the Earth. Indirect measurements of CRs using this emission are expected to bring us important information of Galactic CRs distribution outside the Solar system. This is because charged particles lose their positional information during their propagation in the Galaxy before reaching the Earth, and therefore, only observations of diffuse gamma rays enable us to study Galactic CRs remotely. Preceding observations of the diffuse emission by the EGRET revealed that the Galactic plane and molecular clouds are indeed bright with GeV gamma rays. However, the observed gamma-ray spectra from the gases could not be explained by an emission model expected from the CR spectra directly observed at the Earth. As a result, the emission mechanism of diffuse gamma-ray emission has been a mystery since the EGRET era. The Large Area Telescope (LAT) onboard the *Fermi Gamma-ray Space Telescope (Fermi)* launched in June 2008, is an excellent tool to study the diffuse emission, because it has wider field of view, larger effective area, wider energy band, and better angular resolution than those of the EGRET. Thus we are now able to study the diffuse emission from interstellar medium with unprecedented photon statistics, and to study the spatial structure of molecular clouds. We analyze the first 9 months of observations with *Fermi*/LAT on the Orion A and B clouds which are the archetypes of local giant molecular clouds where interstellar gas condenses and stars are formed. We show that diffuse emission from both H I and H₂ gases are well explained by a gamma-ray emissivity model predicted from the CR spectra observed at the Earth. At the same time, we obtain the total masses of the Orion A and B clouds to be $(78.1 \pm 8.4 \pm 4.9) \times 10^3 M_{\odot}$ and $(38.4 \pm 5.8 \pm 2.9) \times 10^3 M_{\odot}$, respectively. We study correlations among the gamma-ray surface brightness of the clouds, CO line observations, and visual extinction by interstellar dust. Nonlinear relations between gamma rays and CO are found in the clouds, which cannot be explained by a uniform CR distribution and a constant conversion factor from CO intensity to $N(H_2)$. On the other hand, the A_V map shows better linear correlations with the observed gamma-ray intensity. A part of our result is interpreted as an existence of a thin and wide gas distribution which is not detected by the CO observations. However, this does not explain the nonlinear correlations in dense gas regions. There remains a possibility that CRs cannot penetrate into the cores of the clouds.

Contents

1 INTRODUCTION	9
2 REVIEW	11
2.1 Cosmic Rays	11
2.1.1 Cosmic-ray flux and spectra	11
2.1.2 Cosmic-ray propagation	13
2.1.3 Cosmic-ray acceleration	15
2.1.4 GALPROP	17
2.2 Interstellar Medium	17
2.2.1 Neutral hydrogen gas (H I)	20
2.2.2 Molecular clouds	20
2.2.3 Interstellar dust	22
2.3 Gamma-Ray Production in Interstellar Environments	23
2.3.1 π^0 gamma rays	23
2.3.2 Electron bremsstrahlung	29
2.3.3 Inverse Compton scattering	29
2.4 The Orion Molecular Clouds	29
2.4.1 The Orion region	29
2.4.2 Molecular masses of the Orion clouds	30
2.4.3 Previous gamma-ray observations and their limitations	32
3 FERMI GAMMA-RAY SPACE TELESCOPE AND THE LARGE AREA TELESCOPE	37
3.1 The History of Gamma-ray Telescopes	37
3.2 <i>Fermi</i> Gamma-ray Space Telescope	38
3.3 The Large Area Telescope	39
3.3.1 An overview	39
3.3.2 Precision converter-tracker	40
3.3.3 Calorimeter	43
3.3.4 Anticoincidence Detector (ACD)	44
3.3.5 Data acquisition and event processing	44
3.3.6 Sensitivity and instrumental performance	49
4 OBSERVATIONS	53
4.1 Observations	53
4.2 Event Selection	53
5 DATA ANALYSIS AND RESULTS	59
5.1 Gamma-Ray Emission Components	59
5.2 Validation of π^0 Emission	60

5.2.1	Gamma-ray emission from H I	60
5.2.2	X_{CO} and gamma-ray spectrum of H ₂	66
5.2.3	Summary of the simple analysis	72
5.3	Emission Models	73
5.4	Analyses of the Orion Clouds	74
5.4.1	Extraction of the Clouds	75
5.4.2	The Energy Spectra and Total Masses of the Orion A and B Clouds	78
5.4.3	Correlation with CO	78
5.4.4	Correlation with Dusts	83
5.5	The Maximum Likelihood Analysis	88
5.5.1	<i>Science Tools</i> and <i>gtlike</i>	90
5.5.2	<i>gtlike</i> results on ROI 2	90
5.5.3	Attempts of model improvement	93
5.5.4	Summary of the <i>gtlike</i> analysis	94
5.5.5	Significance map	96
6	DISCUSSION	99
6.1	Cosmic Rays and π^0 Gamma Rays	99
6.1.1	Diffuse gamma-ray spectra of H I and H ₂ gases	99
6.1.2	CR flux in the Orion region	99
6.2	Total Masses of the Orion Molecular Clouds	100
6.3	Nonlinear Relation between CO and Gamma-Ray Intensities	101
6.3.1	CO vs. A_V	102
6.3.2	Point source contribution	102
6.3.3	Nonuniformity of Cosmic Rays	102
7	CONCLUSION	107
Appendix		109
A	Kinematics	109
A.1	Threshold kinetic energy for pion production	109
A.2	Gamma-ray energy distribution in π^0 decay	109
B	Maximum Likelihood Method	110
C	Results of <i>gtlike</i>	111
Acknowledgement		119
References		120

List of Figures

2.1	The spectrum of cosmic rays observed at the Earth	12
2.2	Cosmic-ray proton and alpha-particle spectra	13
2.3	Cosmic-ray electron and positron spectra	14
2.4	TeV gamma-ray and X-ray images of RX J1713.7-3946	16
2.5	A schematic view of diffusive shock acceleration	16
2.6	A multiwavelength view of the Milky Way	19
2.7	Schematic view of a photodissociation region	21
2.8	The distribution of molecular clouds in the Solar vicinity	22
2.9	Schematic shapes of the π^0 -decay gamma-ray spectrum.	24
2.10	The cross section of p-p collision	26
2.11	Comparison of gamma-ray emissivity models	27
2.12	Multiwavelength view of the Orion region	31
2.13	Gamma-ray intensity maps of the Orion region obtained by <i>COS-B</i> and the EGRET . . .	33
2.14	The energy spectra of diffuse gamma-ray emission from the Galactic plane	34
2.15	Gamma-ray emissivity of the Orion region	35
3.1	The 3rd EGRET catalog	38
3.2	An artist's impression of <i>Fermi Gamma-ray Space Telescope</i> in orbit	39
3.3	The LAT all sky image taken during the first 3 months	40
3.4	A schematic view of the LAT	41
3.5	The LAT Tracker	42
3.6	A schematic view of a LAT tracker tray	42
3.7	A schematic view of the LAT calorimeter module	43
3.8	A schematic view of the LAT Anticoincidence Detector	44
3.9	A schematic view of the LAT data acquisition system	45
3.10	Event examples	47
3.11	The residual background induced by cosmic rays	48
3.12	The LAT responses	50
3.13	Expected LAT source sensitivities for exposures on various timescales	51
4.1	A schematic view of the scanning mode of <i>Fermi</i>	54
4.2	The pointing history of the LAT between MET=245000000 and 247000000	54
4.3	The exposure map of the Orion region in an energy range of 3.56 GeV – 4.74 GeV . . .	55
4.4	Zenith angle dependence of the Earth-albedo gamma-ray counts	56
4.5	A gamma-ray count map of ROI 1	57
4.6	A gamma-ray count map of ROI 2	57
5.1	Masked count maps of ROI 2	61
5.2	Rebinned count maps	62
5.3	Rebinned H I maps after weighting by exposure	63

5.4	Masked maps of W_{CO} and H I	64
5.5	Gamma-ray counts versus expected emission from H I gas plus background	65
5.6	The observed gamma-ray emissivity of H I and H ₂ gas	67
5.7	The obtained isotropic component	68
5.8	The extracted H ₂ emission map	69
5.9	Rebinned W_{CO} maps after weighting by exposure	70
5.10	Correlations between W_{CO} and gamma-ray count	71
5.11	Observed and modeled gamma-ray intensity maps above 200 MeV	76
5.12	Observed and modeled gamma-ray intensity maps above 1 GeV	77
5.13	CR proton and alpha-particle spectra ($\times 10$) predicted by GALPROP model selected Galactic locations	79
5.14	Gamma-ray spectra of the Orion clouds	80
5.15	Comparison of the observed and simulated gamma-ray maps in energies between 200 MeV and 20 GeV	81
5.16	Correlation between observed intensity and a CO model above 200 MeV	82
5.17	Same as Figure 5.15, but in energies above 1 GeV	84
5.18	Same as Figure 5.16, but in energies above 1 GeV	84
5.19	Correlation between observed intensity and a CO model above 1 GeV	85
5.20	Same as Figure 5.16, but in energies between 200 MeV and 1 GeV	86
5.21	Gamma-ray intensity and dust maps	87
5.22	Correlations between the observed gamma-ray intensity and A_V	88
5.23	Same as Figure 5.22, but fitted with quadratic functions	89
5.24	Results of the <i>gtlike</i> analysis of the data set 2, using the model “54_77Xvarh7S”	92
5.25	The total count spectrum of the data set 2, compared with the best-fit model including “54_77Xvarh7S”	93
5.26	Effects of the assumed spin temperature T_s on the derived H I map	95
5.27	The significance map of the Orion A ₊ region in the 0.25° grid	97
6.1	A comparison of gamma-ray emissivity of H I and H ₂ gases between EGRET and LAT .	100
6.2	X-ray observations of the Orion region	103
6.3	The observed gamma-ray count map using only “thin”-layer events of the energies above 1 GeV	105
C.1	Results of the <i>gtlike</i> analysis of the data set 2, using the model “54_78Xvarh7O”	112
C.2	Results of the <i>gtlike</i> analysis of the data set 2, using the model “54_78Xvarh7O”	113
C.3	The total count spectrum of the data set 2, compared with the best-fit model including “54_78Xvarh7O”	114
C.4	The total count spectrum of the data set 2, compared with the best-fit model including “54_78Xvarh7O”	114
C.5	Results of the <i>gtlike</i> analysis of the data set 2, using the model “54_78Xvarh7O_Ts100” .	116
C.6	Results of the <i>gtlike</i> analysis of the data set 2, using the model “54_78Xvarh7O_Ts100000”	117
C.7	The total count spectrum of the data set 2, compared with the best-fit model including “54_78Xvarh7O_Ts100”	118
C.8	The total count spectrum of the data set 2, compared with the best-fit model including “54_78Xvarh7O_Ts100000”	118

List of Tables

2.1	Properties of ISM	18
2.2	Decay modes of pions and muons	24
2.3	π^0 gamma-ray contributions from CR α and ISM He	28
2.4	The distance to the Orion nebula	32
2.5	The masses of the Orion molecular clouds	32
3.1	Comparison of gamma-ray telescopes	37
3.2	LAT and GBM	38
3.3	The LAT components	40
3.4	Summary of instrumental performance of LAT	49
4.1	The criteria of event selections	56
5.1	Gamma-ray emission components	60
5.2	The observed gamma-ray emissivity of H I gas	66
5.3	Estimated X_{CO}	67
5.4	Parameters for different GALPROP models	74
5.5	The mass of the Orion clouds	79
5.6	Correlation slopes between observed intensity and a CO model above 200 MeV	83
5.7	Same as Table 5.6, but only using events of with energies above 1 GeV	85
5.8	Same as Table 5.7, but using equation (5.16)	86
5.9	Correlation slopes between the observed gamma-ray intensity and A_V	89
5.10	A likelihood result of “54_77Xvarh7S”	91
5.11	A likelihood result of “54_78Xvarh7O”	94
5.12	A likelihood result of “54_78Xvarh7O”	94
5.13	Summary of <i>gtlike</i>	96
6.1	A comparison of the total masses of the Orion A and B clouds obtained by several authors	101
6.2	Comparison of X_{CO}	101
C.1	A likelihood result of “54_78Xvarh7O_Ts100”	115
C.2	A likelihood result of “54_78Xvarh7O_Ts100000”	115

Chapter 1

INTRODUCTION

Diffuse emission of > 100 MeV gamma rays in the Galaxy is mainly induced by hadronic interactions between cosmic rays (CRs) and interstellar matter (ISM), via the productions of π^0 particles and their subsequent decay into photons. This emission can be used to study the structure of ISM and the Galactic distribution of cosmic rays, because its emissivity can be written as the product of the CR flux and the density of ISM, and its spectral index above 1 GeV is thought to trace that of parental CRs. Thus, observations of diffuse gamma-ray emission are expected to enable us to study the flux and spectrum of Galactic CRs at the location of the emission, while direct measurements of CRs at the Earth cannot extract their positional information which is already lost during propagation in the interstellar magnetic fields of the Galaxy.

The CR spectra and fluxes ever observed at the Earth are believed to give us a correct estimate of those of the Galaxy. Thus diffuse gamma-ray emission should be explained by a π^0 emission model and observed CR spectral index (~ 2.7). However, the EGRET studies on diffuse emission from the Galactic plane ($|b| < 10^\circ$) revealed that its spectral shape above ~ 1 GeV was not explained by a π^0 model and the observed CR spectra at the Earth (Hunter et al., 1997). This mystery is referred to as “GeV excess”. The diffuse emission from nearby giant molecular clouds (GMCs) also exhibited similar spectral shape, while the photon statistics of the observations was not adequate enough (Digel et al., 1999; Aharonian, 2001). Many authors discussed on this mystery and proposed a number of “solutions”: signature of dark matter annihilation (de Boer et al., 2005), variations of CR spectra outside the Solar vicinity (Strong et al., 2000; Porter & Protheroe, 1997), contributions by unresolved point sources (Berezhko & Volk, 2004), and miscalibration of the instrument (Moskalenko et al., 2007).

The recent progress in gamma-ray detection technique has changed this situation. The Large Area Telescope (LAT) onboard the *Fermi Gamma-ray Space Telescope* was newly launched in June 2008. It has a wider energy band, a larger effective area, a wider field of view, and better angular resolution than those of the EGRET (Atwood et al., 2009). Among many scientific objectives of the LAT, a study of the diffuse gamma-ray emission is one of its primary targets. Its unprecedented gamma-ray sensitivity enables us to study the Galactic CRs and ISM in detail. Observations of the GMCs in the Solar neighborhood, such as the Orion molecular clouds, are suitable for this study, because nearby GMCs contain vast mass working as the target of CR collisions, and their large apparent sizes ($\sim 10^\circ$) enable us to study the structure of the clouds.

Orion A and B are typical GMCs containing many dense cores where stars are formed. They are located about 400 pc away from the Sun, and their total mass is estimated to be of the order of $10^5 M_\odot$ (Wilson et al., 2005). Their structure, physical and chemical properties have been extensively studied using emission lines in the radio band (e.g. Wilson et al., 1970), and dust observations using infrared emission or star light extinction (e.g. Schlegel et al., 1998; Dobashi et al., 2005). However, their total masses and density distribution, the most basic properties of GMCs, have been calculated by an empirical conversion factor X_{CO} which relates the velocity-integrated CO intensity W_{CO} to the H₂ column density

$N(H_2)$. This is because H₂ and He, the main components of GMCs, cannot be observed directly.

Galactic scale variation and galaxy-by-galaxy variation of X_{CO} due to metallicity differences are already known from radio and gamma-ray observations (Wilson, 1995; Arimoto et al., 1996; Strong et al., 2004b). A nonlinear relation between W_{CO} and dust maps was also discussed (Boulanger et al., 1998). However, X_{CO} and the CO line are still widely used in studying the structure of GMCs. This is because the CO line is one of the most bright radio lines emitted from GMCs, and the angular resolution of radio telescopes is enough to resolve internal structure of GMCs. Since infrared emission from GMCs is known to be affected by their temperature, the CO line is still keeping its established position as a “mass tracer”.

On the other hand, high-energy gamma-ray emission can be used to study the masses of GMCs as mentioned above, with an assumption of CR fluxes and the distances to the clouds. The advantage of π^0 gamma-ray observations in studying GMCs is that its production rate is not affected by gas temperature or formation/excitation of CO molecules. Indeed, diffuse gamma-ray observations of the Orion clouds were performed by *COS-B* and EGRET (Caraveo et al., 1980; Bloemen et al., 1984; Digel et al., 1995, 1999). However, the two clouds were not resolved due to their limited photons statistics and low angular resolution. In addition, the mystery of gamma-ray emission mechanism itself remained.

In the present thesis, we analyze the diffuse GeV gamma-ray emission from the Orion region obtained by the LAT, and conduct the following studies.

1. We precisely measure the gamma-ray spectra from H I gas and the Orion clouds. We settle the problem of “GeV excess” by comparing the observed spectra with a model calculation expected from radio observations, CR measurements, and a π^0 model.
2. Using the above result, we estimate the CR flux at the location of the Orion clouds. The results enable us to measure the CR spectrum and flux at a specific Galactic location away from the Earth.
3. Extracting the gamma-ray emission associated with the Orion A and B clouds, we estimate the total masses of the clouds.
4. We study the correlations among gamma-ray surface brightness, a CO intensity map, and a visual extinction map to study the distributions of molecular gas and CRs in the region.

Chapter 2

REVIEW

Charged cosmic-ray (CR) particles are deflected by interstellar magnetic fields, and hence their positional information is lost during propagation. In order to study CRs at their acceleration sites, and outside the vicinity of the Earth, indirect measurements using neutral secondary particles, energetic photons in particular, are needed. Among them, of particular importance are GeV¹ gamma rays induced by interactions between CRs and interstellar medium (ISM). We review CRs in Section 2.1, ISM in Section 2.2, and gamma-ray production processes in Section 2.3. The Orion molecular clouds, the target object studied in the present thesis, is also summarized in Section 2.4.

2.1 Cosmic Rays

Cosmic rays (CRs), namely energetic particles traveling through space at speeds approaching almost that of light, were first discovered by Victor Heß using a balloon experiment in 1912 (Hess, 1912). Since then, CRs have been extensively studied for 100 years through both experimental and theoretical approaches. However there are still long-standing and fundamental questions about CRs, since the time of their historical discovery; “where do they come from?” and “how are they accelerated?” One of the greatest difficulties in trying to answer these questions is that the arrival directions of CRs do not keep the directional information about their origin. This is because interstellar magnetic fields have a typical strength of the order of $1 \mu\text{G}$ (Heiles, 1976), and thus the gyroradius of a 1 TeV CR proton is $\sim 10^{-3} \text{ pc}$ which is much smaller than the Galactic scale ($\sim 1 \text{ kpc}$). The magnetic field is known to be a superimposition of small-scale random component and large-scale structure. The ratio between the two is estimated to be ~ 1 . Since our direct measurements of CRs are limited to the vicinity of the Earth, we do not know the Galactic distribution of CR fluxes, either.

2.1.1 Cosmic-ray flux and spectra

About 10^3 CR particles enter the Earth’s atmosphere per m^2 per second. The observed highest energy of these particles reaches 10^{20} eV (Takeda et al., 2003; Abbasi et al., 2008). Figure 2.1 shows the CR energy spectrum observed at the Earth, ranging from 1 GeV to 100 EeV (Cronin et al., 1997). As the figure shows, the spectrum below 1 PeV follows a power law as $dN/dE \propto E^{-\Gamma}$, with the spectral index $\Gamma \sim 2.7$. Meanwhile, the spectrum above this energy region around 1 PeV (so-called ‘knee’) is described by a softer power law, $\Gamma \sim 3$. These different spectral indices suggest that the origins of CRs are different: CRs below the knee are believed to be accelerated in Galactic objects such as supernova remnants (SNRs), while those above the knee produced by extragalactic accelerators.

About 90% of cosmic rays observed at the Earth are protons, about 9% are alpha particles (helium nuclei), and the rest are heavier nuclei and leptons (Gaisser, 1990). The energy spectra of these CR com-

¹keV (10³ eV), MeV (10⁶ eV), GeV (10⁹ eV), TeV (10¹² eV), PeV (10¹⁵ eV), EeV (10¹⁸ eV).

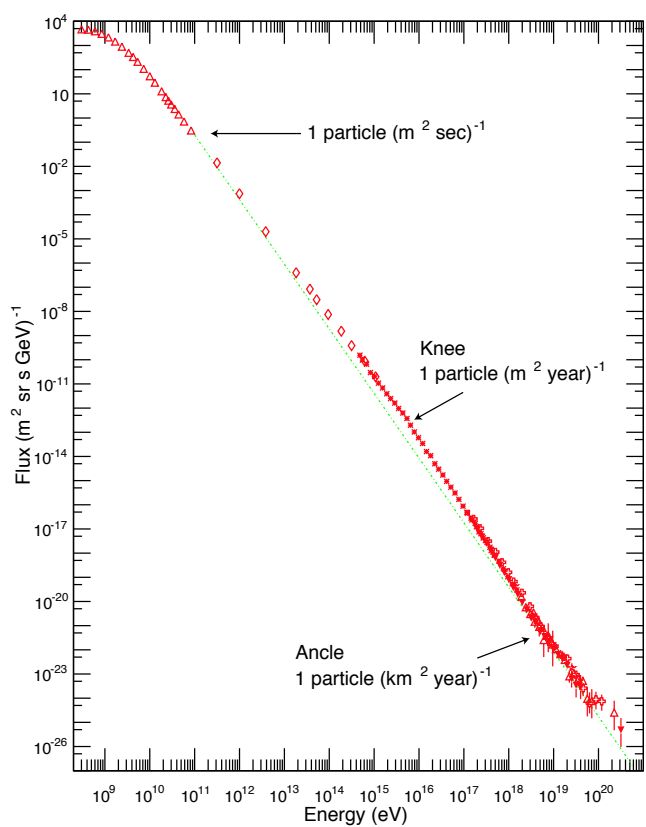


Figure 2.1: The spectrum of cosmic rays observed at the top of the Earth's atmosphere (Cronin et al., 1997). All cosmic-ray species are plotted together.

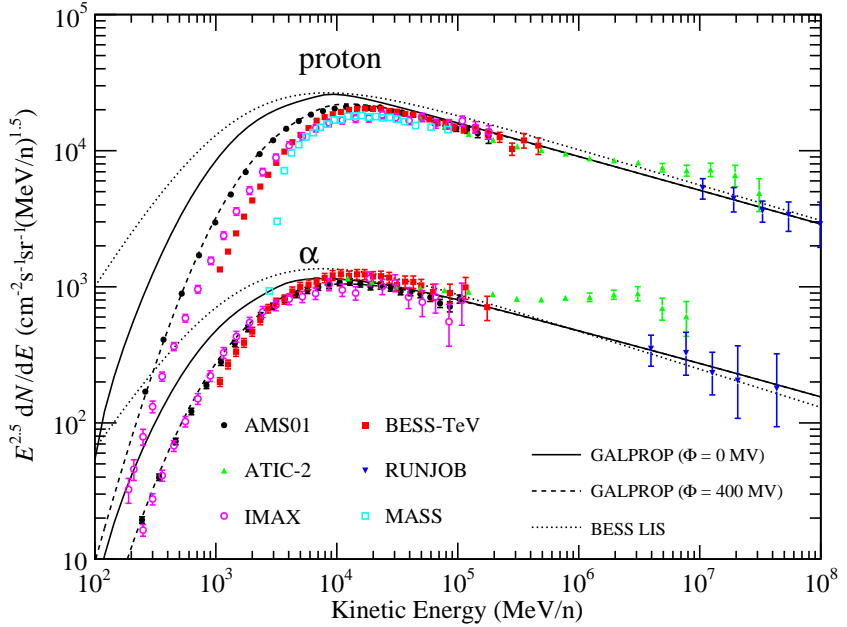


Figure 2.2: CR proton and alpha-particle spectra observed by several experiments; the AMS experiment (black filled circles; Alcaraz et al. 2000a,b), the BESS experiment (red filled rectangles; Haino et al. 2004), the ATIC-2 experiment (green upward triangles; Panov et al. 2007), the RUNJOB experiment (blue downward triangles; Apanasenko et al. 2001), the IMAX experiment (purple open circles; Menn et al. 2000), and the MASS experiment (light blue open rectangles; Bellotti et al. 1999). Solid lines are CR spectra adopted by GALPROP for a Galactic location of $(R, Z) = (8.5 \text{ kpc}, 0 \text{ kpc})$. Dashed lines are the same as the solid ones, but the effect of solar modulation is taken into account. Local interstellar spectra (LIS) “demodulated” from the BESS observations (Shikaze et al., 2007) are also shown with dotted lines.

ponents have been measured by various experiments at the Earth. Some results from those experiments are plotted in Figure 2.2 (hadronic components) and 2.3 (leptonic components). The figures clearly show three important features. First, the power law indices of CR proton and alpha spectra are about 2.7 in the energy range above 10 GeV. Second, that of CR electrons is about 3. The last is that all species have cutoffs below 10 GeV.

2.1.2 Cosmic-ray propagation

The spectral shape of CRs are determined through the processes of CR acceleration and propagation. The propagation part can be written in the following transport equation regardless of the CR origin (Strong & Moskalenko, 1998);

$$\frac{\partial \psi}{\partial t} = q(\vec{r}, p) + \vec{\nabla} \cdot (D_{xx} \vec{\nabla} \psi - \vec{V} \psi) + \frac{\partial}{\partial p} \left[p^2 D_{pp} \frac{\partial}{\partial p} \left(\frac{1}{p^2} \psi \right) \right] - \frac{\partial}{\partial p} \left[\dot{p} \psi - \frac{p}{3} (\vec{\nabla} \cdot \vec{V}) \psi \right] - \frac{1}{\tau_f} \psi - \frac{1}{\tau_r} \psi. \quad (2.1)$$

Here p is the particle momentum, $\psi = \psi(\vec{r}, p, t)$ is the CR density per unit particle momentum, while \vec{r} and t are position vector and time, respectively. The first term q denotes CR sources. The second is the diffusion term described by a spatial diffusion coefficient D_{xx} and a convection velocity \vec{V} , while the third term that in the momentum phase space. The fourth term describes the energy loss caused by, for

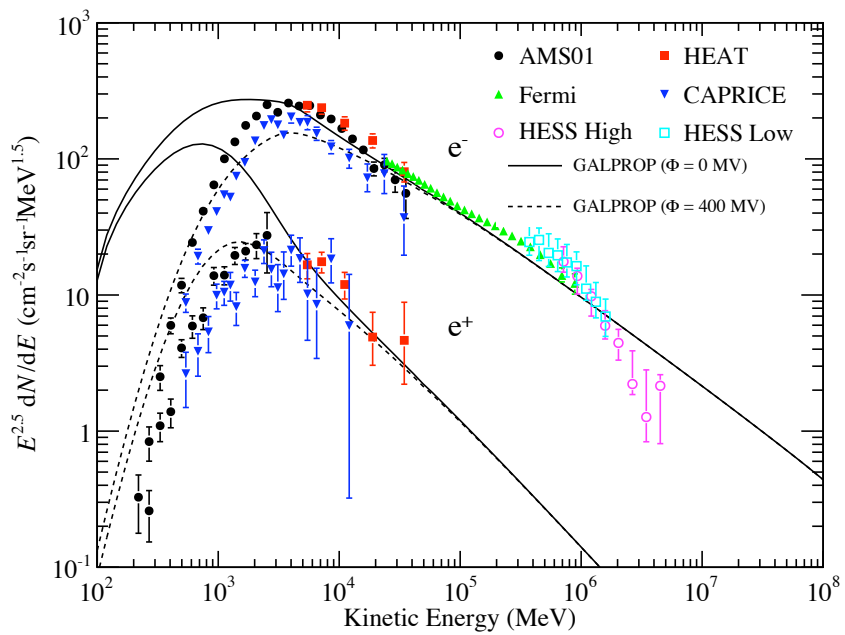


Figure 2.3: CR electron and positron spectra observed by several experiments; the AMS experiment (black filled circles; Alcaraz et al. 2000c), the HEAT experiment (red rectangles; Barwick et al. 1998), the *Fermi*/LAT (green upward triangles; Abdo et al. 2009d), the CAPRICE experiment (blue downward triangles; Boezio et al. 2000), the high-energy analysis of the HESS experiment (purple open circles; Aharonian et al. 2008), and the low-energy analysis of the HESS experiment (light blue open rectangles; Aharonian et al. 2009). The latter three data include positron flux.

example, synchrotron radiation, and by adiabatic particle deceleration. The last two terms denote nuclear fragmentation and radioactive decay processes, respectively, where τ_f and τ_r are their timescales. By solving equation (2.1) for each CR component, the interstellar CR flux can be derived with appropriate assumptions on many parameters, such as the diffusion coefficients and the source spectra. For example, a computer program called GALPROP² (Subsection 2.1.4) calculates the equation in Galactocentric cylindrical space and gives numerical CR flux models at arbitrary places in the Galaxy.

The CR spectra which have ever been observed are spatially limited to the vicinity of the Earth orbit, except for the Voyager 1 observations (Stone et al., 2005). It is unknown whether the measured CR fluxes and spectra represent those in typical interstellar environments. Their measured properties are also affected by the solar wind which varies with a period of about 11 years (see the fourth term in equation (2.1)). This is referred to as solar modulation. Its effect on the CR proton spectra can be seen in Figure 2.2 in the energy range below 10^4 MeV, where spectral shapes obtained by various experiments differ. As the solar activity becomes higher, more enhanced solar winds sweep out these low-energy CRs, and prohibit them from entering the heliosphere. Gleeson & Axford (1968) constructed a simplified model of the solar modulation under “force-field approximation”, by introducing an electronic potential Φ which reduces the total energy of a CR particle according to its charge. For example, in the case of $\Phi = 400$ (MV), an alpha particle with the kinetic energy of 10 GeV, will reduce its energy to 9.2 GeV ($= 10 \text{ GeV} - 400 \text{ MV} \times 2 \times e$). As shown in Figures 2.2 and 2.3, GALPROP can successfully reproduce the solar modulation.

2.1.3 Cosmic-ray acceleration

Then what is the origin of the source term $q(\vec{r}, p)$ in equation (2.1)? Galactic CRs, or CRs in the energy range below the knee, are widely believed to be accelerated by shock waves at the outer front of expanding SNRs (Hillas, 2005). Ginzburg & Syrovatskii (1964) pointed out that the radio emission from SNRs could be explained by CR acceleration inside them. As shown in Figure 2.4, recent observations of SNRs by X-rays (Koyama et al., 1995; Uchiyama et al., 2007) and TeV gamma rays (Aharonian et al., 2004; Naumann-Godó et al., 2008) both support the idea of the acceleration of high-energy CRs, electrons at least, in the shell of SNRs. However, conclusive evidence of the acceleration of hadronic components has not been observed yet except for a several suggestive materials by keV to TeV observations (Esposito et al., 1996; Uchiyama et al., 2007; Aharonian et al., 2007).

The actual mechanism of CR acceleration is a fundamental issue in the CR study. Although ground-based particle accelerators utilize direct electromagnetic acceleration mechanisms, those in cosmic sources are considered to be dominated by so-called “first-order Fermi acceleration”³. Blandford & Ostriker (1978) and Bell (1978) independently proposed theories of particle acceleration mechanism at strong shock waves, called “diffusive shock acceleration”. As shown in Figure 2.5, The basic idea is that a charged particle is reflected by magnetic fields (MHD waves) between the “upstream” and “downstream” domains of a shock front, and gains energy repeatedly. The upstream and the downstream have different velocities v_1 and v_2 ($v_1 > v_2$), respectively. Thus, if the particle is reflected on both sides elastically, its total energy is increased. It is known that the relative gain in one round trip is given by $1 + 4V/3c$, where V is $v_1 - v_2$ and c is the speed of light.

In SNRs which are believed to be one of the major CR sources, diffusive shock acceleration is thought to be taking place at the shock front called a blast wave, which propagates into the surrounding ISM. In this scheme, leptonic and hadronic particles pre-accelerated in a supernova explosion are efficiently accelerated, leading to energetic photon production as shown in figure 2.4. It is believed that the spectral

²http://galprop.stanford.edu/web_galprop/galprop_home.html

³As the name indicates, the original acceleration mechanism, now referred to as “second-order Fermi acceleration”, was proposed by Fermi (1949). He considered collisions between charged particles and moving magnetic fields inside interstellar gas. His theory naturally explained the power-law shapes of CR spectra. However it was not efficient enough to accelerate CRs in a limited time scale.

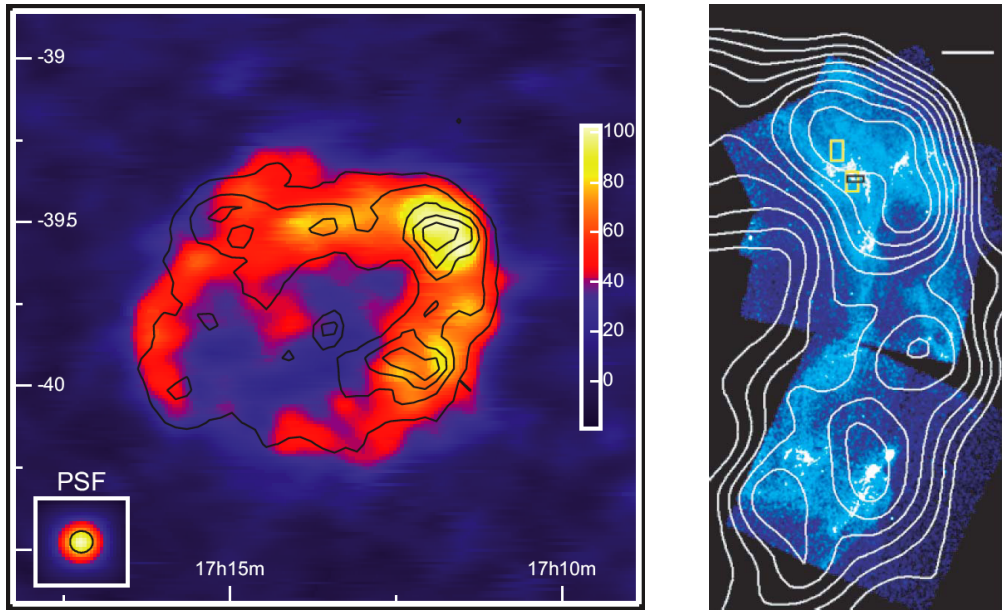


Figure 2.4: TeV gamma-ray and X-ray images of RX J1713.7-3946. (Left) A TeV gamma-ray image observed by the HESS telescope (Aharonian et al., 2007). (Right) An X-ray image obtained by the *Chandra* satellite (Uchiyama et al., 2007).

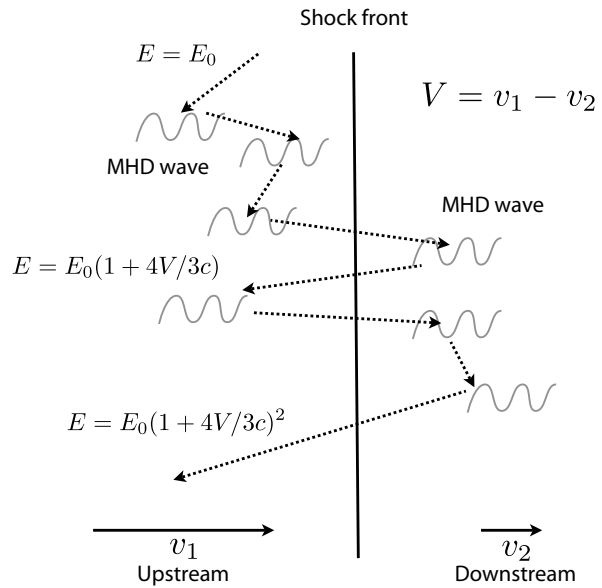


Figure 2.5: A schematic view of diffusive shock acceleration (Uchiyama, 2003, with modification).

indices of these particles become ~ 2 , and they become softer during propagation. However direct observation of hadronic acceleration at SNRs is not achieved yet.

The biggest problem in searching for the cosmic hadron accelerators is that a proton has a much lower efficiency of directly emitting photons than an electron, due to its much higher mass. As a result, a “hadronic channel” becomes an extremely important process through which photons are produced from CR protons. This occurs when CR protons collide with interstellar medium and produce π^0 and π^\pm particles. Among them, π^0 ’s immediately decay into two gamma-ray photons (Subsection 2.3.1), which in turn are observable by gamma-ray detectors which are sensitive in the MeV–TeV energy band. As a result, the *Fermi*/LAT (Chapter 3) is expected to provide a major step forward in our search for the cosmic hadron accelerators, and our attempt of clarifying the Galactic distribution of CRs (Funk, 2008).

2.1.4 GALPROP

GALPROP is a computer program which numerically solves the transport equation, eq (2.1), all over the Galaxy with given parameters such as the diffusion coefficients and CR injection spectra (Strong & Moskalenko, 1998). Some of its “solutions” have been already shown in Figures 2.2 and 2.3. In this Subsection we briefly explain GALPROP, as we use it in our analysis (Chapter 5).

The main purpose of GALPROP is to provide all CR spectra at any arbitrary location of the Galaxy. As a by-product, the spectra of secondary gamma rays and radio emission are also calculated. They are numerically obtained by solving equation 2.1, but the solution is not trivial and strongly depends on many parameters such as diffusion coefficient and primary CR injection spectra. These parameters can be adjusted by users but should be constrained by physical considerations. For example, the calculated CR spectra are required to reproduce those observed at the Earth. Consistency between the calculated and observed CR metal abundances and spectral indices is important in validating the assumed diffusion coefficient. Comparison between continuum synchrotron radiation observed by radio telescopes and that of GALPROP derived from “solved” electron spectra will constrain primary and secondary electron fluxes. In addition, an all-sky GeV gamma-ray map, combined with GALPROP simulations, has a potential to constrain the CR distribution in the Galaxy.

When running GALPROP, we divide the Galaxy into 2D or 3D grids. In the former case, each grid point is parametrized by cylindrical coordinates (R, Z) , while Cartesian coordinates (x, y, z) in the latter case. Usually grid steps for R and Z are $\Delta R = 1$ kpc and $\Delta Z = 0.1$ kpc, respectively. Nucleon species from H to Ni are taken into account, and are converted into other nuclei through nuclear fragmentation and radioactive decay. After repeating calculations over specified time steps, CR densities in equilibrium are “collide”d with interstellar medium (H I, H₂) or interstellar radiation fields (visible, infrared, and cosmic microwave background). Then finally, we can obtain predictions for MeV–GeV gamma-ray emission and synchrotron radiation.

2.2 Interstellar Medium

Interstellar medium (ISM) is a general term denoting diffuse gaseous materials distributing throughout the Galaxy, which consist of hydrogen (H; 70%), helium (He; 28%), and heavier nuclei (“metal”; the rest) in mass. The total ISM mass is thought to contribute $\sim 10\%$ to the overall Galaxy mass. ISM is the target of cosmic-ray interactions from the point of view of gamma-ray astrophysics. As classified in Table 2.1, the ISM is found in several different forms ; cold and warm neutral atomic gas, molecular gas, warm and hot ionized gas, and dust, depending on its density and temperature (Ferrière, 2001). Figure 2.6 shows the ISM distribution in the Galactic plane viewed in different wavelengths. Since molecular gas and cold atomic gas contain a large amount of dust inside them, they obscure the light from background stars as shown in Figure 2.6a, and is also called “dark clouds”. As shown in Figure 2.6b, neutral atomic gas is observed by 21 cm radio line emitted by neutral hydrogen gas. Molecular gases are thought to

Table 2.1: Properties of different components of the ISM (Ferrière, 2001). T is the temperature, n is the density of H nuclei near the Sun, Σ_\odot is the azimuthally averaged mass density per unit area at the solar circle, and \mathcal{M} is the mass contained in the entire Galaxy.

Component	T (K)	n (cm^{-3})	Σ_\odot ($M_\odot \text{ pc}^{-2}$)	$\mathcal{M}(10^9 M_\odot)$
Molecular	10–20	10^2 – 10^6	~ 2.5	~ 1.3 – 2.5
Cold atomic	50–100	20–50	~ 3.5	
Warm atomic	6000–10000	0.2–0.5	~ 3.5	$\} \gtrsim 6.0$
Warm ionized	~ 8000	0.2–0.5	~ 1.4	$\gtrsim 1.6$
Hot ionized	$\sim 10^6$	~ 0.0065		

be traced by 115 GHz radio line emitted by carbon monoxide molecules (Figure 2.6c). The ISM dust is optical thick and thus is traced by “visual extinction” as shown in Figure 2.6d. The hot ionized ISM component is observable in X-rays. All those ISM components contribute to the gamma-ray emission (Figure 2.6e), with the emissions basically proportional to the mass density times the CR flux.

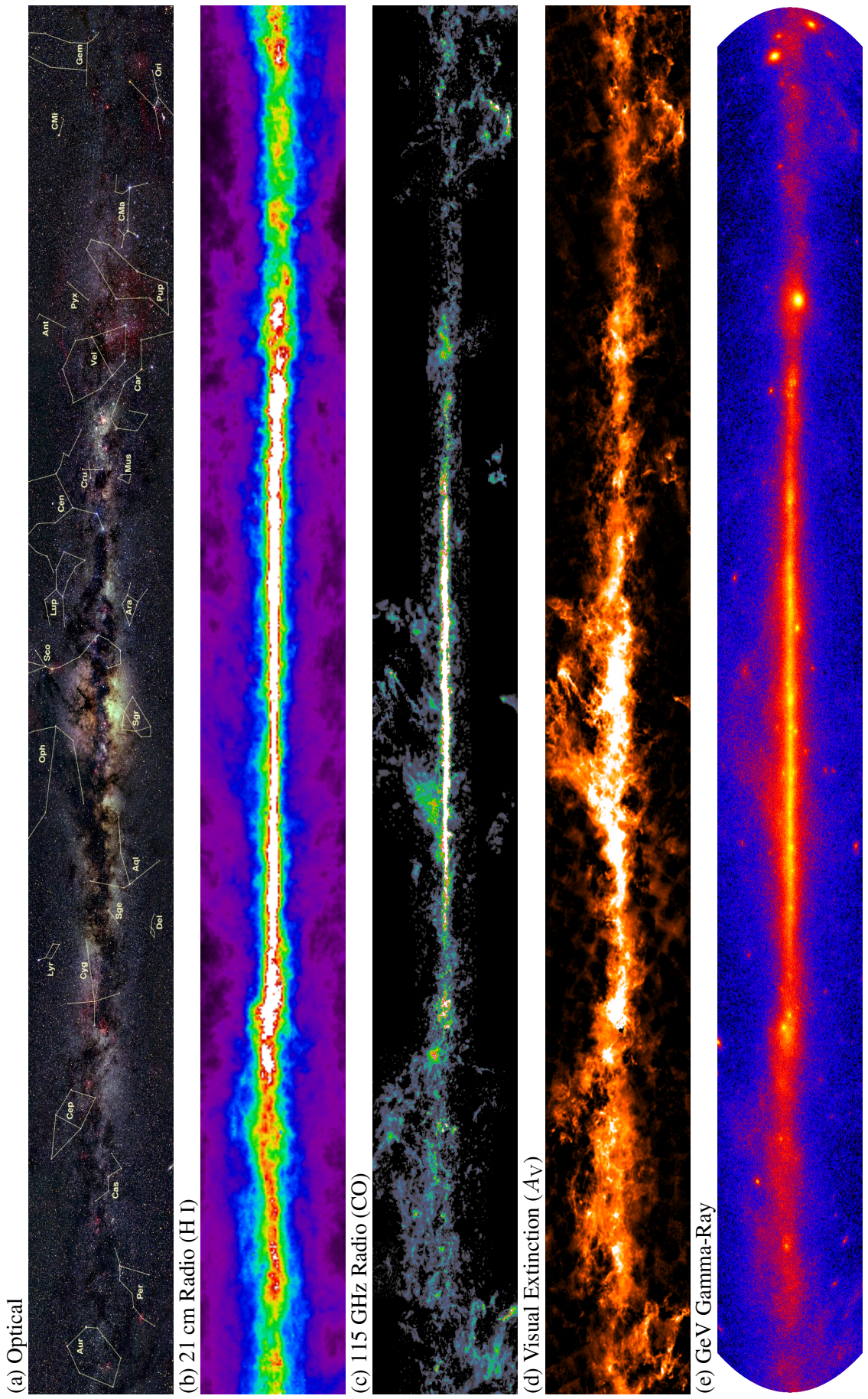


Figure 2.6: A multiwavelength view of the Milky Way. (a) An optical mosaic image on which major constellations are indicated (Mellinger, 2008). The Orion constellation is located at the bottom right. (b) A 21 cm radio image corresponding to the H I distribution (Kalberla et al., 2005). (c) A 115 GHz radio image representing the distribution of CO (Dame et al., 2001). (d) A map of visual extinction, revealing distribution of dust (Dobashi et al., 2005). (e) The 200 MeV – 300 GeV *Fermi*/LAT gamma-ray image.

2.2.1 Neutral hydrogen gas (H I)

One of the major components of the ISM is neutral atomic gas including H, He and metals; these are referred to as H I regions. As the name indicates, these regions are dominated by neutral hydrogen atoms (H I), which are observable by 21 cm radio line from ground. Since the first discovery of the line from space (Ewen & Purcell, 1951; Muller & Oort, 1951), H I emission has been widely and extensively used as a probe to study the structure of the Milky Way Galaxy and other galaxies. Figure 2.6b shows the Galactic-plane map of H I gas observed by the Leiden-Argentine-Bonn (LAB) survey (Kalberla et al., 2005), which is the most recent all-sky survey of H I gas. The results of different radio telescopes have been merged into the all-sky data. Since the beam sizes of the telescopes are similar ($\sim 0.6^\circ$), the data quality of the survey is almost uniform throughout the sky.

A neutral hydrogen atom consists of a proton and an electron, both having spin of $\frac{1}{2}$. The electron spin interacts with the magnetic field induced by the magnetic momentum of the proton. As a result, the energy level of the electron is split into two states according to the direction of the electron and proton spins. This mechanism is called hyperfine structure. The hyperfine energy split of an atomic hydrogen in the ground state is

$$\Delta E \simeq 5.9 \times 10^{-6} \text{ eV}, \quad (2.2)$$

which is equivalent to a frequency of 1420 MHz; this is the 21 cm radio line. This line emission has two advantages in studying the structure of the Galaxy. First, the line is narrow. The width due to the uncertainty principle (natural width) is $\sim 10^{-20}$ km/s, and the Doppler width of gas at a temperature of 100 K is ~ 1 km/s; both are low enough compared to the speed of the Galactic rotation ranging from ~ 10 to ~ 200 km/s. Second, it can penetrate the depths of a few kpc, since the line is optical thin outside the Galactic plane ($|b| > 10^\circ$). Therefore the 3D structure of the Galaxy can be reconstructed from observations of the 21 cm line, upon assumptions of the position of the solar system and the Galactic rotation velocity (e.g. Nakanishi & Sofue 2003).

The observed brightness temperature $T_b(v)$ of a gas at a line-of-sight velocity v is given by

$$T_b(v) = [T_s(v) - T_{\text{bg}}] \left[1 - e^{-\tau(v)} \right], \quad (2.3)$$

where T_s is the spin temperature which is equal to the gas kinetic temperature in most cases, $\tau(v)$ is the optical depth, and T_{bg} is that of the cosmic microwave background which is 2.66 K at 21 cm (Dickey & Lockman, 1990). T_s varies around 100 K depending on the location of gas, and is difficult to measure precisely. Then, assuming a constant spin temperature, we can derive the column density $N(\text{H})$ as

$$N(\text{H}) = 1.823 \times 10^{18} \int -\ln \left(1 - \frac{T_b(v)}{T_s - T_{\text{bg}}} \right) T_s dv \text{ cm}^{-2}. \quad (2.4)$$

The typical column density of H I gas in the Orion region is $\sim 3 \times 10^{21} \text{ cm}^{-2}$.

2.2.2 Molecular clouds

In a cold and dense ISM region, the major form of hydrogen is the H₂ molecule, and hence, such cold and dense clouds are called molecular clouds (MCs). Since the dense surface of a MC shields interstellar ultraviolet (UV) photons which dissociate molecules, the formation of molecules progresses inside the cloud. At first, MCs were optically observed as dark clouds where few stars are present. Later, these regions were understood as the densest parts of the ISM. However, a direct measurement of H₂, the main component of MCs, is difficult because it does not have any line emission that can be easily observed. The first direct measurement of H₂ gas was achieved by a rocket observation using Lyman alpha absorption in far-ultraviolet wave bands (Carruthers, 1970).

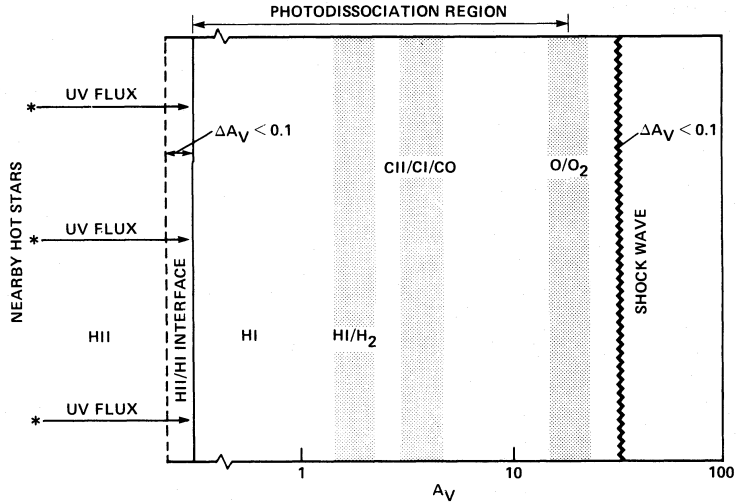


Figure 2.7: Schematic view of a photodissociation region (Tielens & Hollenbach, 1985).

Figure 2.7 shows a schematic structure of a photodissociation region which lies between ionized gas and molecular gas (Tielens & Hollenbach, 1985). The transformation between H I to H₂ does not behave like a step function. The form of the gas gradually changes as the gas density increases.

The two of most abundant chemical components in MCs are H₂ and He, and the third is carbon monoxide (CO). CO cannot exist in the surface of MCs because it is dissociated by UV photons. However, in denser regions, a large part of carbon is thought to exist in the form of CO molecules. So far, CO has been widely used to study MCs as one of the best tracers alternative to “invisible” H₂ and He. In fact, the CO molecule is a heteronuclear diatomic molecule, whose rotational energy levels are given by

$$E_J = \frac{\hbar^2}{2\mu R^2} J(J+1) \quad (J = 0, 1, 2, \dots), \quad (2.5)$$

where \hbar is the Dirac’s constant, μ is the reduced mass of the two nuclei, R is the internuclear distance, and J is the rotational quantum number. The energy separation between the $J = 0$ and $J = 1$ states (hereafter denoted as $J = 1 - 0$) is $E_{J=1-0} = \hbar^2/\mu R^2$. In the case of a CO molecule, this energy corresponds to 115 GHz or 2.6 mm radio line. The line was first detected by Wilson et al. (1970), and since then it has been widely used to study MCs. So far, a large area of the sky has been observed with the 115 GHz line (Dame et al., 1987, 2001). Figure 2.6c is a CO map of the Galactic plane obtained by the most recent survey (Dame et al., 2001).

The distributions, shapes, and masses of MCs have been estimated using CO data instead of direct detections of H₂ or He (see e.g. Wilson et al., 2005). Major MCs close to the Sun, revealed in this way, are shown in Figure 2.8 (Dame et al., 1987). Usually in this kind of studies, the H₂ column density $N(\text{H}_2)$ is estimated from velocity-integrated CO intensity W_{CO} , by empirically assuming that their ratio,

$$X_{\text{CO}} \equiv N(\text{H}_2)/W_{\text{CO}} \text{ cm}^{-2}(\text{K km s}^{-1})^{-1}, \quad (2.6)$$

has a roughly constant value, e.g. $(2.6 \pm 1.2) \times 10^{20}$ by Bloemen et al. (1984) or $(1.8 \pm 0.3) \times 10^{20}$ by Dame et al. (2001). Utilizing X_{CO} is useful to understand the global structure of MCs and the Galactic scale distribution of MCs. However, the value of X_{CO} is rather uncertain, and its constancy is controversial. Small scale structure (~ 10 pc) of MCs is not traced by a constant X_{CO} , due to gas temperature, optical thickness, and PDRs. In addition, we expect X_{CO} to depend, at least to some extent, on the ISM metallicity. Then, even if the H₂ to CO ratio is constant in a small region, the ratio

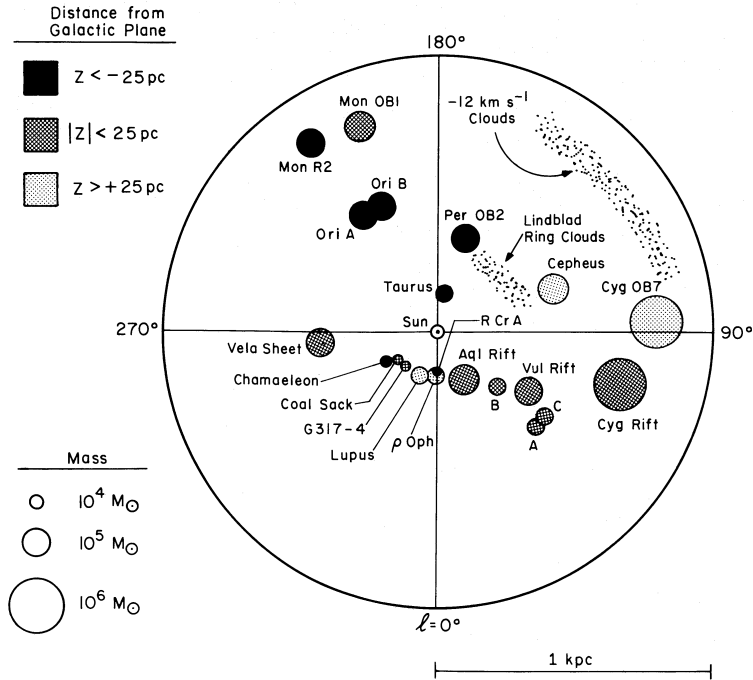


Figure 2.8: The distribution of molecular clouds in the Solar vicinity (Dame et al., 1987).

can change from position to position in the Galaxy, or galaxy by galaxy because the metallicity differs (Arimoto et al., 1996; Wilson, 1995; Strong et al., 2004b). In addition to this, gamma-ray and infrared observations of ISM have revealed the existence of “dark gas” which cannot be detected by H I or CO observations (Boulanger et al., 1998; Greiner et al., 2005). This will be discussed in the next subsection.

2.2.3 Interstellar dust

Both atomic and molecular gases contain small solid grains, the sizes of which are smaller than $\sim 10^{-3}$ mm. Composed of non-volatile chemical compounds containing C, Mg, Si, S, and Fe, these grains are called interstellar dust. It plays two important roles in the study of ISM even though its mass fraction is much smaller than those of H I and H₂ gases. First, H₂ molecules cannot form without dust grains. When two H atoms collide, they do not combine together, because surplus binding energies are not released in the space environment without catalyst which absorbs them. Therefore, transformation from atomic gas to molecular gas occurs on the surface of dust grains. Second, interstellar dusts provide an independent way to estimate the mass of MCs. They are thought to be distributed in both H I and H₂ gases with similar fractions. As a result, they trace the structure of these gases. Even if the assumption of a constant X_{CO} is incorrect, complementary dust observations of MCs will thus reveal the shape of MCs. In fact, Greiner et al. (2005) studied if there exists hidden ISM which cannot be observed by radio telescopes but detected by gamma-ray observations. They have shown that the spatial excess of diffuse gamma rays observed by EGRET, which is not predicted by H I or CO maps, can be partially explained by the dust map. Boulanger et al. (1998) independently studied the Chamaeleon MCs by comparing CO and dust data. They also found that the CO intensity is not always proportional to the dust column density.

Interstellar dusts can be observed by several methods unlike H I or H₂. They absorb or emit infrared (IR) radiation according to their temperature. Schlegel et al. (1998) constructed a dust map using the data of the IRAS mission, calibrated with the data of the DIRBE experiment on board the COBE satellite. The

dusts also work as obscuration of visible star light as shown in Figure 2.6a. The number of observable stars in a region is expected to decrease in correlation with the column density of the dust in the region. With this star-count technique, Dobashi et al. (2005) constructed a dust map using the archival database of Digitized Sky Survey. The map is referred to as visual extinction (A_V) map. A part of the latter map is shown in Figure 2.6d. The extinction of star light is also measured by a reddening technique (e.g. Alves et al., 2001). This method utilizes the difference of transmissivity depending on wavelengths of starlight.

These techniques are established methods. However, they have some intrinsic problems. First, unlike the 21 cm and the 115 GHz lines, the above techniques cannot separate H I and H₂ components. Second, they cannot be always used in a region we are interested. For example, star-counting technique cannot be adopted in bright MC cores because bright H II gas and stars saturate star images. IR observations strongly depend on dust temperature, and thus their calibration is difficult. The reddening and polarization technique requires bright stars behind MCs.

2.3 Gamma-Ray Production in Interstellar Environments

The Galaxy is filled with ISM and CRs as described above. Electromagnetic and hadronic interactions occur when they collide with each other, leading to the production of various secondary particles including gamma rays in particular. We explain three important processes in the production of diffuse gamma-ray emission in interstellar environments; gamma rays from hadronic interactions between CRs and ISM, bremsstrahlung radiation from collisions between CR electrons and ISM nuclei, and inverse Compton scattering of CR electrons off interstellar radiation fields. They dominate diffuse gamma-ray emission in the Galaxy in the photon energy range between ~ 100 MeV and ~ 100 GeV (Bloemen, 1985). Other processes such as synchrotron radiation and gamma decay are negligible in this energy band.

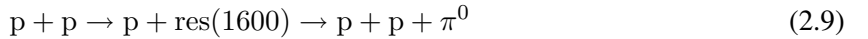
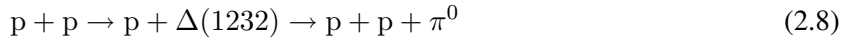
2.3.1 π^0 gamma rays

Hadronic interactions between CRs and ISM produce secondary particles such as neutral pions (π^0) and neutral kaons (K^0) which decay into gamma rays. These gamma rays are referred to as “ π^0 gamma rays”, and play an important role in high-energy gamma-ray astrophysics; hereafter we refer to all gamma rays produced in hadronic interactions as “ π^0 gamma rays”. In a collision between a CR proton and a hydrogen nucleus in ISM (p-p collision), neutral and charged pions are generated as

$$p + p \rightarrow p + p + \zeta_{\pm} \pi^{\pm} + \zeta_0 \pi^0, \quad (2.7)$$

where ζ_{\pm} and ζ_0 are the average numbers of π^{\pm} and π^0 particles (Stecker, 1970). As shown in Table 2.2, the produced pions then decay, via electromagnetic or weak interactions, finally to stable particles; gamma rays, electrons, positrons and neutrinos. The kinetic energy of an incident proton at the threshold of pion production is $E_{\text{th}} = 2m_{\pi}(1 + m_{\pi}/4m_p) \simeq 280$ MeV/ c^2 (see appendix A.1). Thus, CR protons with energies below this threshold are not related to the π^0 gamma-ray production.

In addition to this multiple pion production process, the contribution from baryon resonances, either $\Delta(1232)$ or $\text{res}(1600)$ ⁴, cannot be neglected around the threshold energy (Kamae et al., 2006):



These resonances are called isobar model, which is based on a theory that the π^0 production is induced by the excitation of $\Delta_{3/2}$ isobar.

⁴ $\text{res}(1600)$ represents resonances around 1600 MeV/ c^2 .

Table 2.2: Decay modes of pions and muons (Amsler et al., 2008).

Particle	Mass (MeV/c ²)	Mean Life Time (s)	Mode	Fraction (%)
π^0	134.98	$(8.4 \pm 0.6) \times 10^{-17}$	$\gamma + \gamma$	98.8
			$e^+ + e^- + \gamma$	1.2
π^+	139.57	2.6×10^{-8}	$\mu^+ + \nu_\mu$	99.988
			$\mu^+ + \nu_\mu + \gamma$	2×10^{-4}
			$e^+ + \nu_e$	1.2×10^{-4}
μ^+	105.66	2.197×10^{-6}	$e^+ + \nu_e + \bar{\nu}_\mu$	$\simeq 100$

Note: Modes of π^- and μ^- are charge conjugates of those of π^+ and μ^+ .

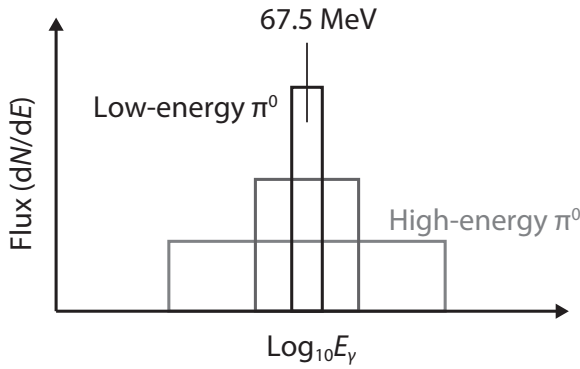


Figure 2.9: Schematic shapes of the π^0 -decay gamma-ray spectrum.

The p-p collision is known to contribute to the gamma-ray production predominantly via two-body decay of π^0 particles , as



In the rest frame of π^0 , these two photons are emitted in the opposite directions, and their energies become

$$E_\gamma = \frac{m_{\pi^0}}{2} \simeq 67.5 \text{ MeV}, \quad (2.11)$$

where m_{π^0} is the rest mass of π^0 . However, the π^0 particles produced via p-p collision are boosted toward the initial momentum of the projectile CR proton. As a result, the two photons of equation (2.10) can have largely different energies as measured in the laboratory frame. As shown in Figure 2.9, the resultant gamma-ray spectrum becomes symmetric in the logarithmic scale with respect to the line $E_\gamma = m_{\pi^0}/2$ in the laboratory system. Higher energy pions produce a broader spectrum than that of lower energy pions. Therefore, the total spectrum of gamma rays integrated in all π^0 energies becomes symmetric, and has a peak called “ π^0 bump” at $E_\gamma = 67.5$ MeV. See appendix A.2 for details of the calculation.

In addition to π^0 's directly produced by p-p interactions, other secondary mesons, such as K_L and K_S decay to π^0 's. Moreover other decay modes are known to be contributing (Huang et al., 2007); for example, direct gamma-ray emission in p-p collisions, three-body decay of π^0 , and K meson decay,

expressed respectively as



It is known that approximately a constant fraction of kinetic energies of the projectile protons are transferred to secondary π^0 , over broad region from GeV to TeV (Gaisser, 1990). As a result, the power law indices of the incident CRs and the produced diffuse gamma rays become similar. For example, the photon index of π^0 gamma ray emission in a region where the shock front of a SNR collides with surrounding molecular clouds will be ~ 2.1 . That of the typical Galactic region is expected to be ~ 2.7 , because the spectral index of typical Galactic CR is thought to be ~ 2.7 . The π^0 bump and the photon index are key features of the CR interactions with ISM.

Figure 2.10 shows the cross section of p-p collisions as a function of the momentum of the projectile proton. The inelastic cross-section rapidly increases at around the threshold energy and becomes almost flat (~ 25 mb) from $1\text{ GeV}/c$ to $1\text{ TeV}/c$. The typical column density of the Orion molecular clouds is an order of 10^{22}cm^{-2} . Therefore, the probability for a CR proton traveling through the MC to interact is an order of $10^{22}\text{cm}^{-2} \times 25\text{ mb} \sim 10^{-4}$. It means that molecular clouds are usually thin against CRs.

The π^0 gamma-ray emission carries important information on the distribution of the Galactic cosmic rays and the structure of the ISM, because the emissivity of π^0 gamma rays is proportional to the CR flux and ISM density. Thus, the gamma-ray emissivity of p-p interactions has been extensively calculated by many authors over a few decades, utilizing experimental data of accelerators and scattering theories (e.g. Stecker, 1970; Dermer, 1986; Mori, 1997; Kamae et al., 2006; Kelner et al., 2006; Huang et al., 2007). However, direct comparison of these models is not easy, because each model assumes different CR fluxes and ISM abundances. We have developed a Python package, PyCRFlux⁵, so that we can compare the models directly. Figure 2.11 shows a comparison among three models of gamma-ray emissivity (Dermer, 1986; Mori, 1997; Kamae et al., 2006), where we used the same CR proton flux predicted by GALPROP as shown in Figure 2.2, and the same gas condition that is filled with only H atoms ($n_H = 1\text{cm}^{-3}$). The π^0 model calculated by Kamae et al. (2006) is the most up-to-date one among many works. It includes contributions from diffractive processes and violation of the Feynman scaling. As shown in the bottom of Figure 2.11, these contributions appear at 10% levels above 1 GeV. Bumps in the model by Dermer (1986) is due to a combination of different models for different energy bands. The model by Kamae et al. (2006) predicts asymmetric gamma-ray spectrum below 100 MeV. This is due to a limitation in their parametrization. However, in the present thesis, the uncertainty in this energy region does not matter.

The calculation of the π^0 gamma-ray emissivity from ISM also depends on models of gamma-ray inclusive cross-sections⁶ between heavier nuclei collisions. Our experimental knowledge on heavier nuclei interactions is limited, although the contribution from helium and metals cannot be neglected in calculating the total π^0 gamma-ray emissivity. If we simply assume that the incoming CRs and the target ISM have proton to alpha (or H to He) ratios of 1 : 0.05 (see Figure 2.2) and 1 : 0.1, respectively, and that a helium nucleus consists of independent 4 nucleons, then the total π^0 gamma-ray emissivity will become 1.68 relative to the case considering p-p interactions only⁷. Contributions from p-H, p-He, α -H, and α -He interactions are listed in Table 2.3a. However in reality, the calculation is more complicated. There exist CRs heavier than protons and alpha particles in the Galaxy, and the ISM as well. A heavier nucleus is not actually an assembly of nucleons. The cross section between heavier nuclei collision is smaller than that of p-p collision multiplied by its nucleon number A , due to “shadowing effect”. Moreover,

⁵<http://www-glast.stanford.edu/cgi-bin/viewcvs/users/oxon/PyCRFlux/>

⁶Cross section multiplied by the number of gamma rays.

⁷ $1.68 = 1 \times 1 + 1 \times 0.1 \times 4 + 0.05 \times 1 \times 4 + 0.05 \times 0.1 \times 4 \times 4$

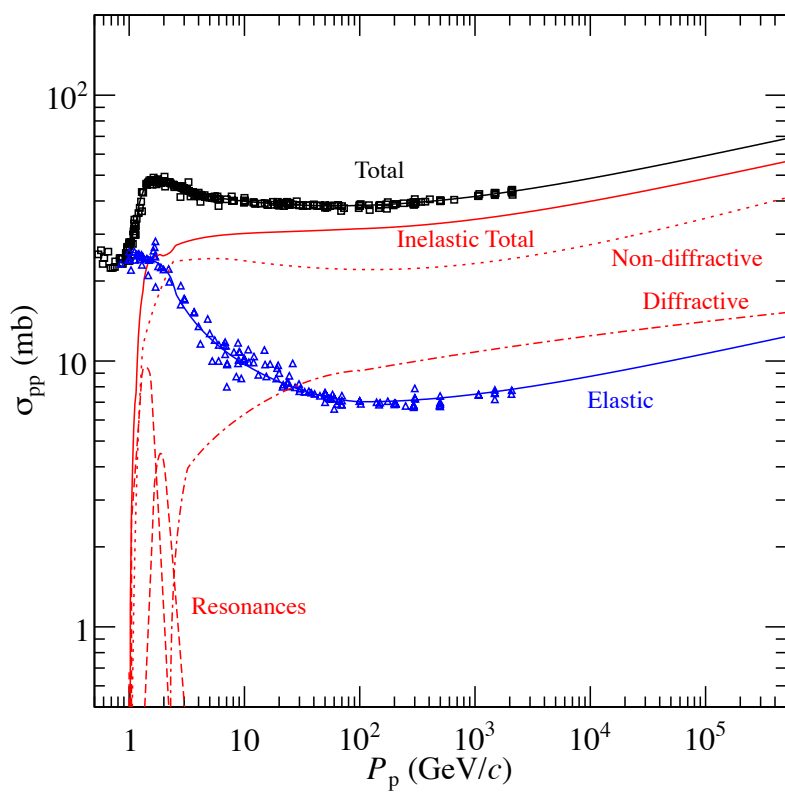


Figure 2.10: The cross section of p-p collision (Kamae et al., 2006, with modification). Red and blue solid lines show the total cross sections of inelastic and elastic scattering, respectively. The black solid line is the sum of them. The inelastic cross section is broken down into non-diffractive (red dotted), diffractive (red dot-dashed), and resonance (red dashed) processes.

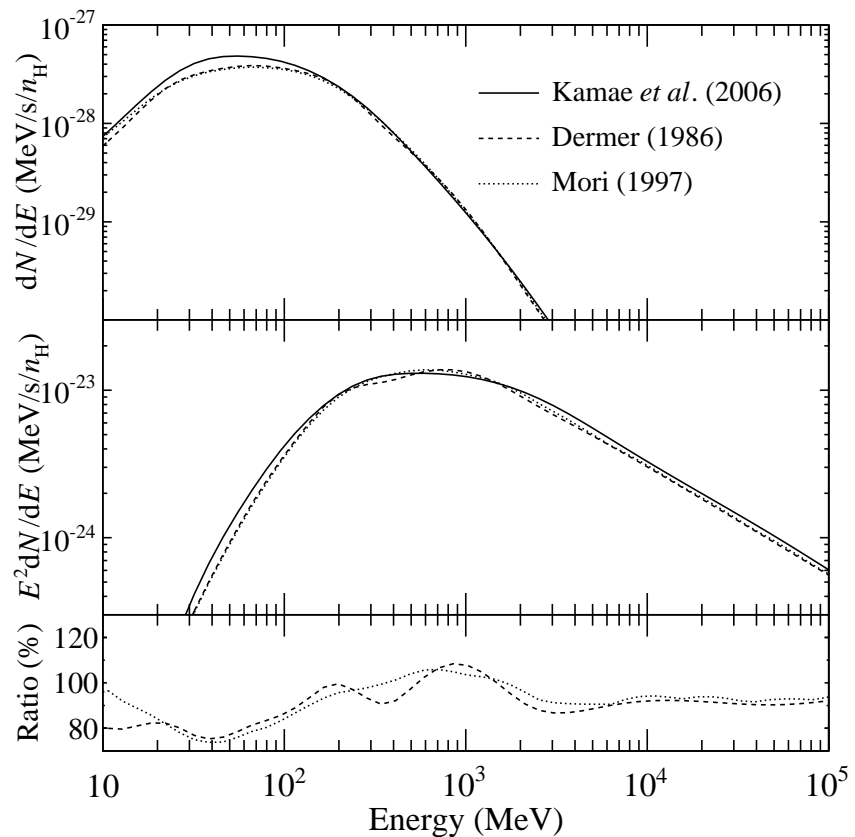


Figure 2.11: Comparison of three models of π^0 gamma-ray emissivity from ISM. Solid, dashed and dotted lines are calculations based on Kamae et al. (2006), Dermer (1986), and Mori (1997), respectively. (top) Differential gamma-ray emissivities. (middle) Same as the top panel, but E^2 is multiplied. (bottom) The latter two models normalized to that of Kamae et al. (2006).

Table 2.3: π^0 gamma-ray contributions from CR α and ISM He. The proton to α ratio in CRs, and the H to He ratio in ISM are assumed to be 1 : 0.05 and 1 : 0.1, respectively. The 2nd, 4th, and 6th columns show inclusive cross-sections of π^0 relative to that of p-p interaction. The 3rd, 5th, and 7th show relative gamma-ray emissivities. (a) Assuming a helium nucleus consists of independent 4 protons. (b) The method adopted by Dermer (1986). Cross-sections were compiled by Ashmore et al. (1960). (c) The method adopted by Gaisser & Schaefer (1992).

CR-ISM	(a) 4 protons		(b) Dermer (1986)		(c) Gaisser & Schaefer (1992)	
	Rel. σ_π	Rel. gamma	Rel. σ_π	Rel. gamma	Rel. σ_π	Rel. gamma
p-H	1	1.00	1	1.00	1	1.00
p-He	4	0.40	2.83	0.28	3.57	0.36
α -H	4	0.20	2.83	0.14	3.57	0.18
α -He	16	0.08	5.59	0.03	12.6	0.06
metal-H	–	–	–	–	–	0.05
metal-He	–	–	–	–	–	0.02
total		1.68		1.45		1.67

we have to take into account multiple scatterings inside the nuclei. Many authors have modeled the cross sections of heavier nuclei interactions using the data obtained in accelerator experiments (Orth & Buffington, 1976; Białas et al., 1976; Gaisser & Schaefer, 1992).

To calculate gamma-ray emissivity from heavier nuclei interactions, Dermer (1986) used the following equation, which is an empirical “inelastic” cross-section fitted to experimental data (Ashmore et al., 1960; Orth & Buffington, 1976),

$$\sigma \propto \left(A_{\text{P}}^{3/8} + A_{\text{T}}^{3/8} - 1 \right)^2, \quad (2.15)$$

where σ is the inclusive cross-section of π^0 , while A_{P} and A_{T} are the nucleon numbers of the projectile and target nuclei in a collision, respectively. This model has been used in the EGRET era. We note that the equation neglects multiplicity of π^0 production in a nucleus, and that it was fitted with only proton-nucleus interactions. The contribution from helium nuclei with this model is listed in Table 2.3b.

In their calculation of secondary antiproton flux in the Galaxy, Gaisser & Schaefer (1992) estimated the contribution from p-He, α -H, α -He and other heavier CRs. Mori (1997) adopted their method to calculate the π^0 gamma-ray emissivity. In this approach, we assume that the multiplicity of produced secondary particles in one collision between nucleus A and nucleus B can be written as (Białas et al., 1976),

$$n_{AB} = \frac{1}{2} \left(A \frac{\sigma_{pB,\text{inel}}}{\sigma_{AB,\text{inel}}} + B \frac{\sigma_{pA,\text{inel}}}{\sigma_{AB,\text{inel}}} \right) n_{pp} \equiv \frac{1}{2} w_{AB} n_{pp}, \quad (2.16)$$

where A and B are nucleon numbers of A and B, $\sigma_{AB,\text{inel}}$, $\sigma_{pA,\text{inel}}$ and $\sigma_{pB,\text{inel}}$ are total inelastic cross sections of A-B, p-A and p-B collisions, respectively, and n_{pp} is the multiplicity of secondary particle production in a p-p collision. In our case, n_{pp} corresponds to the multiplicity of secondary gamma rays. We also assume that the cross section of an A-B collision for gamma-ray production mode can be scaled using the ratio between $\sigma_{AB,\text{inel}}$ and $\sigma_{pp,\text{inel}}$. Consequently, the inclusive cross section of gamma-ray production in an A-B collision is given by

$$\begin{aligned} \sigma_{AB \rightarrow \gamma} &\simeq \frac{1}{2} w_{AB} \frac{\sigma_{AB,\text{inel}}}{\sigma_{pp,\text{inel}}} \sigma_{pp \rightarrow \gamma} \\ &= \frac{1}{2} (A \sigma_{pB,\text{inel}} + B \sigma_{pA,\text{inel}}) \frac{\sigma_{pp \rightarrow \gamma}}{\sigma_{pp,\text{inel}}} \\ &\equiv m_{AB} \sigma_{pp \rightarrow \gamma}, \end{aligned} \quad (2.17)$$

where $\sigma_{pp \rightarrow \gamma}$ is the inclusive cross section of p-p collisions. Various values of m_{AB} for ISM H and He are tabulated in Table 1 of Gaisser & Schaefer (1992). The contributions from He nuclei and CR metals calculated with this method are listed in Table 2.3c. It is worth mentioning that there exists +15% difference from the method by Dermer (1986).

In addition to the contributions from He nuclei and CR metals, Mori (2009) calculated the contribution from ISM metals using a Monte Carlo simulation program DPMJET-III. He estimated the contribution to be of the order of 2%.

2.3.2 Electron bremsstrahlung

In interstellar environments, bremsstrahlung radiation between high-energy CR electrons and protons which are effectively at rest overwhelms the radiation of π^0 gamma rays, in the energy range below ~ 100 MeV. The energy loss rate of CR electrons in neutral gases (H I, H₂) can be approximated as (Strong & Moskalenko, 1998),

$$\left(\frac{dE}{dt}\right)_B = \begin{cases} -4\alpha r_e^2 c E \left[\ln(2\gamma) - \frac{1}{3}\right] \sum_{s=\text{H,He}} n_s Z_s (Z_s + 1), & \gamma \lesssim 100 \\ -c E \sum_{s=\text{H,He}} \frac{n_s M_s}{T_s}, & \gamma \gtrsim 800, \end{cases} \quad (2.18)$$

where α is the fine structure constant, r_e and m_e are the classical electron radius and the electron mass, respectively, c is the velocity of light, E and γ are the energy and the Lorentz factor of an incident electron, and n_s , Z_s , M_s and T_s are the gas density, the atomic number, the atomic mass and the radiation length, respectively. Here we assumed that the gas consists of only H and He.

In the case of relativistic electron interactions, gamma-ray emissivity per photon frequency ω is roughly constant as (Rybicki & Lightman, 1979)

$$\frac{dE}{dtd\omega} \sim \text{constant}. \quad (2.19)$$

Therefore, the spectral index of bremsstrahlung radiation produced by high-energy CR electrons and ISM becomes similar to that of the incoming CR electrons, namely ~ 3 (see Figure 2.3).

2.3.3 Inverse Compton scattering

High-energy CR electrons also interact with electromagnetic fields in the Galaxy. This process is referred to as synchrotron radiation when the field is a non-oscillating magnetic field, and is as inverse Compton (IC) scattering when the electromagnetic field is provided by photons such as those in the cosmic microwave background. In the MeV–GeV region, the IC process is more important. The energy loss rate of IC is given by

$$\left(\frac{dE}{dt}\right)_{\text{IC}} \simeq -\frac{4}{3} c \sigma_T \beta^2 \gamma^2 U, \quad (2.20)$$

where U is the photon energy density, and σ_T is the cross section of Thomson scattering (Rybicki & Lightman, 1979). In the Klein-Nishina regime, the efficiency decreases. The contribution of IC emission is less than an order of magnitude than that of π^0 gamma-ray emission from dense MCs.

2.4 The Orion Molecular Clouds

2.4.1 The Orion region

A wide sky region around the Orion constellation is referred to “Orion region”, which is extended over the Galactic coordinates of $(l, b) = (200^\circ \sim 220^\circ, -10^\circ \sim -30^\circ)$. The region has been extensively studied

by various wavelengths because it hosts typical MCs that are known as active star forming regions. Two of the most massive and important giant molecular clouds (GMCs) in the region are Orion A and B clouds, which are archetypes of local GMCs where interstellar gas condenses and stars are being formed. As shown in Figure 2.8, Orion A and B are located within 500 pc from the Sun and away from the Galactic plane. Thanks to their large size and near locations, they have been well resolved by radio telescopes.

Figures 2.12a and 2.12b show an optical mosaic image of the Orion region (Mellinger, 2008), and its schematic view, respectively. There are three GMCs, Orion A, Orion B, and Monoceros R2, located in the center of the region. Orion A has a bright diffuse nebula (or H II region) in its core. This nebula is known as the Orion Nebula (also known as M42) which can be seen with naked eyes (see around the coordinates of $(l, b) = (209^\circ, -25^\circ)$ in Figure 2.12a). As the gas collapses under their own gravitational force, stars are formed inside, and then they emit ultraviolet photons. These photons ionize the surrounding gas. As a result, the Orion Nebula becomes bright with visible photons which are supplied by the ionized plasma. There is a red arc with a radius of $\sim 5^\circ$ encircling the Orion Nebula. This is called “Barnard’s Loop” and thought to be a supernova remnant, the progenitor of which has exploded 2 million years ago in the Orion Nebula.

The distances to the two clouds, Orion A and Orion B, have been estimated to be $400 \sim 500$ pc from the Sun (see e.g. Wilson et al., 2005). As listed in Table 2.4, recent parallax observations of the Orion Nebula made by the most advanced radio telescopes have measured the distance precisely. The weighted mean of the results becomes 416.4 ± 4.3 pc. The apparent sizes of Orion A and B are roughly $8^\circ \times 3^\circ$ and $5^\circ \times 2^\circ$, respectively. At a distance of 400 pc, their actual sizes can be estimated to be $\sim 50 \times 20$ pc 2 and $\sim 30 \times 10$ pc 2 , respectively. The Galactic coordinates of the Orion A and B clouds are roughly $(l, b) = (211^\circ, -19^\circ)$ and $(206^\circ, -15^\circ)$. If we assume that the Galactic cylindrical coordinates of the Sun is $(R, Z) = (8.5$ kpc, 0 kpc), those of the clouds are $(R, Z) = (8.83$ kpc, -0.13 kpc) and $(8.85$ kpc, -0.10 kpc), respectively.

The apparent brightness of nebulae and gas is not proportional to their mass, because molecular gas itself does not emit visible photons. Moreover, MCs obscure the light from background stars due to the dust existing inside them. By looking at Figure 2.12a carefully, we can see that the shaded regions in Figure 2.12b are slightly darker than the outer region in Figure 2.12a. As explained in Section 2.2.2, “invisible” or “dark” clouds can be traced by radio observations instead. Figure 2.12c shows a CO intensity map of the region (Dame et al., 2001), where it shows bright cores corresponding bright nebulae (see Figure 2.12b) in addition to the fine structure of the Orion MCs. Figure 2.12e is a dust map constructed by a star count technique⁸ (Dobashi et al., 2005). The same region observed by the 21 cm line is shown in Figure 2.12d which reveals the distribution of H I gas surrounding the Orion MCs. Since both H₂ and H I gases include dust grains, the A_V map is thought to trace nearby MCs and a part of H I gas. In fact, the similar structure of the Orion clouds are found in both Figures 2.12c and 2.12e. In addition, the similar structure of the Galactic plane is found in Figures 2.12d and 2.12e. We note that the A_V map shows the left part of the Orion A cloud is bright as well as the dense region of the Orion B clouds, but dim in the CO map. This fact implies that there may exist gas which is not traced by the CO or H I observations. Figure 2.12f also shows a dust map constructed from IR observations (Schlegel et al., 1998) in which the unit is converted to reddening magnitude. Since the IR observation is strongly affected by the dust temperature (Schlegel et al., 1998), it cannot be used to directly study the structure of MCs.

2.4.2 Molecular masses of the Orion clouds

The mass of a celestial object is one of fundamental quantities in almost all cases. Those of the Orion MCs have been estimated assuming a constant conversion factor X_{CO} . While many authors have pointed

⁸They count the number of stars and calculate the magnitude of visible light extinction. Since the Orion A core is too bright and saturated in the optical image plate they used, the star count technique cannot be adopted in such a region. Saturated regions are shown with black pixels in Figure 2.12e.

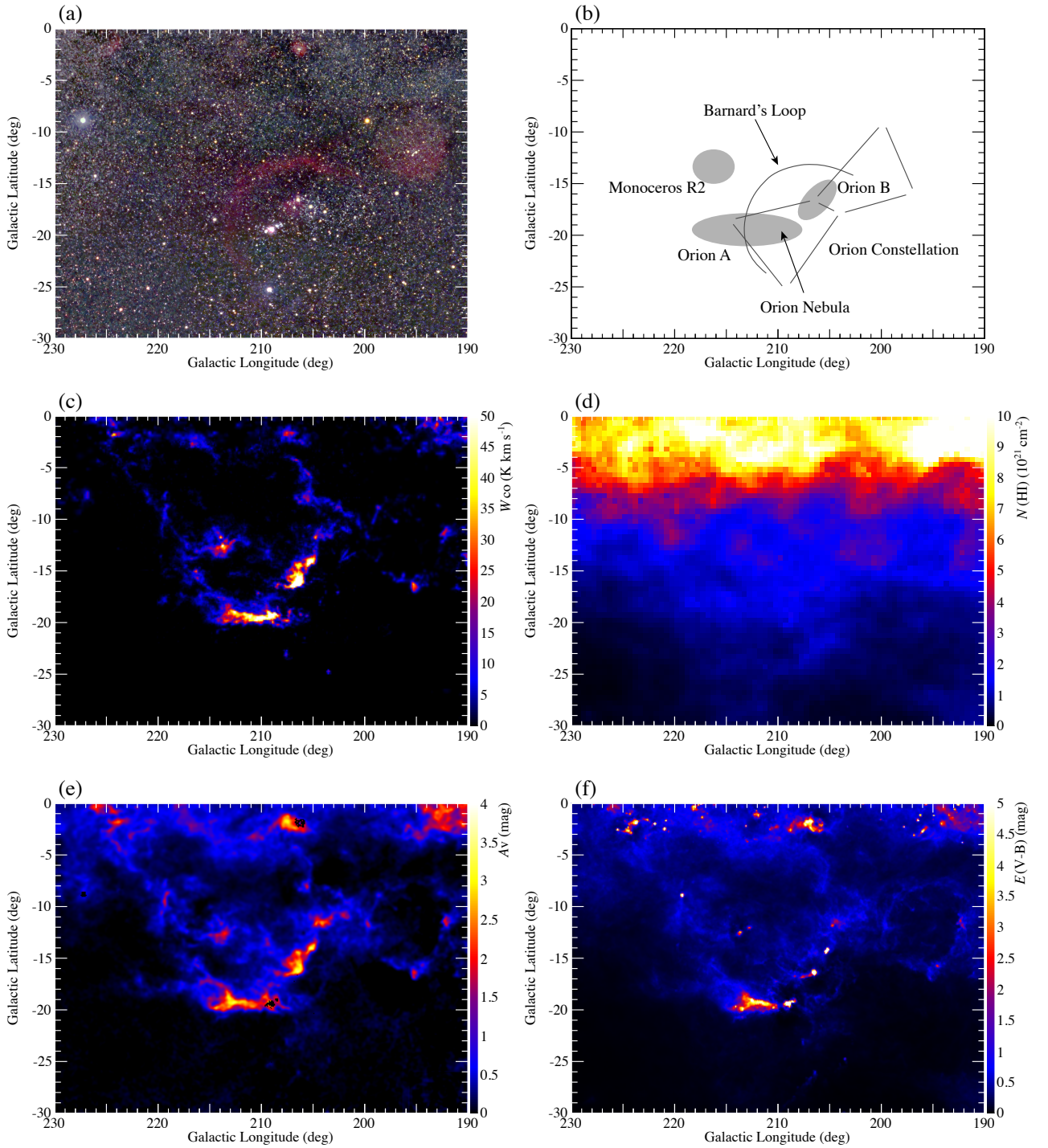


Figure 2.12: Multiwavelength view of the Orion region. (a) An optical image (Mellinger, 2008). (b) Schematic view of the Orion region. (c) A CO intensity map (Dame et al., 2001). (d) An H I column density map (Kalberla et al., 2005). (e) A visual extinction map (Dobashi et al., 2005). (f) A reddening map (Schlegel et al., 1998).

Table 2.4: The distance to the Orion nebula measured by four different parallax observations.

Telescope	Target	Distance	Reference
VLBA	GMR A,F,G,12	414 ± 7	Menten et al. (2007)
VLBA	GMR A	389^{+24}_{-21}	Sandstrom et al. (2007)
VERA (H ₂ O maser)	Orion KL	437 ± 19	Hirota et al. (2007)
VERA (SiO maser)	Orion KL	418 ± 6	Kim et al. (2008)
Weighted mean		416.4 ± 4.3	

Table 2.5: The masses of the Orion molecular clouds (Wilson et al., 2005). The clouds are divided in six smaller regions, of which the distances were cited from the *Hipparcos* catalog.

Region	Distance (pc)	Molecular mass ($10^3 M_{\odot}$)
Orion A:		105.1
1	521^{+140}_{-91}	12.3
2	465^{+75}_{-57}	69.5
3	412^{+114}_{-74}	23.3
Orion B:		82.3
1 near	422^{+61}_{-48}	11.9
1 far	514^{+106}_{-75}	53.4
2	387^{+112}_{-71}	18.1

out that CO is saturated in dense cores of GMCs, it is still widely used in estimating the mass of a cloud because most of the mass is contained in the lower-density envelopes (Cambrésy, 1999). Table 2.5 shows an estimation of their masses calculated by Wilson et al. (2005) from a CO map and a constant factor $X_{\text{CO}} = 1.8 \times 10^{20} \text{ cm}^{-2}(\text{K km s}^{-1})^{-1}$.

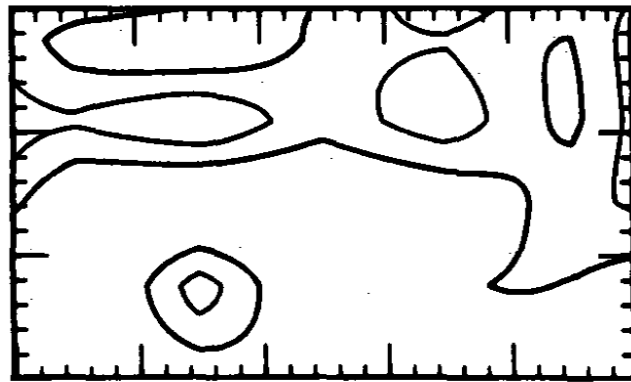
2.4.3 Previous gamma-ray observations and their limitations

As shown in Figure 2.6, the brightest gamma-ray source in the sky is the Galactic plane. Since MCs are Galactic “sources”, most of them are located at low Galactic latitudes. Hence small and distant MCs may not be easily separated by gamma-ray telescopes from the emission of the Galactic plane. Among them, the Orion clouds are located at the opposite direction to the Galactic center, and away from the Galactic plane, and near from the Earth. Therefore they are the best MCs to be studied by gamma-ray telescopes.

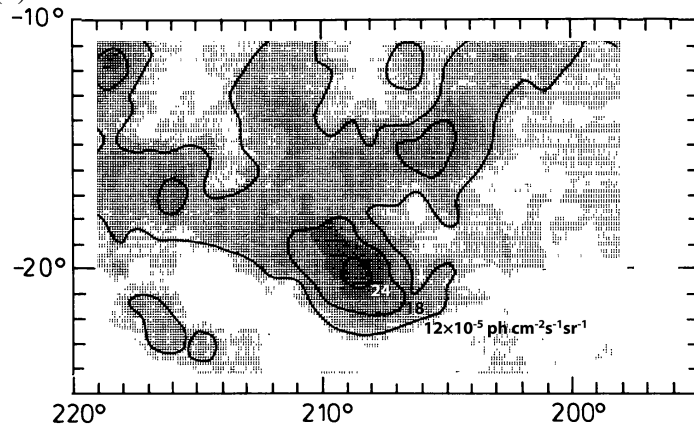
The Orion region has been observed by gamma-ray telescopes; SAS-2, *COS-B*, and *Compton Gamma-Ray Observatory/EGRET* in 1970s, 1980s and 1990s, respectively. The first observations by SAS-2 did not yield a significant detection from the Orion clouds, even though a small excess was found near Orion A as shown in Figure 2.13a (Thompson et al., 1977). As shown in Figure 2.13b, the second observations by *COS-B* detected a significant excess near the core of Orion A (Caraveo et al., 1980; Bloemen et al., 1984). However, the energy spectra of the region was not derived and the spatial structure of the clouds were not sharply resolved, due to the limited photon statistics and spatial resolution. The third observations by the EGRET was greatly improved, thanks to its high sensitivity and long observation time. The EGRET has revealed rough shapes of Orion A, Orion B and Monoceros R2, and derived their gamma-ray energy spectrum of the region as shown in Figure 2.15 (Digel et al., 1995, 1999).

In spite of the great leap provided by the EGRET results, there still remain two problems. One

(a) SAS-2



(b) COS-B



(c) EGRET

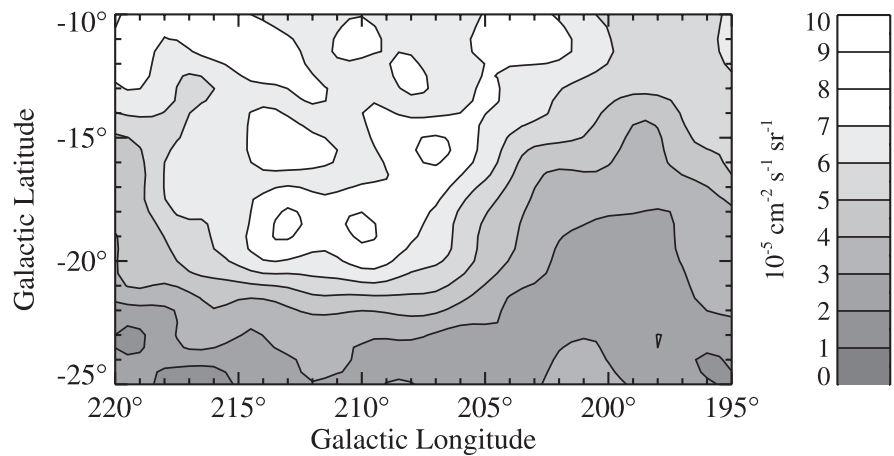


Figure 2.13: Gamma-ray intensity maps of the Orion region obtained by SAS-2, COS-B, and the EGRET. (a) SAS-2 observations above 35 MeV (Thompson et al., 1977, with modification). (b) COS-B observations between 100 MeV and 5 GeV (Bloemen et al., 1984, with modification). (c) The EGRET results between 30 MeV and 10 GeV (Digel et al., 1999, with modification).

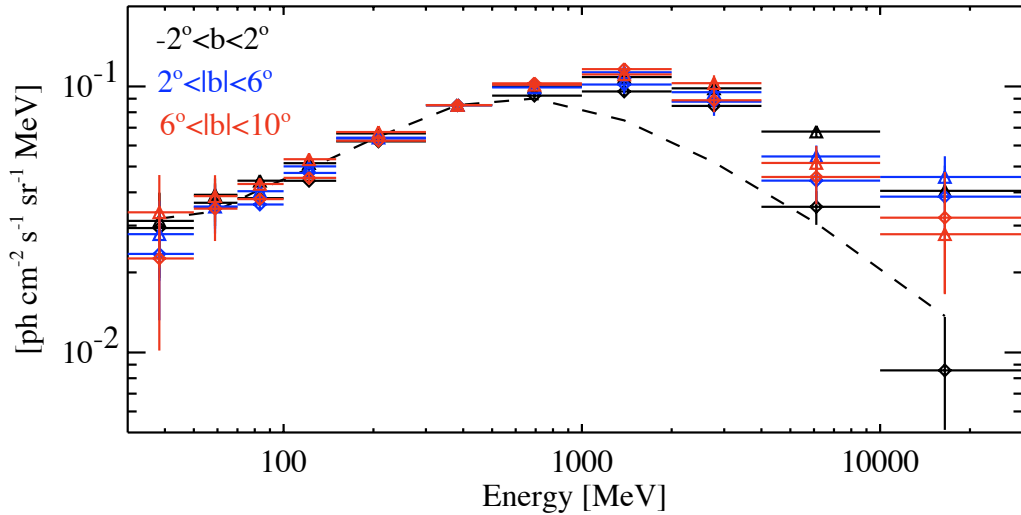


Figure 2.14: The energy spectra of diffuse gamma-ray emission from the Galactic plane observed by EGRET (Hunter et al., 1997, with modification). A dashed line shows a gamma-ray emission model based on π^0 production and the CR energy spectrum at the Earth.

is so-called “GeV excess”. The energy spectra of diffuse gamma-ray emission at various sky regions obtained by the EGRET generally exhibited hard components above 1 GeV, which were not explained by the widely accepted concept that the diffuse emission is induced by the interactions between CRs and ISM (Hunter et al., 1997; Strong et al., 2004a). The observed energy spectra of diffuse gamma-ray emission from the Galactic plane by EGRET are shown in Figure 2.14. If their result is correct, the CR spectra measured at the Earth (indices ~ 2.7) must be considered as a local one which does not represent the typical CR fluxes in the Galaxy. The same can be said for the Orion spectrum, even though the photon statistics above 1 GeV were not good enough; only one bin covers one decade between 1 GeV and 10 GeV in Figure 2.15. As Aharonian (2001) pointed out, this highest-energy data point by Digel et al. (1999) is not consistent with the local CR spectra (red lines in Figure 2.15). He calculated several energy spectra based on different CR spectra, and indicated that a harder CR spectrum reproduced the observed data better.

The second problem is the conversion factor X_{CO} . Digel et al. (1999) assumed that X_{CO} was spatially constant in the region but energy dependent. This assumption is not necessarily true. As mentioned in Subsection 2.4, the A_V map suggest the presence of dense gas in the left part of Orion A. The intensity map by the EGRET also has the similar sign.

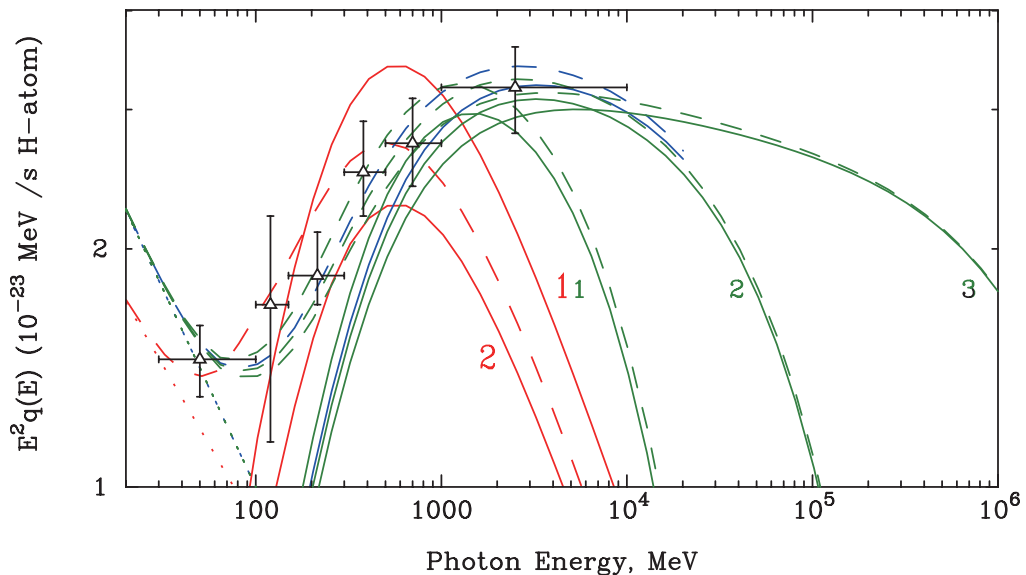


Figure 2.15: Gamma-ray emissivity of the Orion region calculated from the EGRET observations (Digel et al., 1999). Curves indicate numerical emissivity models adjusted to explain the “GeV excess” (Aharonian, 2001). The red line labeled “1” is a normal π^0 emissivity, while red “2” assumes a 1.5 times lower flux. The blue line is a model calculated for a proton flux with power-law index 2.1. Green lines 1, 2 and 3 correspond to emissivities calculated for CR spectra with the same power-law index 2.1, but with exponential cutoff at 3 different energies, $E_0 = 100$ GeV, 1 TeV, and 10 TeV, respectively. Dotted lines are emissivity of bremsstrahlung radiation, while dashed lines are the sum of π^0 and bremsstrahlung. (Aharonian, 2001, with modifications)

Chapter 3

FERMI GAMMA-RAY SPACE TELESCOPE AND THE LARGE AREA TELESCOPE

3.1 The History of Gamma-ray Telescopes

Cosmic high-energy gamma rays (> 100 MeV) were first detected by the *OSO-3* satellite (Clark et al., 1968). It revealed that the Galactic plane is a bright gamma-ray source. Since then, pioneering gamma-ray telescopes onboard satellites have been launched and used to study the high-energy window of the sky. *SAS-2*, *COS-B*, and the EGRET onboard *Compton Gamma-Ray Observatory* have extended our understanding of the high-energy phenomena of the Universe. The first detection of gamma-ray point sources was brought by *SAS-2* (Kniffen et al., 1974; Thompson et al., 1974). After that, the number of established gamma-ray point sources increased by a factor of 10 every generation. Table 3.1 summarizes the historical and current MeV-GeV gamma-ray telescopes.

Among those telescopes, the detection capability of the EGRET was quite excellent. It performed the first all-sky survey above several 10 MeV, and made a high-energy gamma-ray source catalog consisting of 271 point sources (Hartman et al., 1999). As shown in Figure 3.1, the gamma-ray catalog includes 83 active galactic nuclei and 5 pulsars. It is notable that in fact 181 sources of the catalog are unidentified sources which are invisible in other wavelengths. The EGRET has not only revealed the gamma-ray sky, but also given us new mysteries. In order to understand high-energy phenomena more deeply, a new gamma-ray telescope with higher sensitivity and better angular resolution, overwhelming the EGRET,

Table 3.1: Comparison of gamma-ray telescopes. Data are cited from NASA's web page (<http://heasarc.gsfc.nasa.gov/docs/heasarc/missions/past.html>) except for the LAT. The number of LAT sources is as of February 2009 (Abdo et al., 2009c).

Name	Year	Point Sources	Energy Range (eV)	FOV (sr)	Eff. Area (cm ²)	Detector Type
<i>OSO-3</i>	1967–1969	0	> 50 M			Proportional counter
<i>SAS-2</i>	1972–1973	2	20 M – 1 G	540	Spark chamber	
<i>COS-B</i>	1975–1982	25	30 M – 5 G	50	Spark chamber	
EGRET	1991–2000	271	30 M – 10 G	0.5	1500	Spark chamber
LAT	2008–	> 205	20 M – 300 G	2.4	9500	Silicon strip

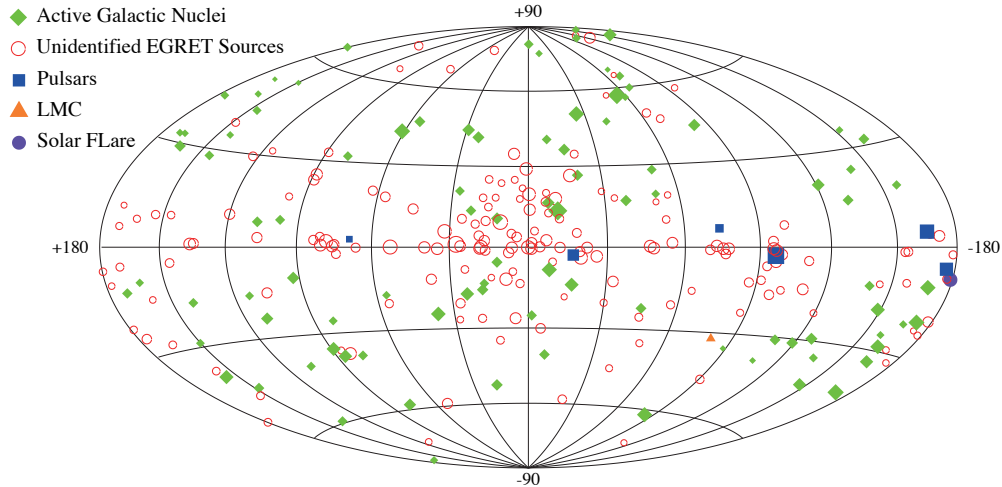


Figure 3.1: The 3rd EGRET catalog (Hartman et al., 1999, with modification)

Table 3.2: Brief specifications of the LAT (Atwood et al., 2009) and the GBM (Meegan et al., 2007)

	LAT	GBM
Energy range	20 MeV - 300 GeV	8 keV – 30 MeV
Field of View	2.4 sr	9 sr
Target	AGN, GRB, ISM, SNR, Micro Quasar, Pulsar, Sun, Dark Matter, Cosmic Ray	GRB, SGR, Solar flares

has been required.

3.2 *Fermi Gamma-ray Space Telescope*

*Fermi Gamma-ray Space Telescope*¹ (*Fermi*) is a satellite mission which observes high-energy cosmic gamma rays. *Fermi* has two gamma-ray detectors; the Large Area Telescope (LAT) and the Gamma-ray Burst Monitor (GBM). The LAT and GBM have different energy bands and field of views because their scientific objectives are different. Brief specifications of the LAT and GBM are listed in Table 3.2.

The LAT is designed to observe a large number of celestial gamma-ray objects in a long-term sky-survey mode, in addition to its ability to study transient objects such as gamma-ray bursts (GRBs). It covers a higher energy band (20 MeV–300 GeV) where electron-positron pair creation becomes the dominant mode of photon vs. matter interaction. In contrast, the GBM is mainly designed to study transient objects in a lower energy band (10 keV–30 MeV) using mainly photoelectric absorption and Compton scattering.

Carrying these two detectors onboard, *Fermi* was launched successfully by NASA on June 11 2008 from Cape Canaveral Air Force Station using a Delta II rocket. The inclination angle and the elevation of the satellite are 25.5 deg and ~ 565 km, respectively. It orbits the Earth in about 90 minutes. Figure

¹Formerly known as *Gamma-ray Large Area Space Telescope* (GLAST).

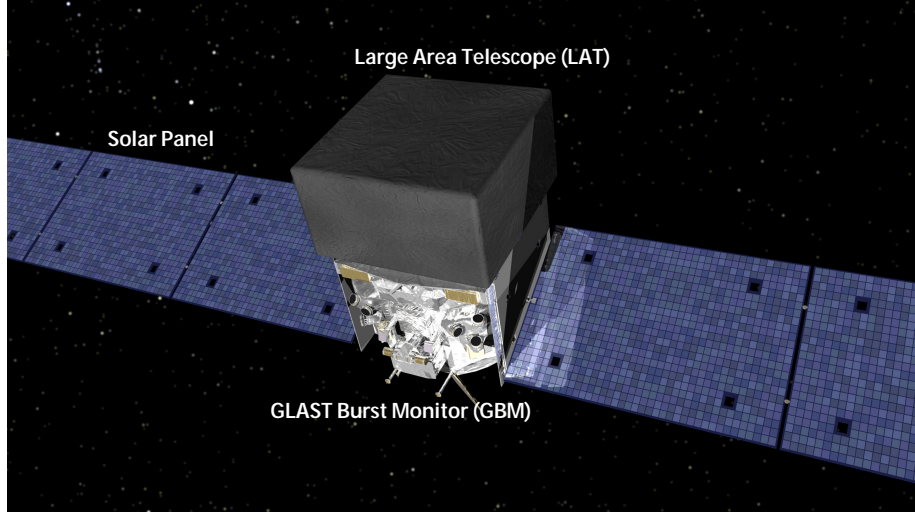


Figure 3.2: An artist's impression of *Fermi Gamma-ray Space Telescope* in orbit (©NASA)

3.2 shows an artist's impression of *Fermi* in orbit.

3.3 The Large Area Telescope

3.3.1 An overview

The Large Area Telescope (*Fermi/LAT*, LAT) is the primary gamma-ray detector onboard the *Fermi Gamma-ray Space Telescope* mission. It surveys the entire sky in the energy range from below 20 MeV to more than 300 GeV. The LAT was designed and built to deeply study high-energy gamma-ray astrophysics that has been explored by pioneering gamma-ray telescopes mentioned in Section 3.1. The LAT has been developed since early 1990's by an international collaboration, which consists of many institutes and universities in France, Italy, Japan, Sweden, and the United States.

Unlike those preceding instruments which used spark chambers, the LAT uses silicon strip detectors (SSDs) to measure the tracks of secondary particles created by incident gamma rays. The technique of particle tracking with SSDs have been extensively developed in the field of high-energy particle physics. As a key technology to overcome some difficulties and limitations of spark chambers in space environment, it was then adopted when the LAT was proposed as a next-generation gamma-ray telescope (Atwood, 1993, 1994). Figure 3.3 shows the LAT gamma-ray sky map of the first 3 months data.

As illustrated in Figure 3.4, the LAT is a pair-conversion gamma-ray telescope consisting of a precision converter-tracker, a calorimeter, and a segmented anticoincidence detector. An incident gamma ray is converted into an electron-positron pair via pair creation process under a collision with a virtual target photon, which is provided by the Coulomb field of a thin high-Z tungsten foil² inside a tracker module. Along their trajectories, these charged secondary particles produce electron-hole pairs in SSDs inside the tracker, and their track patterns are recorded. After passing through the tracker, the electron-positron pair collides against the calorimeter and generates an electromagnetic shower. Repeating bremsstrahlung radiation and pair creation, the shower yields scintillation photons and deposit its energy in the calorimeter. Thus, the incident direction of each gamma-ray is reconstructed from the tracker data, and its energy from those of the calorimeter.

²The first twelve planes of tungsten are each 2.7% radiation length (0.095 mm) in thickness, while the final four are each 18% (0.72 mm).

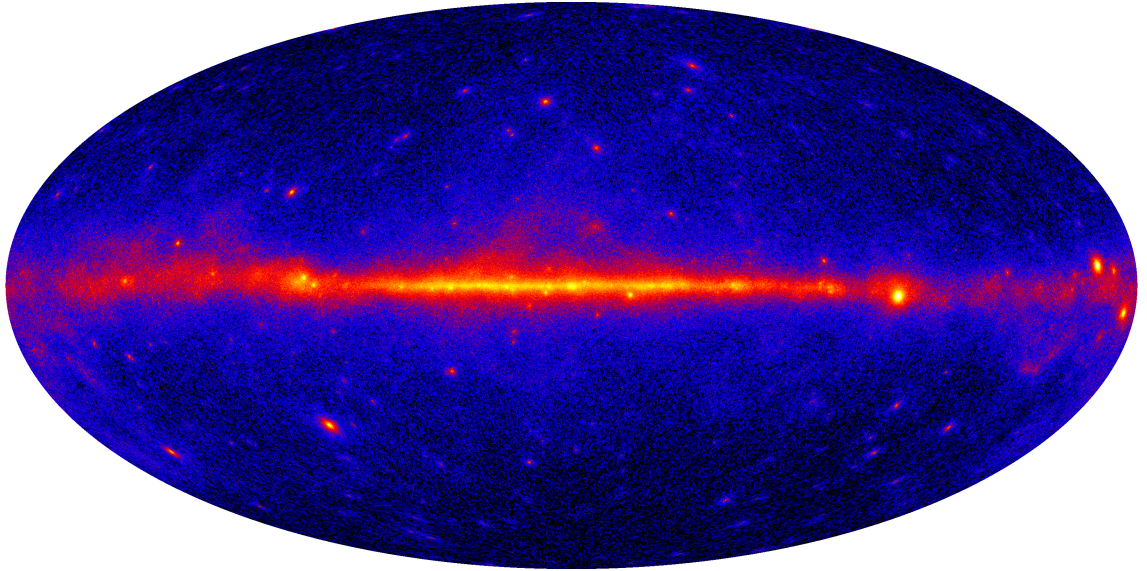


Figure 3.3: The LAT all sky image taken during the first 3 months with Hammer-Aitoff projection in Galactic coordinates.

In addition to gamma rays, an overwhelming number of high-energy cosmic rays (CRs) collide with the detector. If CRs come inside the detector, they create electromagnetic or hadronic showers which would reduce the live time and gamma-ray trigger efficiency of the LAT. In order to remove CR events, the trackers and the calorimeters are covered by plastic scintillators which detect charged particles.

3.3.2 Precision converter-tracker

The LAT tracker, so-called “precision converter-tracker”, consists of 4×4 tracker modules. One module has 18 trays piled up in vertical. Front-end electronics and two layers of single-sided SSDs are installed on top and bottom of each tray. The paired SSD layers have orthogonal sensing directions, one in X- and the other in Y- directions. These piled X-Y pairs enable three dimensional reconstruction of the tracks of secondary particles. Figure 3.5 shows a single tracker module and the completed array of 4×4 modules.

One SSD layer consists of 16 SSDs as shown in Figures 3.5b and 3.6. Each has a very large area of

Table 3.3: The LAT components divided into substructures. Each number is the total number of SSDs or CAL bars in each substructure.

Tower	Tracker (TKR) module				Calorimeter (CAL) module	
	Tray	Layer	Ladder	SSD	Layer	Bar
LAT = 16	288	576	2304	9216	128	1536
1 tower =		1 × TKR		+	1 × CAL	
TKR = 18	18	36	144	576		
1 tray = 2		2	8	32		
1 layer = 4			4	16		
1 ladder = 4				4		
CAL =					8	96
					1 layer =	12

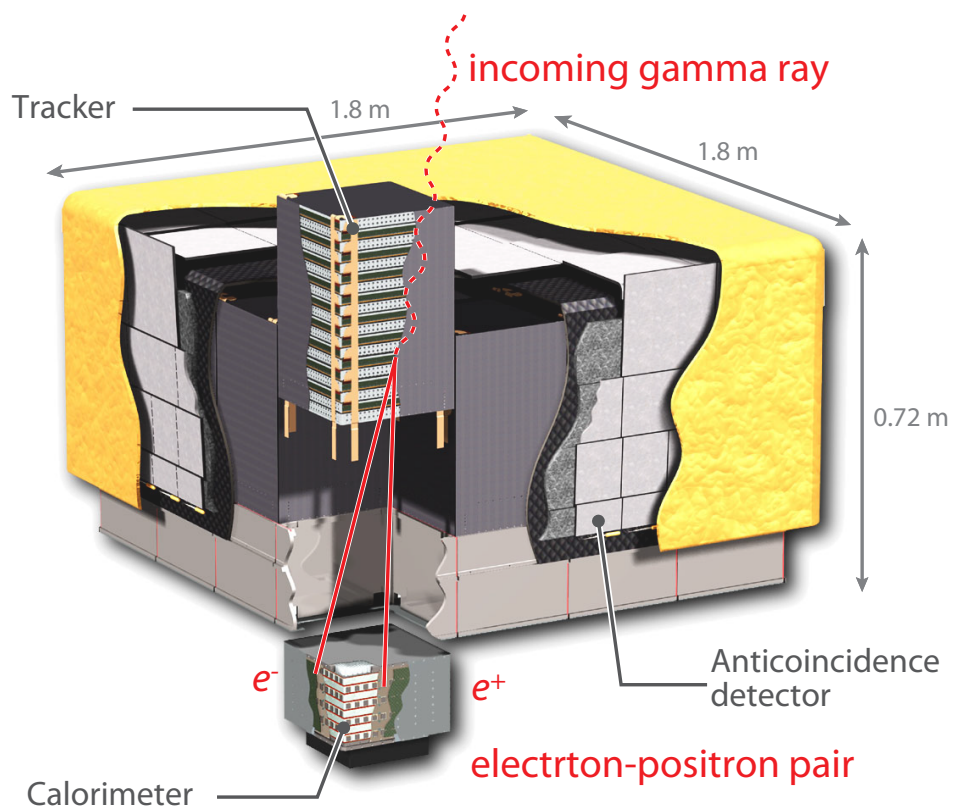


Figure 3.4: A schematic view of the LAT working as a pair-conversion telescope. An incoming gamma ray is converted into an electron-positron pair in the tracker through pair creation process. The tracks of secondary particles are recorded by the tracker, and their energy deposit is measured by the calorimeter (from Atwood et al. 2009 with modification).

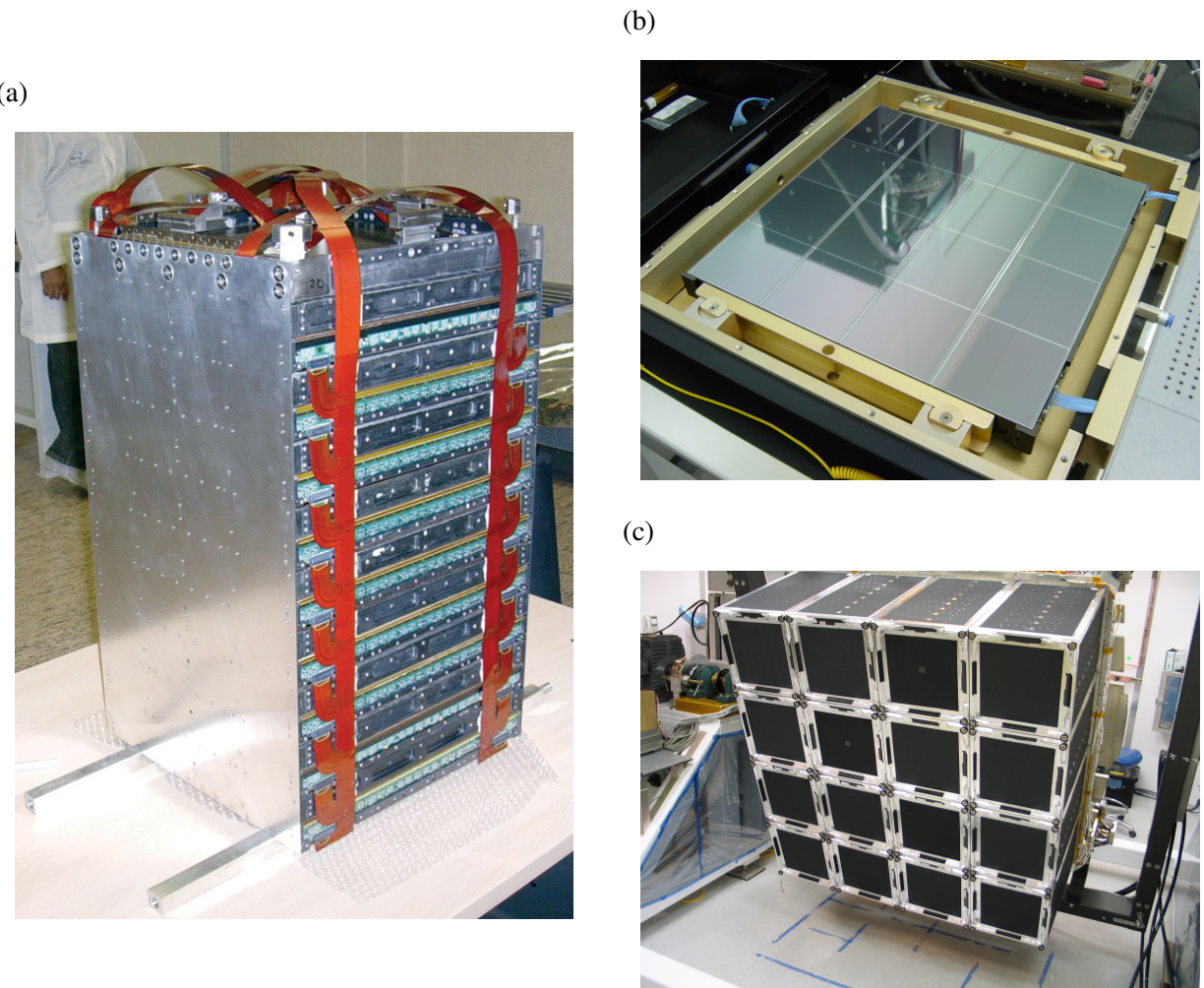


Figure 3.5: The LAT Tracker. (a) A single tracker module with sidewalls removed. (b) A single tracker layer. The shiny 16 surfaces are SSDs. (c) The completed tracker array before the Anticoincidence Detector is mounted (©NASA).

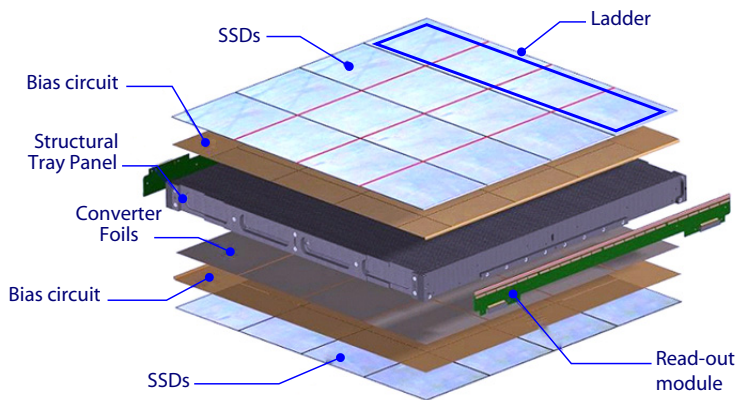


Figure 3.6: A schematic view of a LAT tracker tray (Belli et al., 2007)

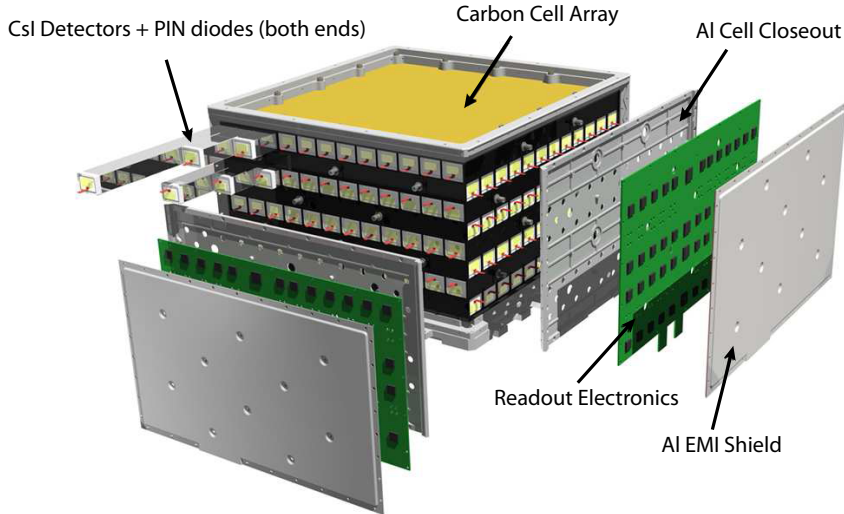


Figure 3.7: A schematic view of the LAT calorimeter module (Atwood et al., 2009).

$8.95 \times 8.95 \text{ cm}^2$ with 1 mm wide inactive edges, and a thickness of $400 \mu\text{m}$. Total 384 p+ strips are implanted on an n-type substrate, and $56 \mu\text{m}$ wide aluminum readout strips are overlaid on them with $228 \mu\text{m}$ pitch³. Four pieces of SSDs are aligned linearly and bonded edge by edge with epoxy. This set forms a “ladder” which has 35 cm long strips. Four “ladders” are aligned with 0.2 mm gaps, so that 16 SSDs altogether cover an area of $35 \times 35 \text{ cm}^2$ (Figure 3.6).

Of the 18 trays in a module, the top 16 trays have tungsten foils which convert gamma rays into electron-positron pairs. The first 12 trays (“front”) have thin tungsten foils, the radiation length of which is 0.03. The thickness is optimized so as to provide a sufficient conversion efficiency, while avoiding degradation of angular resolution⁴ (PSF) for low energy photons due to multiple scatterings of the electron-positron pair. The second 4 trays have ~ 6 times thicker foils to maximize the effective area. The radiation length of supporting material in each tray is 0.014, thereby totaling 1.5 vertical radiation length in the tracker.

3.3.3 Calorimeter

Each tracker module has one calorimeter module beneath it. A tracker module and the associated calorimeter module, combined together, from a “tower” (Table 3.3). The main purposes of the calorimeter is to determine the energy of each incident photon by measuring scintillation photons in an electromagnetic shower formed by secondary particles, and to image the development of the shower. Each calorimeter module has 96 CsI(Tl) crystal bars, each with a size of $2.7 \times 2.0 \times 32.6 \text{ cm}^3$. The crystals are optically isolated from one another, in order to retain the positional information of the shower. As illustrated in Figure 3.7, 12 crystals are aligned in horizontal, and 8 such layers are piled in vertical.

One large and one small PIN photodiodes are attached on each end of a crystal bar. The larger one has an area of 147 mm^2 and is used to measure low-energy showers in the energy range of 2 MeV – 1.6 GeV. The smaller one has an area of 25 mm^2 , and is used for a higher energy range of 100 MeV – 70 GeV

³ $8.95 \text{ cm} = 384 \times 228 \mu\text{m} + 2 \times 1 \text{ mm}$

⁴Function of probability distribution of arrival direction.

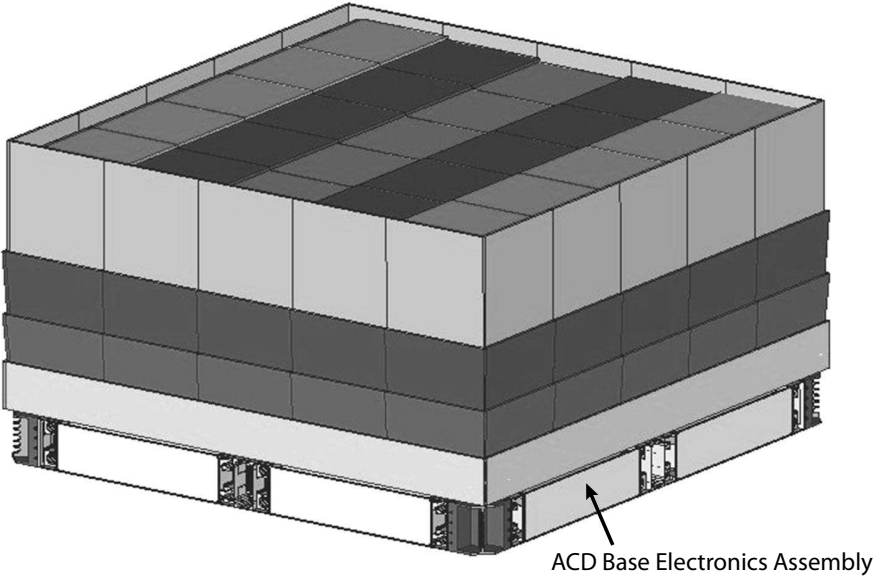


Figure 3.8: A schematic view of the LAT Anticoincidence Detector (Atwood et al., 2009).

because it is less tolerant to signal saturation. By using the photodiodes on both ends, it is possible to reconstruct the one-dimensional position where scintillation photons are induced in the bar. The position along the bar is determined by differences of the light output from the two ends. Accordingly, the calorimeter is able to measure the energy of incident photon and to image the three-dimensional shower development.

3.3.4 Anticoincidence Detector (ACD)

The tracker and the calorimeter are sensitive not only to gamma rays, but also to charged CRs. Electrons and positrons collide with the detector and produce electromagnetic showers. CR protons, alpha particles, CNO and Fe nuclei produce hadronic showers. These unwanted CR events must be removed to minimize the dead time and background rate, and maximize the trigger efficiency.

The anticoincidence detector (ACD) has been designed to remove such charged CRs using plastic scintillators. The required rejection efficiency of charged particles is at least 0.9997. The ACD consists of segmented 89 plastic scintillator tiles and 8 scintillating fiber ribbons. They are arranged in 5×5 tiles placed on the top of the LAT, and $5 \times 3 + 1$ tiles on each side wall. Neighbouring tiles overlap on one edge to minimize ineffective gaps between them. Each tile is coupled with wavelength shifting fibers and 2 photomultiplier tubes. The ribbons placed under the tiles are used to cover remaining gaps. Figure 3.8 shows a schematic view of the ACD.

3.3.5 Data acquisition and event processing

Incoming photons and CRs create their tracks in the tracker and deposit their energies in the calorimeter. These signals are used as the level 1 trigger of the LAT data acquisition system. A simplified diagram of the system is shown in Figure 3.9. Each tower, consisting of a tracker module and a calorimeter module, has a Tower Electronic Module (TEM) under the calorimeter module. A TEM can generate a trigger request when the tower satisfies either of the following conditions. (1) Some tracker channels of consecutive three or more (x, y)-planes give signals which exceed over a predefined threshold. (2) Measured energy of any crystal bar in the calorimeter module exceeds predetermined low-energy or

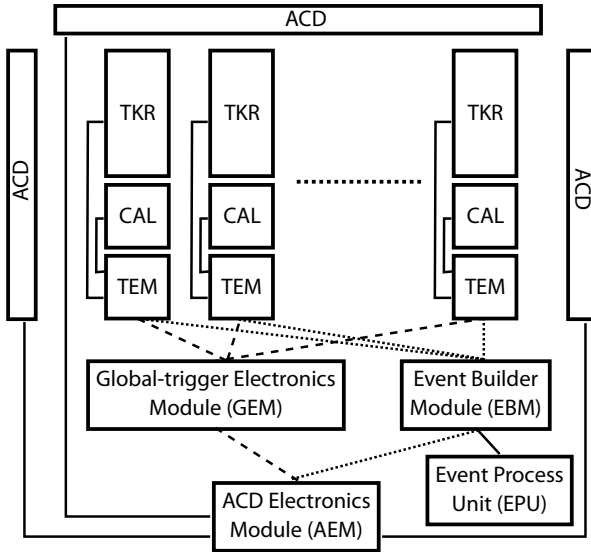


Figure 3.9: A schematic view of the LAT data acquisition system.

high-energy threshold. Then a trigger request is sent to Global-trigger Electronics Module (GEM) which communicates with all the 16 TEMs. Once the GEM accept the request from a TEM, an accept message is broadcasted to the 16 TEMs, and to the ACD Electronics Module (AEM) which controls the ACD like the TEMs. After receiving the accept message, all the TEMs and the AEM send the information of their tracks and energies to Event Builder Module (EBM).

The typical trigger rate at this stage is 2–4 kHz. However this rate must be reduced to ~ 400 Hz so that the triggered event data can be downlinked to ground within limited bandwidth of the LAT (~ 1 Mbps). Since the trigger rate of celestial gamma-ray events is estimated to be only ~ 2 Hz typically, the data are dominated by CR events which should be removed as much as possible. Therefor, for each valid trigger, all the information provided by the TEMs and AEM is sent to the EBM and reconstructed as an event. The LAT has an onboard software filter which rejects events if they are unlikely to be photons. The filter is performed by Event Process Unit, in cooperation with the EBM. The minimum instrumental dead time per event readout is $26.5\ \mu\text{s}$. Thus the total live-time fraction of the LAT is about 90% at a trigger rate of 4 kHz.

The reduced event data are downlinked to the *Fermi* Mission Operations Center and forwarded to the LAT Instrument Science Operations Center. They are reconstructed by a batch farm of 100 computing cores, and then are delivered to end users for scientific analyses. During the event reconstruction processes, the arrival direction and time, the particle (or photon) type, the total energy, and additional information of each event are determined. The reconstruction process is divided into mainly two sub processes; track reconstruction and energy reconstruction, to be explained below.

The track reconstruction plays an important role in determination of the arrival directions of photons. As we have described in the previous sections, charged particles in electromagnetic or hadronic showers induced by incident particles leave their tracks in SSDs. This is because a charged particle passing through a silicon strip create electron-hole pairs along their trajectory. Since this signal is read by orthogonal (x, y) layers stacked in vertical, the tracks are recorded in three dimensions. However, the recorded (x, y, z) coordinates are not simply used to extrapolate the arrival direction due to several reasons. First, SSDs have inefficient regions between neighboring strips in addition to their edges. Particles which passed such regions are not recorded. Second, incident gamma rays can be converted to electron-positron pairs outside the tungsten foils. In this case, the determination of the first interaction point becomes less accurate. Third, secondary particles are scattered by the material of the tracker. This

multiple scattering changes the velocity directions of the particles. Forth, an (x, y) plane cannot determine the hit positions when multiple particles pass through the same strip. These effects must be treated by a statistical approach. Figure 3.10 shows examples of real triggered and reconstructed events.

The first step for the reconstruction of an arrival direction is to connect the first interaction point (namely triggered or hit strip) and the “energy centroid” in the calorimeter. The latter is calculated by using the three-dimensional information of the energy deposit in the crystal bars. This is based on an assumption that the energy centroid lies on the trajectory. If a subsequent hit is found to be close to the line between the first hit and the energy centroid, a trial track is generated. If there are multiple possible candidates in the first layer, corresponding trial tracks are generated. Subsequent hit patterns are then incorporated to find the actual track, together with their positional errors and energy-dependent multiple scattering errors. The Kalman filter method is adopted in this track finding (Kalman, 1960; Frühwirth, 1987). Based on χ^2 and the number of hits, the track candidates are ordered from “best” to “worse” according to the results of Kalman filtering processes. The method provides the χ^2 , the number of hits. The SSD hits used in the best track are flagged as “used”.

The rest of hits are also used in the next step. This process is similar to the first one. However the energy centroid is not used as a second hit point. An unused hit is randomly chosen from the next closest layer to the calorimeter. Then multiple tracks are generated and fitted using the Kalman filter similarly. These tracks are shown in Figure 3.10 with blue lines. Reconstructed tracks are combined, and vertices are generated.

The energy deposit in the calorimeter does not fully reflect the energy of the incident gamma ray. This is because showers develop outside the crystal bars. This leakage energy is estimated using the reconstructed tracks. The reconstructed energy is finally used to refit the tracks. The energy consumed in the tracker is also taken into account to estimate the incident energy.

After the track reconstruction, vertexing, and energy reconstruction, all events are analyzed to determine the accuracy of estimations of the total energy, the arrival direction, and the probability to be a gamma ray. These estimations are obtained by a classification tree method. At first, all events are at the “root” of the tree. They are classified at “branches” of conditions. Each classification criteria are determined by the probability functions of many parameters calculated with Monte Carlo simulations.

Depending on our scientific objectives, we may adopt very tight background rejections under the sacrifice of the signal acceptance, or looser cuts to maximize the signal photon number. This is realized by three cut levels, called “*TRANSIENT*”, “*SOURCE*”, and “*DIFFUSE*” according to three cut levels of cosmic-ray like events. “*TRANSIENT*” is the loosest cut in which cosmic-ray event rate is relatively high. It is optimized for use in analyses of transient objects such as gamma-ray bursts. This class includes 2 Hz or less residual cosmic-ray background, which corresponds to no more than one background event every 5 seconds inside a 10° radius. Thus, residual cosmic-ray events are negligible for transient events of an order of a second. In contrast, “*DIFFUSE*” class is the tightest cut optimized to analyses of steady point sources and diffuse emission. Its cosmic-ray background rate is 1 to 2 orders of magnitude lower than that of the “*TRANSIENT*” class. Figure 3.11 shows the residual cosmic-ray background, normalized to the extragalactic diffuse gamma-ray emission measured by the EGRET (Sreekumar et al., 1998).

Among the background CR events, a part of them consists of gamma rays which cannot be removed by the ACD. For example, a CR positron can annihilate on the surface of the LAT and emits two gamma rays. We are not able to distinguish these photons from real celestial gamma-ray events. CR protons can also produce π^0 's and gamma rays outside the LAT. The contribution from these non-celestial gamma-ray events is estimated to be less than 10% of the flux of the extragalactic diffuse gamma-ray emission. in addition, the Earth albedo neutrons are not remove by the ACD. However since most of them comes from the direction to the Earth, they do not dominate the background level in the LAT FOV.

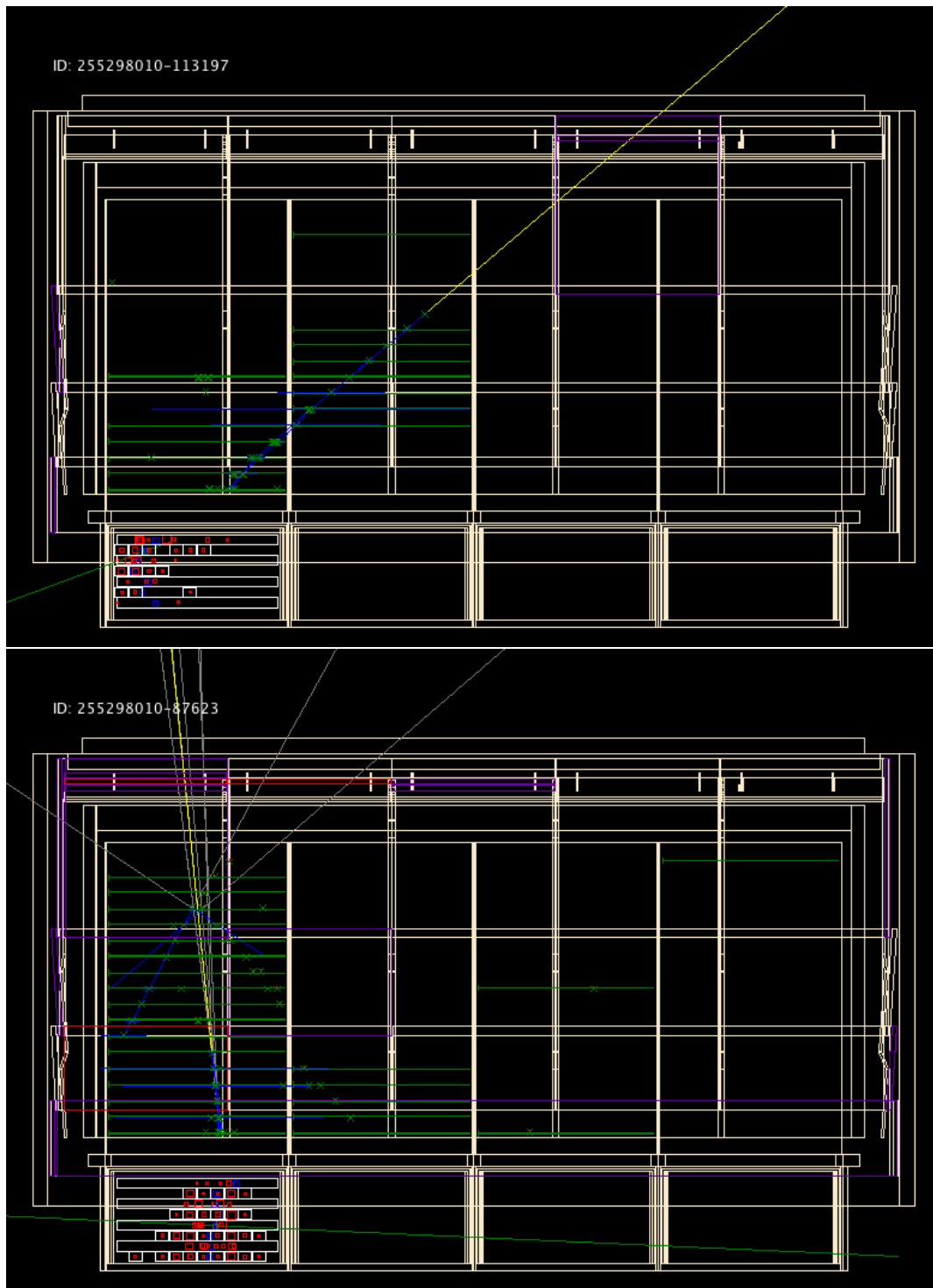


Figure 3.10: Event examples. (top) An example of gamma-ray like event with a reconstructed energy of 1.55 GeV. (bottom) That of cosmic-ray like event with a reconstructed energy of 10.1 GeV. The Yellow line shows the reconstructed arrival directions. The green lines and crosses show SSD hits. Small red rectangles show crystal bars exceeding the thresholds. Red or purple lines show ACD hits.

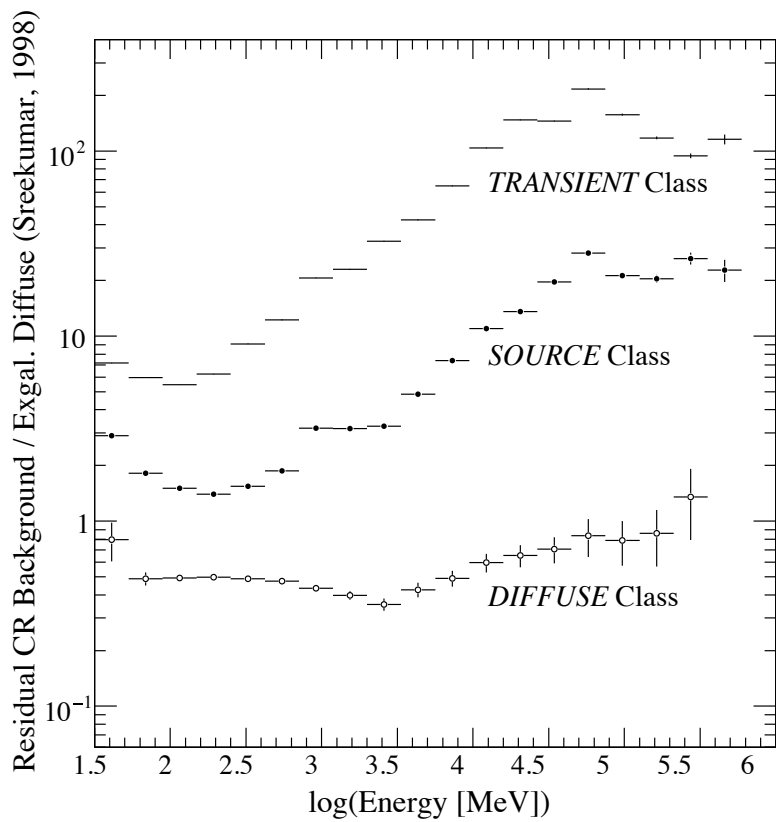


Figure 3.11: The residual background induced by cosmic rays, obtained in the three cut levels (Atwood et al., 2009). They are shown divided by the extragalactic gamma-ray background estimation based on an EGRET measurement (Sreekumar et al., 1998).

Table 3.4: Summary of instrumental performance of LAT (Atwood et al., 2009)

Parameter	Value or Range
Energy range	20 MeV - 300 GeV
Effective area at normal incidence	9,500 cm ²
Energy resolution (equivalent Gaussian 1 σ):	
100 MeV - 1 GeV (on axis)	9%-15%
1 GeV - 10 GeV (on axis)	8%-9%
10 GeV - 300 GeV (on-axis)	8.5%-18%
> 10 GeV (> 60° incidence)	≤ 6%
Single photon angular resolution (space angle) on-axis, 68% containment radius:	
> 10 GeV	≤ 0.15°
1 GeV	0.6°
100 MeV	3.5°
on-axis, 95% containment radius	< 3 × $\theta_{68\%}$
off-axis containment radius at 55°	< 1.7 × on-axis value
Field of View (FOV)	2.4 sr
Timing accuracy	< 10 μ sec
Event readout time (dead time)	26.5 μ sec
GRB location accuracy on-board	< 10'
GRB notification time to spacecraft	< 5 sec
Point source location determination	< 0.5'
Point source sensitivity (> 100 MeV)	3×10^{-9} photon/cm ² /s

3.3.6 Sensitivity and instrumental performance

To understand the LAT response against gamma rays and charged particles, extensive studies have been conducted in accelerator beam tests (Atwood et al., 2000; do Couto e Silva et al., 2001), in balloon flights (Thompson et al., 2002; Mizuno et al., 2004), and by Monte Carlo simulations based on Geant4 program. On-orbit detector calibrations have been done in the early stage just after the launch of *Fermi* (Abdo et al., 2009b).

Figure 3.12a shows on-axis effective areas of the LAT versus gamma-ray energy for the three event classes. They are almost flat in the energy range above 1 GeV. Even employing the tight cut of “*DIF-FUSE*” class in cosmic-ray background rejection (Subsection 3.3.5), its signal acceptance is more than 80% compared to the “*TRANSIENT*” class. Figure 3.12b shows the effective area of the “*SOURCE*” class as a function of gamma-ray energy for the on-axis (solid) and an off-axis (60° dashed) angles. Figure 3.12c illustrates the energy dependence of the angular resolution⁵ of the “*SOURCE*” class for gamma-rays pair-converted in the thin section of the tracker. When the conversion takes place in the thick section, the angular resolution becomes about twice worse than this. Figure 3.12d shows the energy dependence of the energy resolution of the “*SOURCE*” class.

Figure 3.13 shows a simulated sensitivity of the LAT with four different time scales. In high Galactic latitude regions, the maximum sensitivity for point sources is expected to be 3×10^{-9} photon cm⁻²s⁻¹.

⁵68% containment radius

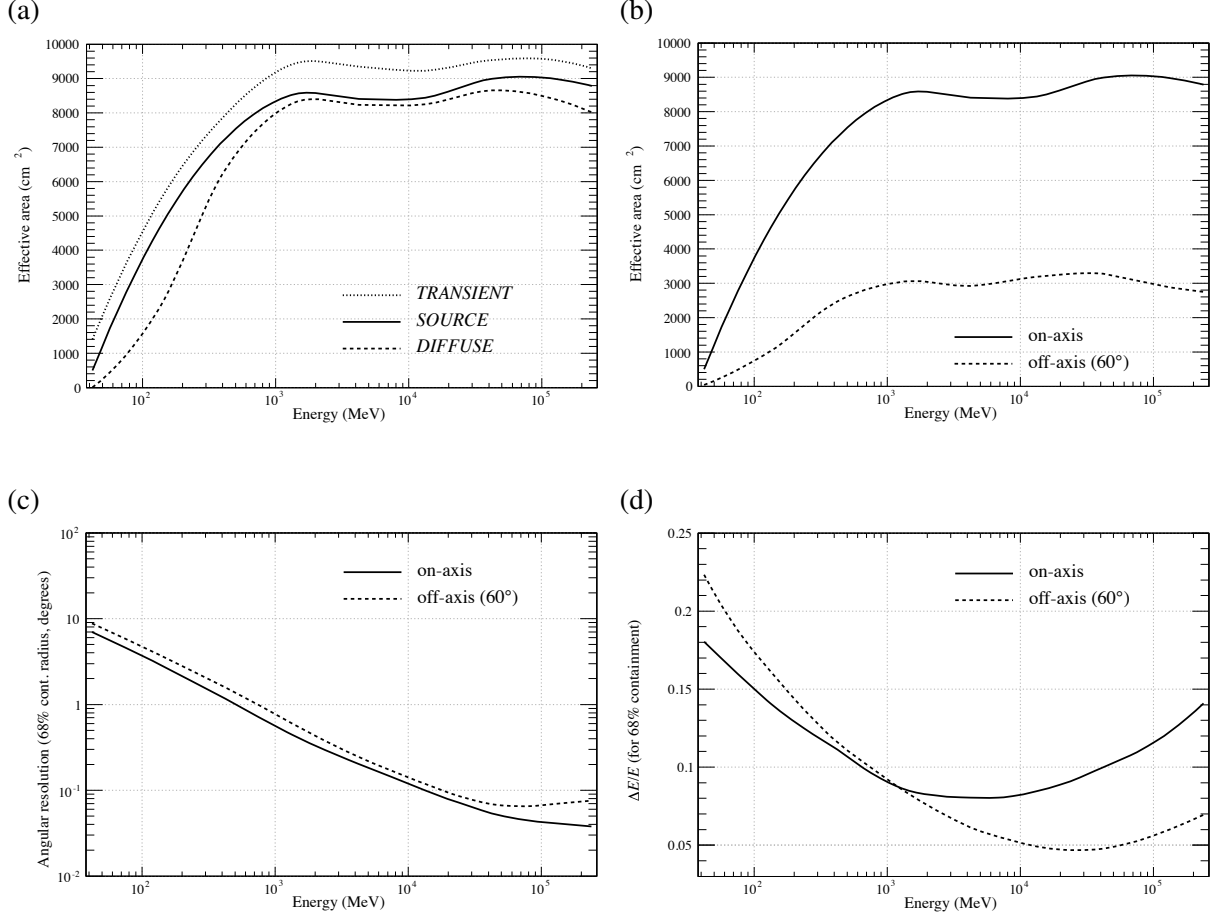


Figure 3.12: The LAT responses to gamma rays (Atwood et al., 2009). (a) Effective areas of the three event classes, shown as a function of gamma-ray energy at normal incidence. The dashed, solid and dotted lines show **DIFFUSE**, **SOURCE** and **TRANSIENT** classes, respectively. (b) A comparison of the effective area between the on-axis (solid) and 60° off-axis incidence (dotted), both for the “**SOURCE**” class. (c) Angular resolution (68% containment radius) versus gamma-ray energy. The solid and dotted lines show on-axis and 60° off-axis conditions, respectively, both for conversions in the thin section of the tracker. (d) The on-axis (solid) and 60° off-axis (dotted) energy resolutions (68% containment radius) versus gamma-ray energy.

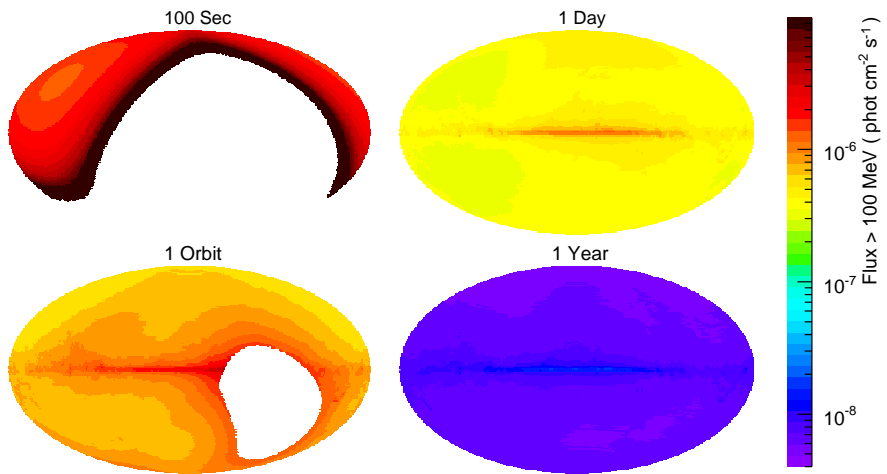


Figure 3.13: Expected LAT source sensitivity for exposures on various timescales. Each map is an Aitoff projection in Galactic coordinates. In standard sky-survey mode, a nearly uniform exposure is achieved every 2 orbits, wherein every sky region is viewed for ~ 30 min every 3 hours (Atwood et al., 2009). The LAT sensitivity in the Galactic plane is worse than that in high-latitude regions due to the strong diffuse emission from the ISM.

Chapter 4

OBSERVATIONS

4.1 Observations

Since August 4 2008 as of July 2009, *Fermi* has been continuing its nominal science operation in an all-sky survey mode. In order to achieve as uniform exposure as possible over the sky, the primary observation mode of *Fermi* is the “scanning” mode, while occasionally performing short pointing observations for specific science operations such as calibrations and multiwavelength campaigns. As illustrated in Figure 4.1, the normal to the front surface of the instrument is pointed to $+35^\circ$ (-35°) from the instantaneous local zenith direction towards the north (south) pole of the orbit in the north-sky (south-sky) scanning mode. North and south modes are carried out in alternate orbits every ~ 180 minutes. Figure 4.2 shows the LAT directions between MET=245000000 and 247000000 (Oct 6 2008 and Oct 29 2008) as an example. The LAT continues sequential pointing except for transitions between the northern and southern sky, and two “sun avoidance” periods needed to achieve effective performance of the solar panel. The nonuniformity in exposure will be eliminated after long-term observations.

The Orion region has also been observed by the LAT with an almost uniform exposure. Figure 4.3 shows the total exposure of the region in an energy band of 3.56 GeV – 4.74 GeV. The exposure is kept uniform within $\pm 10\%$. The exposures of other energy bands are similar because the LAT acceptance is almost flat above 1 GeV (see Figure 3.12a).

4.2 Event Selection

For the present study, we accumulated 9 months of data of the “*DIFFUSE*” class from August 4 2008 to May 19 2009. The start and stop times of the selected observation term are 239557413 and 264000000 in Mission Elapsed Time (MET¹), respectively. The event data was classified into two data sets. One includes those events of which, the arrival directions were reconstructed within a 20° radius region centered at $(l, b) = (211^\circ, -17^\circ)$. Hereafter we refer to these events and the region as “data set 1” and ROI (region of interest) 1. The other contains events within a 15° radius around $(l, b) = (210^\circ, -25^\circ)$, which are referred to as “data set 2” and ROI 2. We note that two data sets are not exclusive mutually. The Orion A and B clouds are located at near the center of ROI 1 and at the edge of ROI 2. The data set 1 and 2 are used in different analyses. The former is for our main analysis. Meanwhile the latter is used in maximum likelihood fitting analyses to validate emission models. Since ROI 2 does not overlap the Galactic plane, a fitting process is not strongly affected by the plane which is optically thick and includes many unresolved point sources.

To both these data sets, we applied a “zenith cut” selection to reduce Earth albedo gamma rays produced in the Earth’s atmosphere by hadronic or electromagnetic cosmic-ray air showers. The production

¹Time zero of MET is set at 00:00 UTC on January 1 2001.

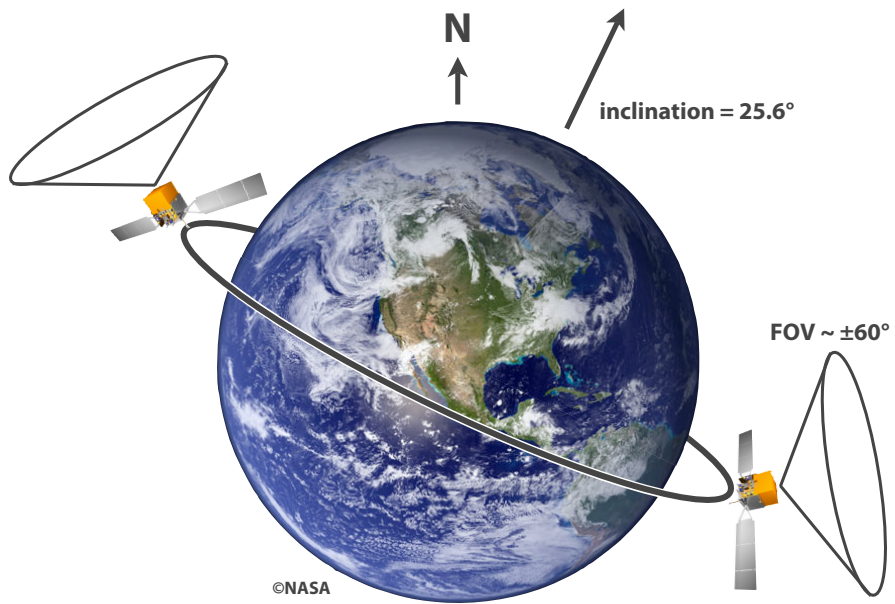


Figure 4.1: A schematic view of the scanning mode of *Fermi*. This is the case of north-sky scanning.

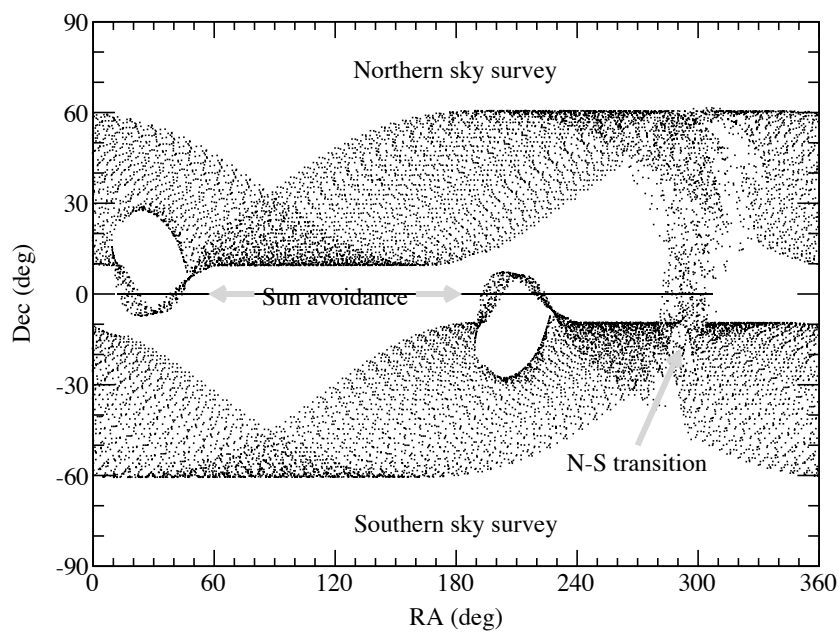


Figure 4.2: An example of the pointing history of the LAT, between MET=245000000 and 247000000. Each data point corresponds to the on-axis direction of the LAT in 120 seconds intervals.

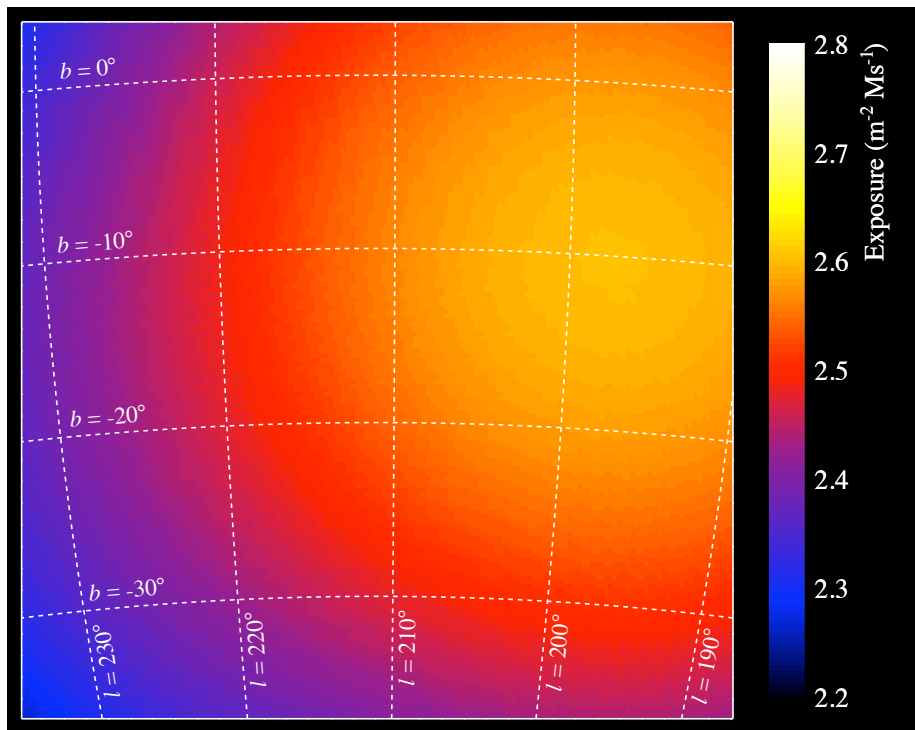


Figure 4.3: The exposure map of the Orion region in an energy range of 3.56 GeV – 4.74 GeV. Since the on-axis effective area of the LAT is $\sim 1 \text{ m}^2$ above 1 GeV, the exposure values are roughly equivalent to observation times in unit of Ms (10^6 seconds).

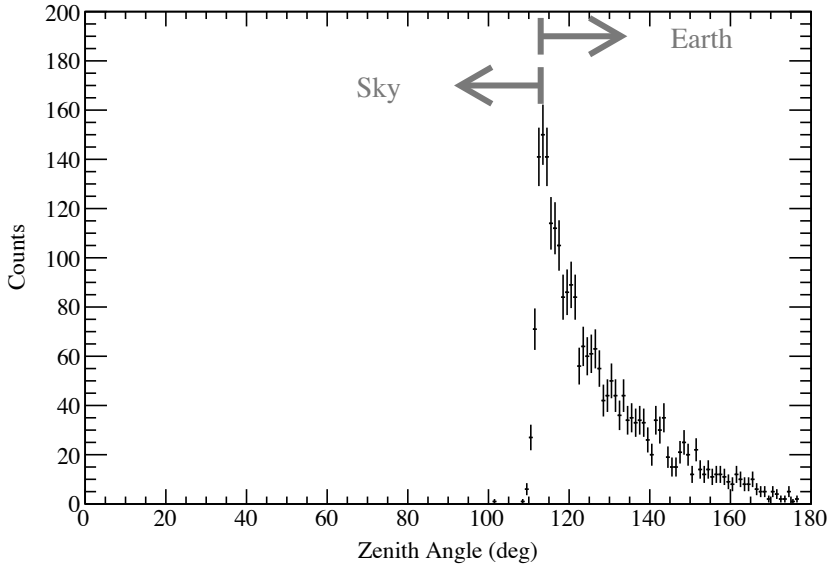


Figure 4.4: Zenith angle dependence of the Earth-albedo gamma-ray counts. The LAT angular resolution is included.

Table 4.1: The criteria of event selections.

Name	Center coordinates (l, b)	Radius	Zenith cut	Energy	MET
Data set 1	($211^\circ, -17^\circ$)	20°	$< 100^\circ$	200 MeV – 20 GeV	239557413–264000000
Data set 2	($210^\circ, -25^\circ$)	15°			

mechanism of these gamma rays is very similar to that inside ISM (Section 2.3). As seen from *Fermi*, the Earth’s horizon is located at a zenith angle of $\sim 113^\circ$ ², so the region below is dominated by the albedo gamma rays. Figure 4.4 shows the zenith angle dependence of gamma-ray counts actually observed by the LAT above 200 MeV, where this effect is very clearly seen. The data were taken in “nadir³ pointing mode” to purposely study the albedo emission. Since celestial gamma rays which skim over the surface of the Earth cannot be distinguished from the albedo emission, in data set 1 and 2, we excluded those events, of which the reconstructed arrival zenith directions are above 100° .

The energy band of the data sets was limited to 200 MeV – 20 GeV in order to reduce the effect of systematic uncertainties at lower energies and of in recognition of limited statistics at higher energies. Another aim of the energy cut at 200 MeV is to reduce the effect of low angular resolution.

The all criteria of our event selections are listed in Table 4.1. The zenith cut, the energy cut, and the MET interval are the same for the two data sets. The count maps of the data sets are shown in Figure 4.5. The Orion A, B, and Monoceros R2 clouds are clearly visible in the maps (see also Figures 2.12 and 2.15). Discrete bright points are gamma-ray point sources, and bright extended emission around $b = 0^\circ$ is the Galactic plane.

² $113^\circ \simeq 180^\circ - \arcsin(R/(R + h))$, where $R = 6400$ km is the Earth’s radius and $h = 550$ km is the elevation of *Fermi*.

³The opposite direction of the zenith.

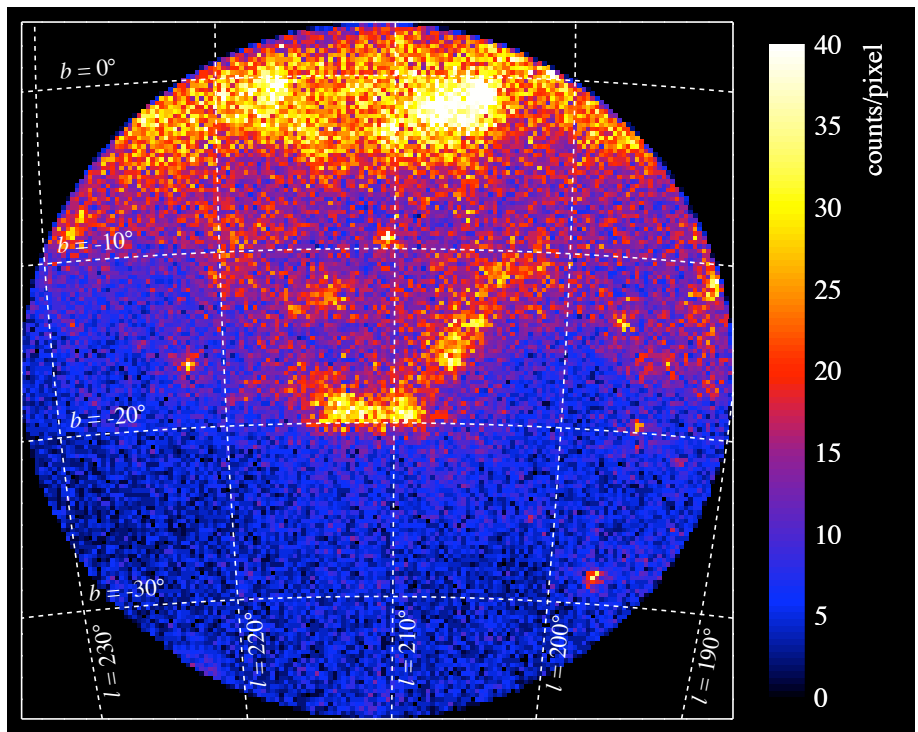


Figure 4.5: A gamma-ray count map of ROI 1 in Hammer-Aitoff projection. The data set 1 binned in $0.25^\circ \times 0.25^\circ$ pixels.

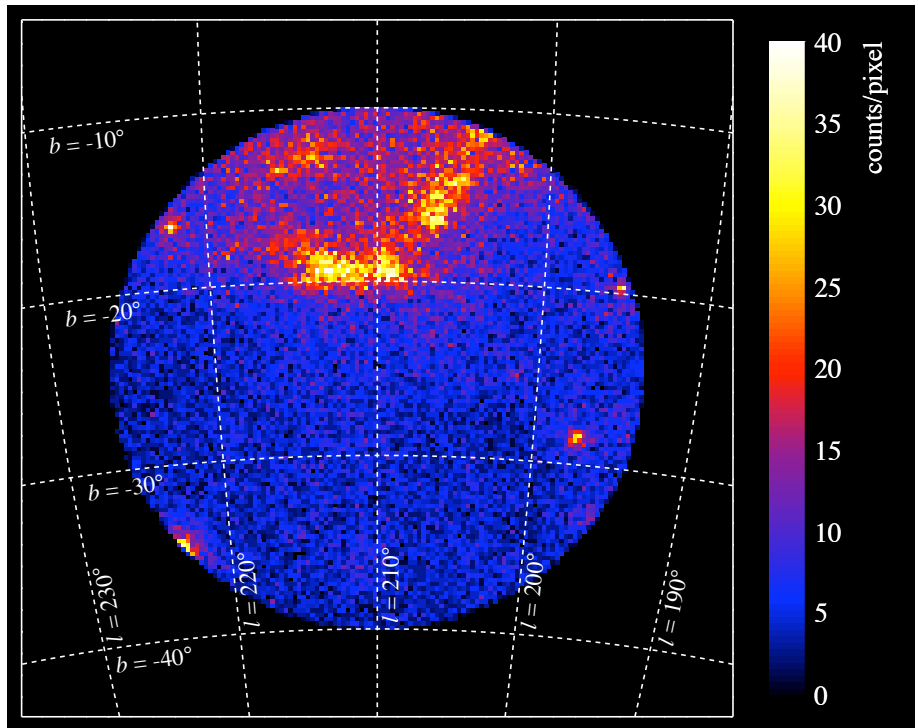


Figure 4.6: A gamma-ray count map of ROI 2.

Chapter 5

DATA ANALYSIS AND RESULTS

5.1 Gamma-Ray Emission Components

The event data sets obtained in Chapter 4 consists of several components, originating from different physics processes and sources as explained in Section 2.3. Possible gamma-ray sources are listed in Table 5.1. Among them, what we are interested in are π^0 gamma rays and bremsstrahlung radiation from the Orion MCs (Ⓐ and Ⓨ). In order to study and extract these components, we first examine in Section 5.2 if the emission from H I and H₂ can be explained by π^0 and bremsstrahlung emission. Then we subtract all components other than Ⓩ and Ⓨ from the data sets in Subsection 5.4.1; the dominant components are π^0 and bremsstrahlung emissions from H I gas (Ⓑ and ⓑ). Similar emission from H II gases (Ⓒ and Ⓧ) also exist, but their contributions are known to be small because they are relatively hot and hence less dense than the other forms of hydrogen. IC emission (Ⓖ) spreads over the ROIs according to the distributions of CR electrons and interstellar radiation fields, and is relatively small compared to Ⓩ, ⓑ, Ⓨ, and ⓑ.

In addition to these diffuse components, of course there exist gamma-ray point sources such as pulsars, blazars, and so on. If a gamma-ray source is strong enough, the LAT can detect it at a high significance level, while weak sources which cannot be detected individually are considered to form an apparently diffuse background emission. If these objects are isotropically distributed in the ROIs, and if the number of such objects is large, they can be treated as an “isotropic” background, with a constant spectral shape and flux over the ROIs (①). The last component is residual CR events which are misclassified by the event reconstruction process (②, see Figure 3.11). We treat ① and ② as a single isotropic component.

Of these 10 components, Ⓩ, ⓑ, Ⓨ, and ⓑ are thought to be proportional to the densities of CRs and the ISM. Thus, the gamma-ray surface brightness at an energy E and Galactic coordinates (l, b) will be written as

$$\Phi(l, b, E) = A(E)W_{\text{CO}}(l, b) + B(E)N(\text{H I})(l, b) + C(E)N(\text{H II})(l, b) \quad (5.1)$$

$$+ \Phi_{\text{IC}}(l, b, E) + \sum_i D_i(E)\delta(l_i, b_i) + F(E). \quad (5.2)$$

Here $A(E)$, $B(E)$, and $C(E)$, all proportional to the CR flux at the clouds, are line-of-sight averaged gamma-ray emissivities of CO, H I gas, and H II gas, respectively (Ⓐ+Ⓨ, ⓑ+ⓑ, and ⓒ+Ⓧ), and Φ_{IC} is inverse Compton emission (Ⓖ). $D_i(E)$ and $\delta(l_i, b_i)$ are the flux and position of the i th point source, respectively (④), while $F(E)$ is the isotropic component (①+②). If we neglect point sources, and put $C(E)$ and Φ_{IC} into the isotropic component, equation (5.2) is simplified as

$$\Phi(l, b, E) = A(E)W_{\text{CO}}(l, b) + B(E)N(\text{H I})(l, b) + F(E). \quad (5.3)$$

Table 5.1: Gamma-ray emission components

	Component	Type
(A)	π^0 (H_2)	Diffuse
(B)	π^0 (H I)	Diffuse
(C)	π^0 (H II)	Diffuse
(D)	Bremsstrahlung (H_2)	Diffuse
(E)	Bremsstrahlung (H I)	Diffuse
(F)	Bremsstrahlung (H II)	Diffuse
(G)	Inverse Compton	Diffuse
(H)	Galactic or extragalactic point sources	Point source
(I)	Unresolved point sources	Isotropic
(J)	Residual CR background	Isotropic

In these equations, the term $A(E)W_{\text{CO}}(l, b)$ in fact represents the gamma-ray emission from H_2 gas, but here we express it using the observable W_{CO} . If the H_2 column density is proportional to W_{CO} with a constant of proportionality X_{CO} , and if the gamma-ray emissivity per hydrogen atom is the same in H I gas and H_2 gas, we obtain

$$\frac{A}{2B} = X_{\text{CO}}. \quad (5.4)$$

5.2 Validation of π^0 Emission

5.2.1 Gamma-ray emission from H I

Whether the Galactic π^0 emission traces the ISM distribution and the CR spectra has been debated since the EGRET “discovery” of “GeV excess”, which cannot be explained by the π^0 emission calculated using the CR spectra observed at the Earth (Hunter et al., 1997). To settle the issue, we first analyze component (B) in the data set 2.

As shown in Figures 2.12 and 4.5, the lower half ($b < -25^\circ$) of ROI 2 does not contain known MCs, while the upper half includes the Orion clouds. Therefore, equation (5.3) can be simplified in the lower half as

$$\Phi(l, b, E) = B(E)N(\text{H I})(l, b) + F(E). \quad (5.5)$$

In order to calculate $B(E)$ and $F(E)$, we studied the correlation between $\Phi(l, b, E)$ and $N(\text{H I})(l, b)$ in 7 energy bands between 200 MeV, 266 MeV, 355 MeV, 474 MeV, 632 MeV, 1.12 GeV, 2.66 GeV, and 20.0 GeV. First, as shown in Figure 5.1, we prepared count maps in the 7 energy bands. Eight bright point sources in the region were masked so that we can neglect their contribution, (H), in equation (5.2). These count maps were rebinned into large pixels as shown in Figure 5.2 so that the point spread function (PSF) of the LAT (Figure 3.12c) can be neglected. Figure 5.3 shows H I maps of the same region rebinned in the same pixel sizes, after weighting by the energy dependent LAT exposure. Thus, we generally observe a close similarity between the gamma-ray and H I maps in the bottom half region of each map. The masked H I map before rebinning is shown in Figure 5.4b.

If the finite PSF width can be neglected and the point source masking in Figure 5.1 works properly, the gamma-ray count in the i th pixel, $N_\gamma(E, i)$, is written as

$$N_\gamma(E, i) = B(E) \times N'(\text{H I})(E, i) + F(E) \times \text{Exposure}(E, i). \quad (5.6)$$

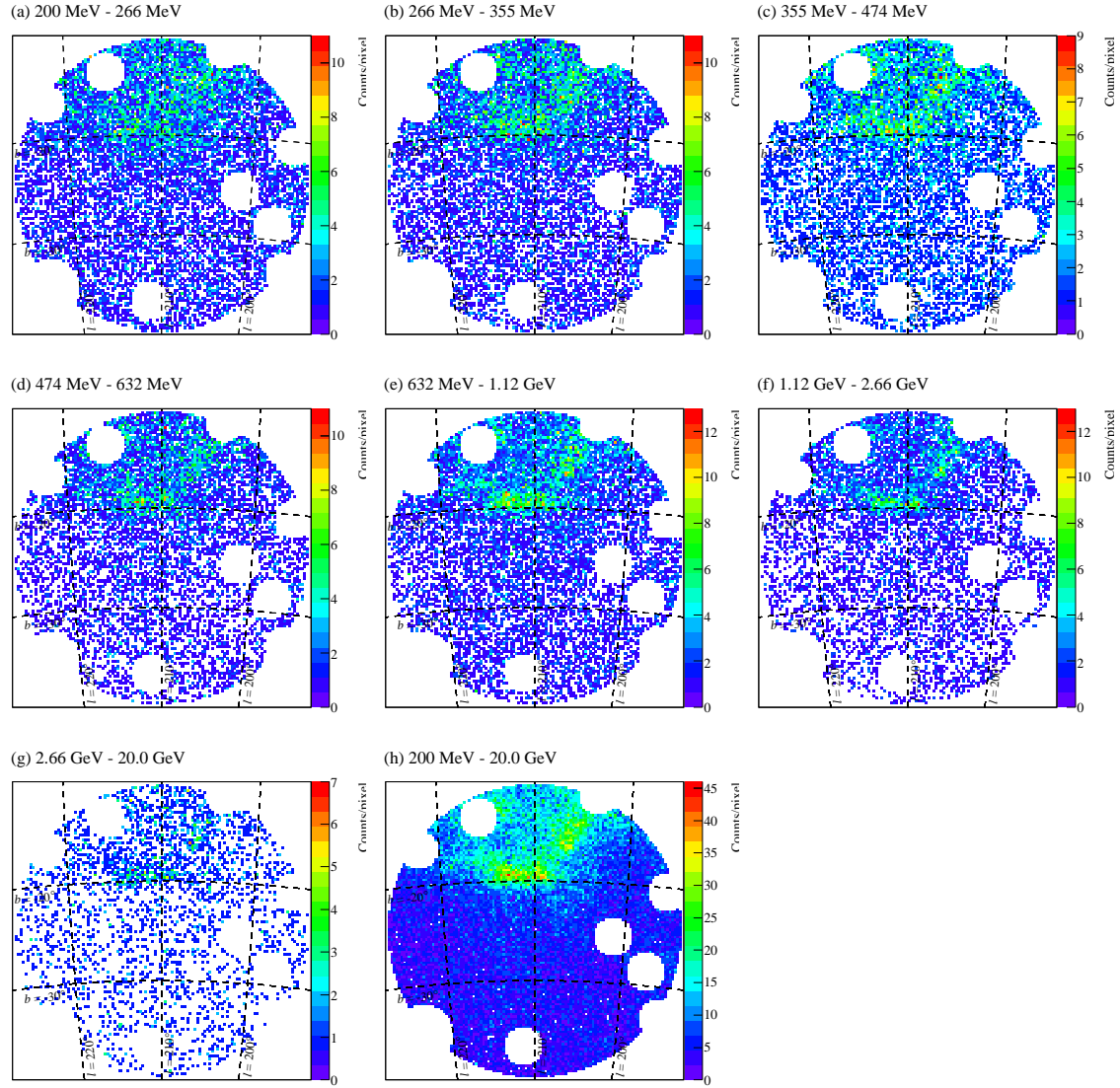


Figure 5.1: Masked count maps of ROI 2. Eight point sources are masked with circles of 2° or 3° radii.
 (a) – (g) Count maps in 7 energy bands. (h) Total count map.

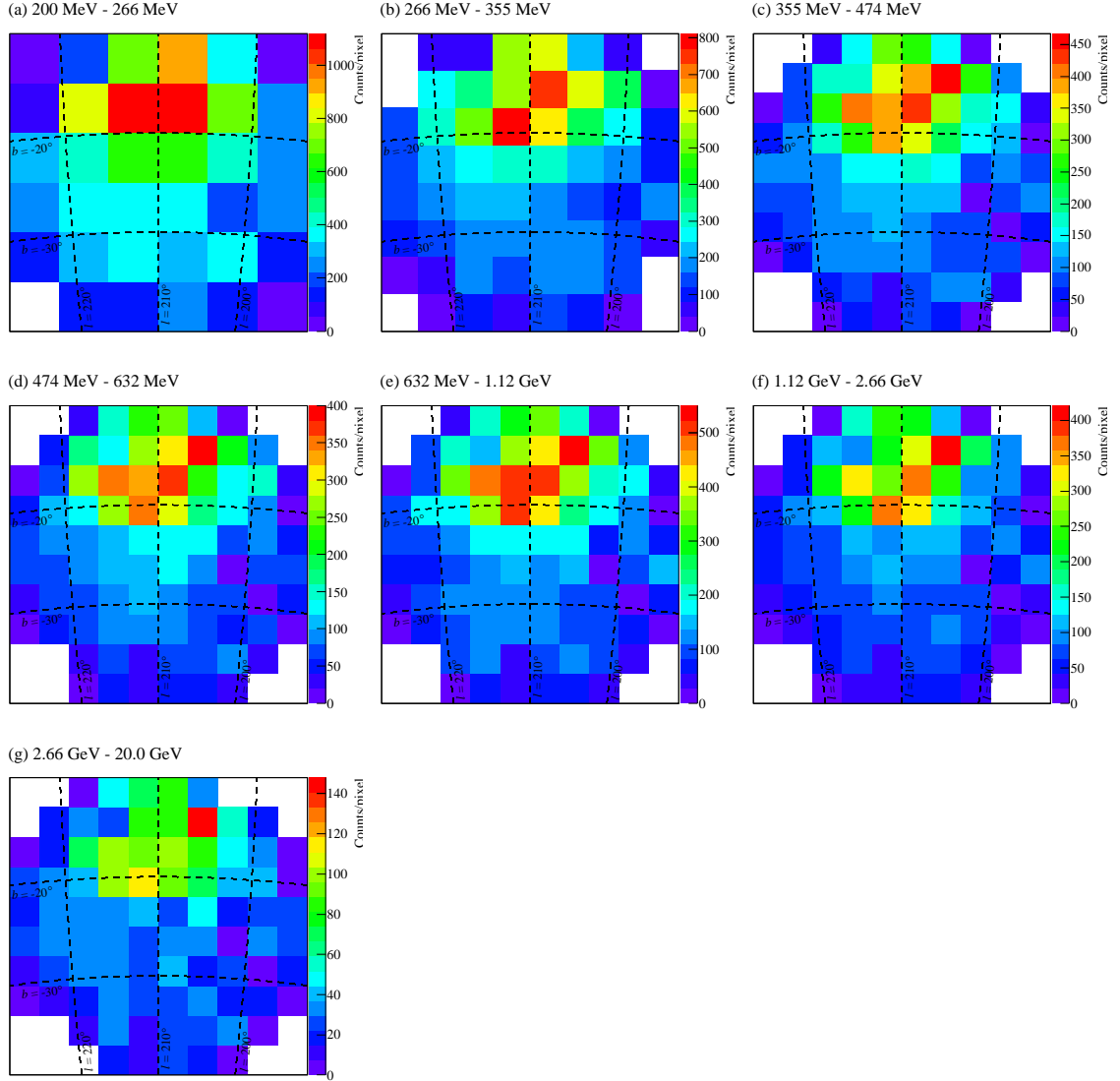


Figure 5.2: Same as Figure 5.1, but rebinned in (a) $5^\circ \times 5^\circ$, (b) $3.75^\circ \times 3.75^\circ$, and (c) – (g) $3^\circ \times 3^\circ$.

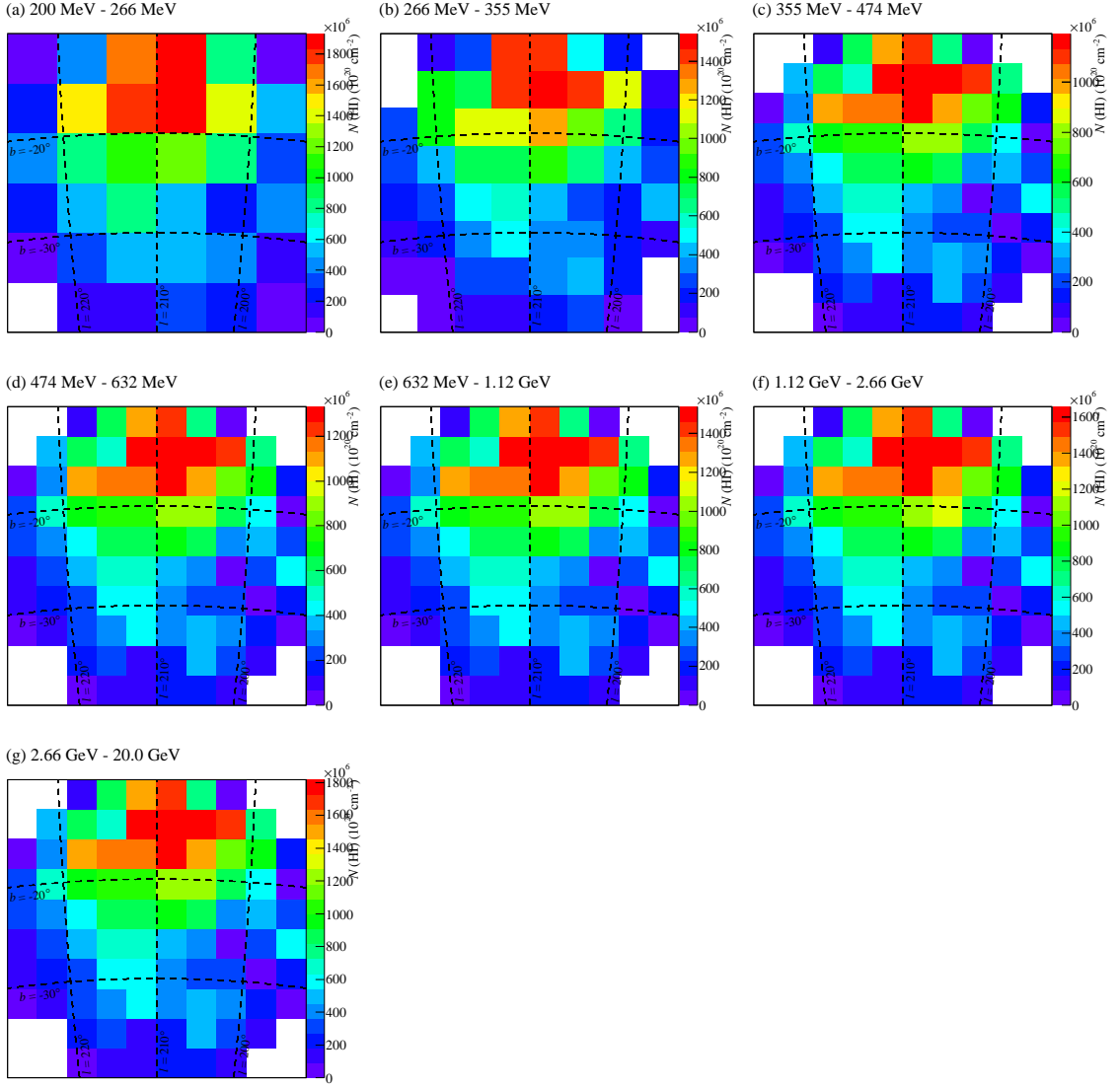


Figure 5.3: The H I maps by Kalberla et al. (2005), rebinned into the 3 pixel sizes used in Figure 5.2. The rebinning is done using the LAT exposure as weights. Note that (c) – (g) are not the same due to energy-dependent exposure.

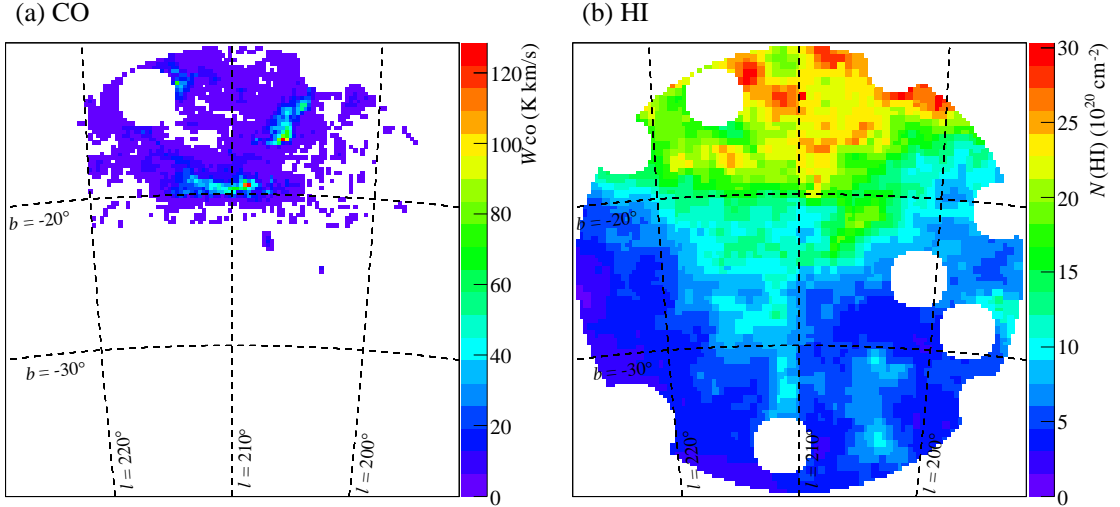


Figure 5.4: Masked maps of W_{CO} (a) and H I (b).

Here $N'(\text{H I})(E, i)$ is the H I column density weighted by the LAT exposure. In each energy band, we determined the two constants, $B(E)$ and $F(E)$, in such a way that the left hand side of equation (5.6), taken from the lower half of Figure 5.1, shows the best pixel-by-pixel agreement to the right hand side of the same equation calculated from Figure 5.2 and the exposure. Figure 5.5 shows the correlation between $N_\gamma(E, i)$ and $B(E) \times N'(\text{H I})(E, i) + F(E) \times \text{Exposure}(E, i)$, using the best-fit values of $B(E)$ and $F(E)$. A linear line $y = x$ corresponds to the best fit function. The correlation in each energy band is obviously linear, and the data points mostly align, within their errors, with this line. In fact, the values of χ^2/ndf are in the range $1.0 \sim 2.0$. This justifies equation (5.6) in the $b < -25^\circ$ region where MCs are absent. The obtained χ^2/ndf of Figure 5.5e is worse than those of other energy bands in which $3^\circ \times 3^\circ$ pixel size is used. This is because the photon statistics is largest among them, and thus contributions from remaining systematic errors, such as weak point sources and the uncertainty of the reconstructed H I column density map, are considered to be appeared. As Figure 5.5 shows, some pixels have small photon counts. However, only several pixels have photon counts of less than 10, and the χ^2 test is expected to work properly (Amsler et al., 2008).

As a result of this analysis, we obtained $B(E)$ and $F(E)$ in all energy bands at the same time. The former can be converted to gamma-ray emissivity ($\equiv dN/dE$) per unit gas density (for $n(\text{H}) = 1 \text{ cm}^{-3}$) per second per energy by dividing it with the width of the energy bins. The latter the isotropic component and IC emission. The observed values of $B(E)$ are tabulated in Table 5.2, and are shown in Figure 5.6 (red crosses) as a function of the gamma-ray energy. We also calculated gamma-ray emissivity spectrum from H I gas, using the up-to-date methods described in Subsection 2.3.1. Specifically, we used the π^0 model of p-p interactions by Kamae et al. (2006), inclusive cross sections for heavier nuclei, the CR metal abundance by Gaisser & Schaefer (1992), and the ISM metal contribution factor 1.02 by Mori (2009). We assumed that the ratio between hydrogen and helium in ISM is 1 : 0.1 in number. The emissivity calculation assumed two different CR fluxes. One is a GALPROP prediction at $(R, Z) = (8.5 \text{ kpc}, 0 \text{ kpc})$, and the other is “demodulated” spectra from the BESS observations (Shikaze et al., 2007), shown in Figure 2.2; their spectral shapes differ below several hundreds MeV. The calculated two π^0 emissivity spectra are shown in Figure 5.6, together with a GALPROP prediction of electron bremsstrahlung spectrum. The observed emissivity is in an excellent agreement with the two models except for the lowest energy bin.

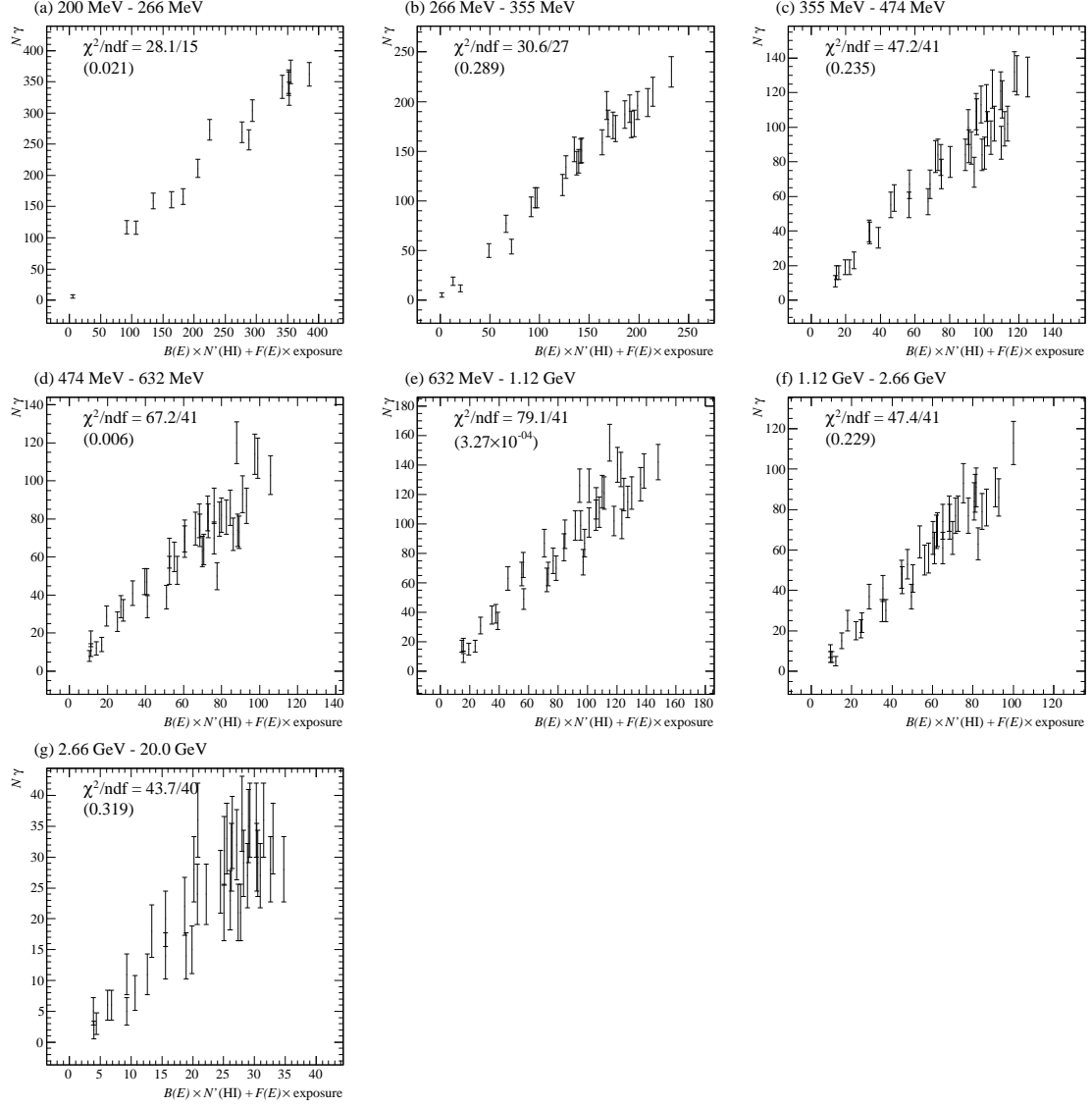


Figure 5.5: Gamma-ray counts in 7 energy bands observed at individual rebinned pixels in the lower half of Figure 5.2, shown against the expected emission from H I gas plus background as defined by equation (5.6) with the best-fit $B(E)$ and $F(E)$. Values in braces are the probabilities of χ^2 fit.

Table 5.2: The observed gamma-ray emissivity of H I gas derived from the coefficient $B(E)$. “Observed” and “Model” correspond to red crosses and black bars in Figure 5.6, respectively.

Energy Range	$dN/dE (\text{s}^{-1}\text{MeV}^{-1})$	
	Observed	Model
200 MeV - 266 MeV	$(2.12 \pm 0.70) \times 10^{-28}$	4.43×10^{-28}
266 MeV - 355 MeV	$(2.44 \pm 0.38) \times 10^{-28}$	2.84×10^{-28}
355 MeV - 474 MeV	$(1.22 \pm 0.21) \times 10^{-28}$	1.66×10^{-28}
474 MeV - 632 MeV	$(9.14 \pm 1.26) \times 10^{-29}$	9.46×10^{-29}
632 MeV - 1.12 GeV	$(3.63 \pm 0.40) \times 10^{-29}$	3.76×10^{-29}
1.12 GeV - 2.66 GeV	$(8.06 \pm 0.97) \times 10^{-30}$	7.25×10^{-30}
2.66 GeV - 20.0 GeV	$(1.55 \pm 0.49) \times 10^{-31}$	2.08×10^{-31}

When the calculated emissivity model is allowed to vary vertically, the data (red cross) come into the best agreement with the predictions (black solid) when the latter are scaled to 0.87 ± 0.05 ($\chi^2/\text{ndf} = 12.2/6$) of their original values. If we ignore the one or two lowest-energy bins so that we can remove the uncertainty in lower energy band, the scale factor becomes 0.92 ± 0.05 ($\chi^2/\text{ndf} = 5.32/5$) or 0.93 ± 0.05 ($\chi^2/\text{ndf} = 5.09/4$), respectively. If we neglect, for the moment, various systematic errors in our data and calculation, the result indicates that the CR fluxes in the Orion region is $\sim 10\%$ lower than that measured at the Earth. This is reasonable, because this region is in the anti-center direction and has a large value of $|b|$. In fact, a GALPROP prediction of the CR flux in the Orion region is 8% lower than that in the solar vicinity.

The derived isotropic background $F(E)$ is shown in Figure 5.7. Its spectral shape is power-law like, and its flux is similar to the EGRET measurements of the isotropic extragalactic emission (Sreekumar et al., 1998). Since it includes the IC contribution, weak point sources, and residual CR background as explained above, it is difficult to precisely model the spectral shape of the isotropic component. However, as the figure illustrates, a single power law ($\Gamma \sim 2$) is expected to work as a first approximation.

5.2.2 X_{CO} and gamma-ray spectrum of H₂

We also estimated the gamma-ray emission from H₂ gas. Using the derived $B(E)$ and $F(E)$, we subtracted the H I emission and the isotropic components, assuming that $B(E)$ and $F(E)$ are the same between the upper and lower halves of ROI 2. The subtracted maps are shown in Figure 5.8 (referred to as “residual maps”). If this subtraction process is accurate, the gamma-ray count in a pixel, $N_{\gamma,\text{res}}(E, i)$, of a residual map is given by

$$N_{\gamma,\text{res}}(E, i) = A(E) \times W_{\text{CO}}'(E, i). \quad (5.7)$$

Here $W_{\text{CO}}'(E, i)$ is the CO intensity weighted by the LAT exposure which is shown in Figure 5.9.

Figure 5.10 shows pixel-by-pixel scatter plots between $N_{\gamma,\text{res}}(E, i)$ given in Figure 5.9 and $W_{\text{CO}}'(E, i)$ in Figure 5.8. By fitting these plots by a linear functions, we have obtained $A(E)$ in each energy band, and further $2X_{\text{CO}}$ [equation (5.4)] by dividing it with $B(E)$ given in Table 5.3. Except for the lowest energy band, the obtained values are similar to the EGRET result in the same region, $(1.35 \pm 0.15) \times 10^{20}$ by Digel et al. (1999). On the other hand, if we assume a constant X_{CO} for all energies, the gamma-ray emissivity from H₂ gas can be derived. Assuming the 92% CR flux, we obtain the best fit X_{CO} as $(1.53 \pm 0.09) \times 10^{20}$. The result is also shown in Figure 5.6 (green crosses). In addition to the emissivity of H I gas, that of H₂ is also in general agreement with the predicted ones. Therefore, the CR spectra inside dense MCs are considered to be not much different from those outside MCs.

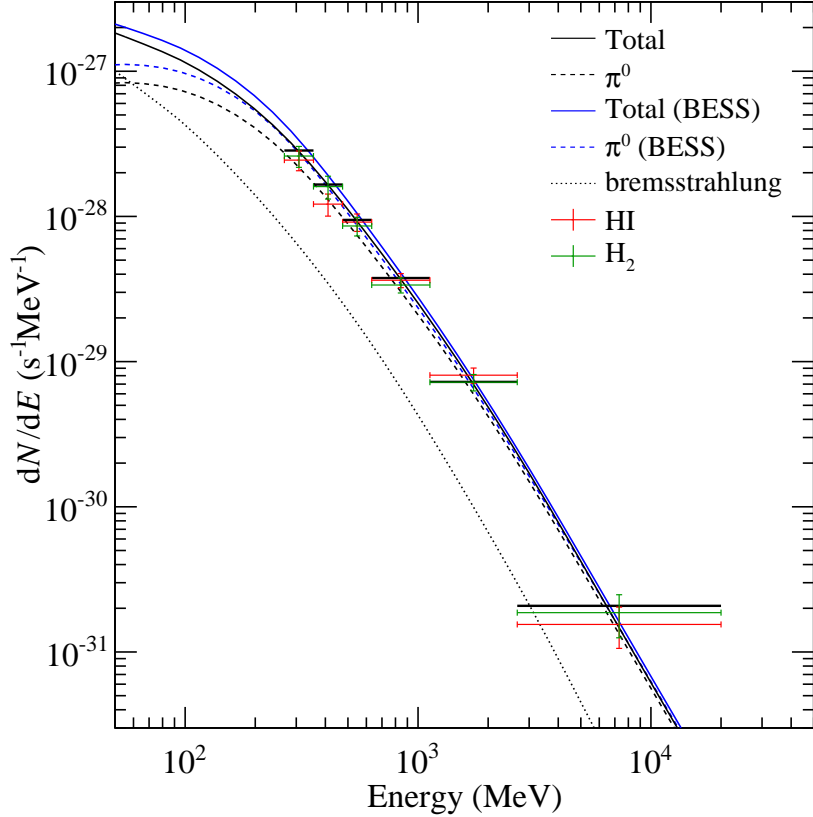


Figure 5.6: The observed gamma-ray emissivity of H I and H₂ gas per unit hydrogen number density (cm⁻³), shown in red and green, respectively. Only statistical errors are shown. The normalization of the H₂ spectrum is adjusted with a constant $X_{\text{CO}} = 1.5 \times 10^{20} \text{ cm}^{-2}(\text{K km s}^{-2})^{-1}$. A black dotted line shows the electron bremsstrahlung emissivity prediction by GALPROP. Black and blue dashed lines show π^0 emission calculated using different CR fluxes, the predicted by GALPROP and the demodulated by Shikaze et al. (2007) (Figure 2.2), respectively. Solid lines show the sum of π^0 and bremsstrahlung components. Black horizontal bars show the average of the black thin line in each energy band, to be compared with the observed data. Unreliable data points of the lowest energy bin are not shown.

Table 5.3: Estimated X_{CO}

Energy Range	$A/2B \equiv X_{\text{CO}}$ ($10^{20} \text{ cm}^{-2}(\text{K km s}^{-2})^{-1}$)	χ^2/ndf
200 MeV - 266 MeV	3.74 ± 0.26	92.1/34
266 MeV - 355 MeV	1.60 ± 0.09	89.4/58
355 MeV - 474 MeV	1.98 ± 0.09	160./86
474 MeV - 632 MeV	1.41 ± 0.07	126./86
632 MeV - 1.12 GeV	1.39 ± 0.06	179./86
1.12 GeV - 2.66 GeV	1.34 ± 0.07	73.6/86
2.66 GeV - 20.0 GeV	1.81 ± 0.16	158./86

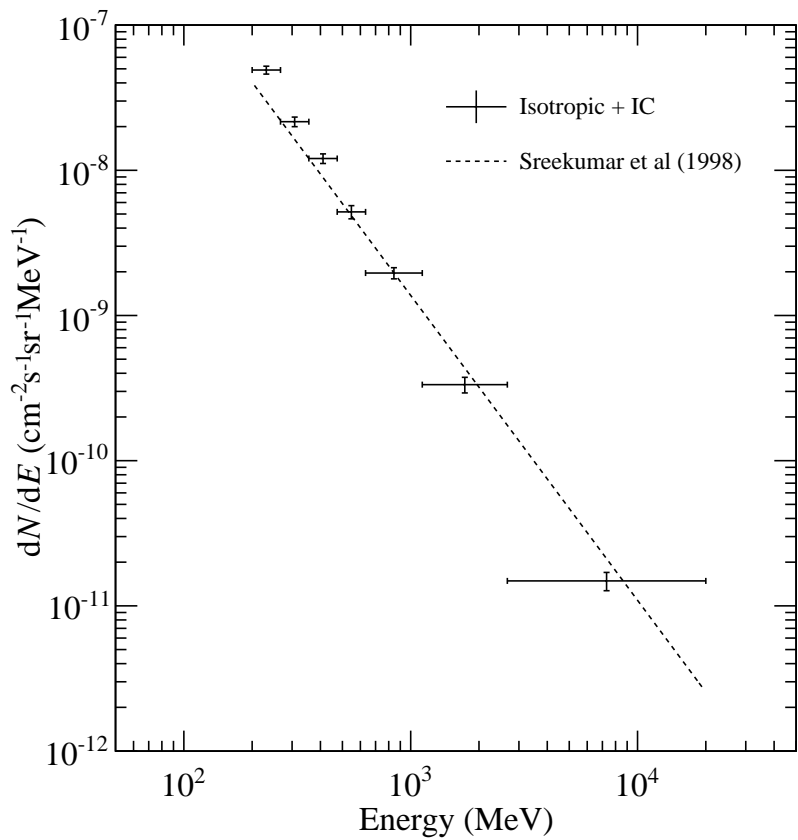


Figure 5.7: The obtained isotropic component $F(E)$. A dashed line show the isotropic extragalactic emission measured with the EGRET (Sreekumar et al., 1998).

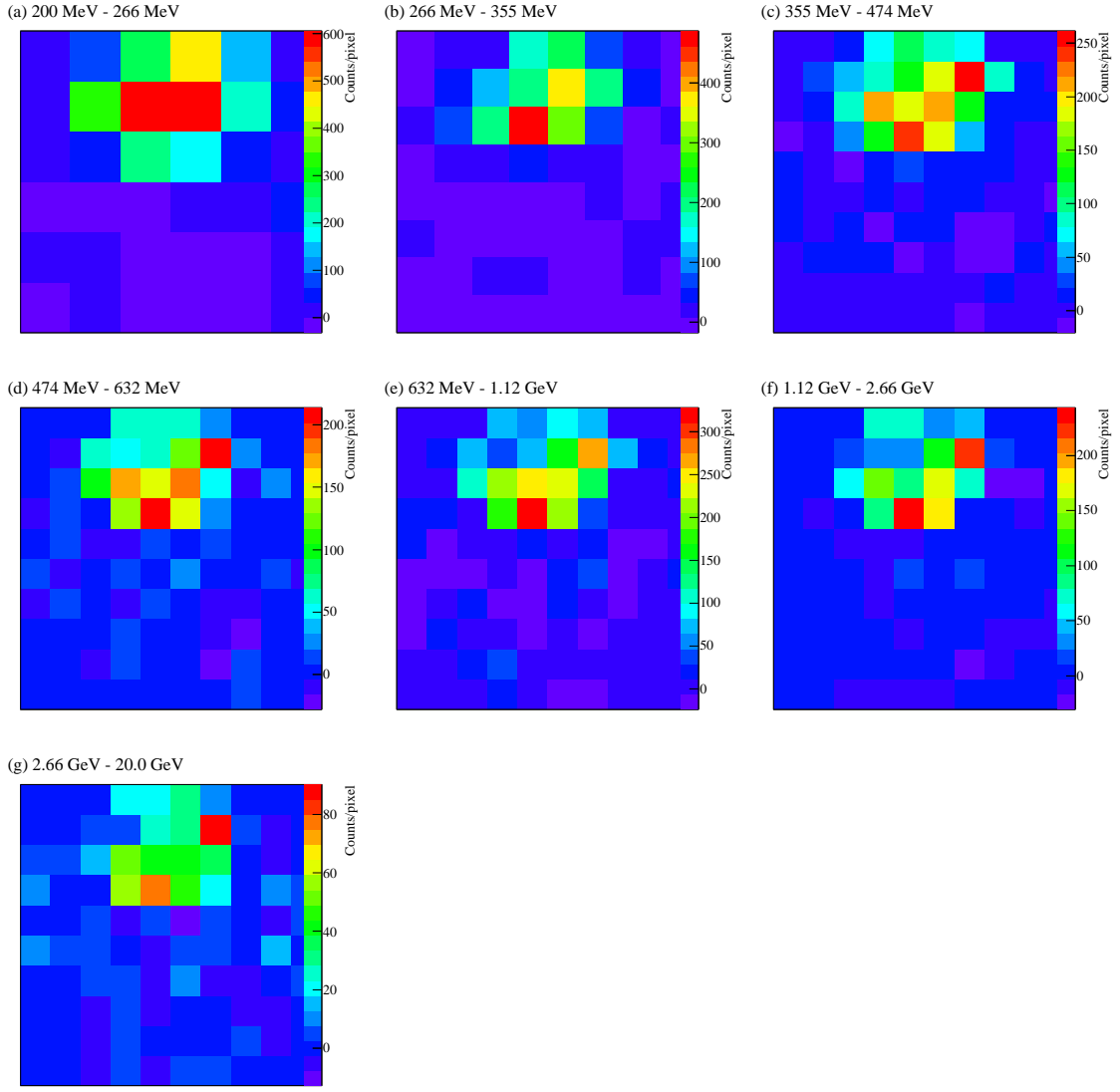


Figure 5.8: “Residual maps” of gamma-ray emission, obtained by subtracting from Figure 5.2 the H I gas emission and the isotropic background, $B(E) \times N'(\text{H I})(E, i) + F(E) \times \text{Exposure}(E, i)$. Negative pixels are due to statistical fluctuations.

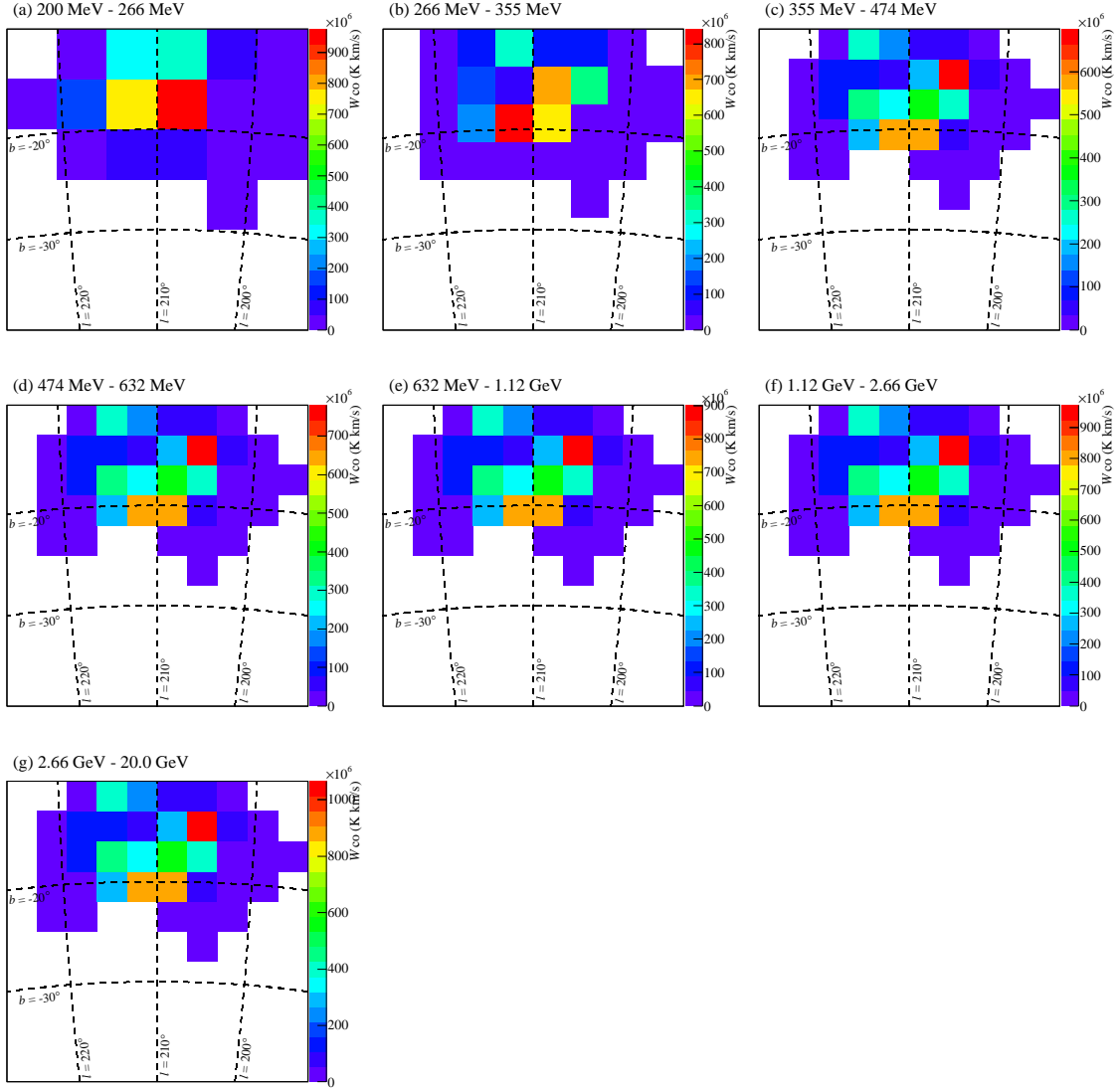


Figure 5.9: The W_{CO} maps by Dame et al. (2001), after rebinning and exposure correction was applied as in Figure 5.3.

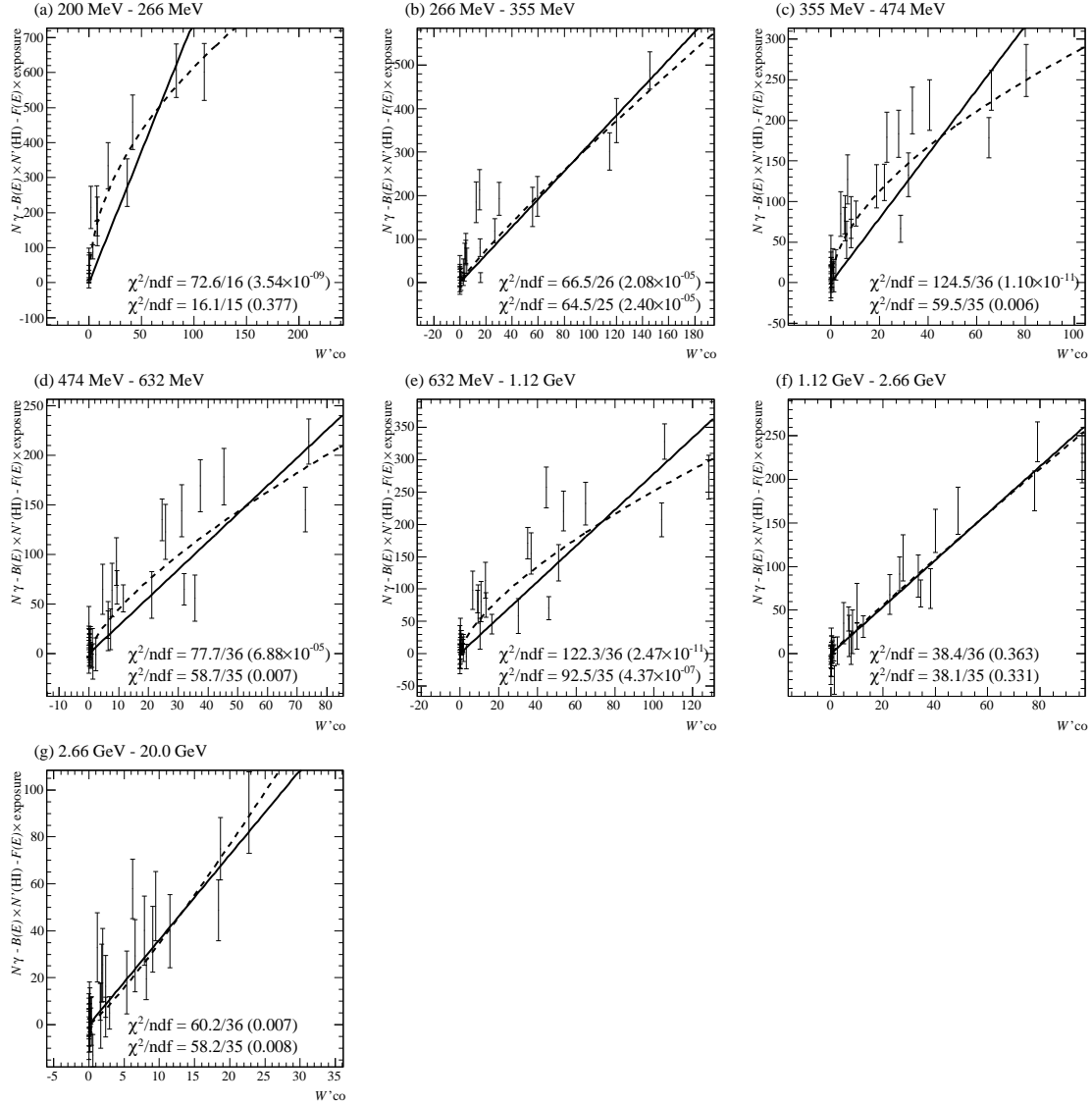


Figure 5.10: The observed gamma-ray count with H I and isotropic components subtracted, plotted against W_{CO} which is weighted by the exposure. The slope of a fitting line is equivalent to $2X_{\text{CO}}/10^{20}$.

On a closer inspection of Figure 5.10, we find the correlation to be much worse than the case of H I emission (Figure 5.5), and the obtained reduced χ^2 rejects a simple linear function in most of energy bands. There are several possible scenarios to explain this deviations. First, the effect of PSF may not be negligible when analyzing molecular clouds because their structure is smaller than that of H I gas and the rebinned pixel sizes. For example, the most of Orion A is contained in only two pixels in Figure 5.9a, while the cloud is actually smeared out as seen in Figure 5.8a. As we can see in Figure 5.6, the emissivity of H I gas is lower than the predicted ones at the lowest energy point. Smeared out low-energy photons may be counted as a part of $F(E)$. In order to study the emission from MCs properly, we need to take the effect of PSF into account. These problems will be removed in the next sections by using a likelihood method and considering the PSF. Second, the method of subtracting the H I contribution may be subject to large systematic errors, because we derived $B(E)$ and $F(E)$ in only the lower region of ROI 2.

Yet another possibility explaining the scatter in Figure 5.10 is that our basic assumption of a constant X_{CO} and a constant CR distribution may not be correct. In Figures 5.8c to 5.8g, we can see two brightest red pixels of which one (upper right) corresponds to the core of Orion B, and the other to the middle of Orion A. However, the latter pixel is less bright in Figure 5.9. As suggested by this comparison, as well as by Figure 5.10, the gamma-ray brightness may depend non-linearly on the CO brightnesses. One possible cause of such a non-linearity would be that the CO lines become optically thick at the sense cores of MCs. This effect would make the correlation in Figure 5.10 more concave than a straight line. However, Figure 5.10 suggests rather convex correlations, in such a way that the gamma-ray intensity becomes saturated at the MC cores.

In order to examine the gamma-ray vs. CO correlation for possible non-linearity, we fitted the data in Figure 5.10 with a non-linear function given by $y = p_1 x^{p_2}$. The best fit functions are shown with dashed lines. In 4 of the 7 energy bands, the best fit functions became convex, and the fit χ^2 's were improved. Therefore, the gamma-ray surface brightness tends to saturate as the CO intensity increases. If CRs are reflected by the strong magnetic fields inside MC cores, the CR density and gamma-ray production rate will be smaller than expected. Alternatively, if the formation of CO is still in progress in thin outskirts of MCs or the variation of gas temperature changes the excitation rate of CO molecules, gamma-ray emission will be stronger than expected. These alternatives are examined in Sections 5.4 and 5.5.

5.2.3 Summary of the simple analysis

We obtained several important results from the above analysis which is simple but robust.

1. The derived gamma-ray spectrum of H I gas is consistent with the recent π^0 model (Kamae et al., 2006), H I observations (Kalberla et al., 2005), and CR observations (e.g. Shikaze et al., 2007). The “GeV excess” reported by the EGRET observations (Hunter et al., 1997) was not confirmed. The implied CR flux in the Orion region is $\sim 90\%$ of that in the solar neighborhood.
2. Gamma-ray emission from H₂ gas is also explained approximately by the predicted π^0 gamma-ray emissivity. Thus, using our π^0 model calculation, we are able to study the cloud structure and the distribution of CRs.
3. We obtained a rough estimation of X_{CO} of the Orion clouds as $\sim 1.5 \times 10^{20} \text{ cm}^{-2} (\text{K km s}^{-1})^{-1}$. It is consistent with the EGRET observations, $(1.35 \pm 0.15) \times 10^{20}$, and that obtained by Dame et al. (2001), $(1.8 \pm 0.3) \times 10^{20}$, from comparison between W_{CO} , $N(\text{H I})$, and dust observations (Schlegel et al., 1998).
4. However, the relation between the gamma-ray intensity and the CO line brightness is not explained by a linear function as shown in Figure 5.10. It implies that our basic assumption of a constant X_{CO} and CR density is not appropriate.

Although these results are already novel enough, we did not take the LAT PSF into account in this analysis, and the detailed structure of the Orion clouds was ignored. We perform additional analyses in the next sections considering the LAT PSF, and further investigate the item 4.

5.3 Emission Models

In this and the following sections, we use gamma-ray emission models to analyze the LAT images. In Section 5.4, we extract the gamma rays associated only with the Orion MCs. In order to subtract other emissions, we use their emission models with finite uncertainties. In Section 5.5, we perform maximum likelihood analyses to validate the H I emission model and make the residual between the observed gamma-ray intensity and the CO map clear. The maximum likelihood analysis is a kind of fitting method and requires knowledge of the instrumental responses and detailed emission models. We start from quantitatively modeling the gamma-ray emission components listed in Table 5.1. Here we assume a constant X_{CO} and a constant CR distribution on a small scale of ~ 100 pc, i.e., across the Orion clouds. To model the components ⑧ and ⑨, we produced a three-dimensional density map of H I gas using the LAB survey (Kalberla et al., 2005) with a constant spin temperature of 125 K (Dickey & Lockman, 1990). A CO survey by Dame et al. (2001) was used in the modeling of molecular clouds. These maps of the Orion region are shown in Figure 2.12. Along our lines of sight through the Orion clouds, the more extended H I gas and the more concentrated molecular clouds have comparable contributions to the gamma-ray emission, as clearly judged from Figures 5.5 and 5.10. The two gas maps are “collided” with a three-dimensional CR distribution map predicted by GALPROP. This gives a prediction for gamma-ray emission from H I gas and H₂ gas, as a function of galactic coordinates (l, b) and gamma-ray energy E . The interstellar radiation fields (cosmic microwave background and infrared background) modeled by Porter et al. (2008) is used to predict the IC emission component which is relatively small compared to the emission from the gases, and is hard to be distinguished from the isotropic component.

These “predicted” emission models are based on many experimental and theoretical knowledge we have. Thus, it is inevitably subject to various statistical and systematic errors arising from measurement uncertainties, assumptions, and ignored minor processes. For example, typical statistical and systematic errors of the CR measurements are $\sim 10\%$ (e.g. Haino et al., 2004; Abdo et al., 2009d). The 21 cm and CO-line measurements with radio telescopes have comparable errors. Thus, the normalization of the gamma-ray emission model becomes uncertain to the same degree. Even if they were small enough, the spectral shape of CRs outside the vicinity of the Earth (local interstellar spectrum) is unknown due to the solar modulation as explained in Subsection 2.1.2. Different assumptions of CR spectra below 1 GeV predict different π^0 spectra as shown in Figure 5.6. In addition to these uncertainties, we found that contributions from CR and ISM metals were underestimated in the source code of GALPROP. It also uses an old normalizations for p-He, α -H, α -He cross sections by Dermer (1986), while the up-to-date model by Kamae et al. (2006) is used in it to calculate the inclusive cross section of π^0 . We estimated relative contributions of π^0 emission should be 20% higher than the GALPROP calculation¹. As a result, we need to carefully examine the predicted emission models and readjust their normalizations using our real data of gamma-ray observations. The spectral shape of π^0 emission has been already validated in Section 5.2.

Several emission models have been calculated using GALPROP in the LAT collaboration or by the present author. Five of them are listed in Table 5.4. Each emission model and its parameter file are labeled with a unique number dubbed “GALDEF” (GALprop DEFinition). The model “54_5gXvarh7S” is called “a priori” model, which is, literally, not tuned to “reproduce” the LAT observations. This model was compared with the LAT observations by Abdo et al. (2009a) at intermediate Galactic latitudes ($10^\circ \leq |b| \leq 20^\circ$), and was found to fall $\sim 10\text{--}15\%$ short of the observed gamma-ray spectrum.

¹The factor 0.20 is taken into account in Figure 5.6.

Table 5.4: Parameters for different GALPROP models.

GALDEF	Normalization [†]		e^- index	T_s (K)	Comment
	p	e^-			
54_5gXvarh7S	5.00	0.40	2.54	125	“a priori” model (not used in the present thesis)
54_77Xvarh7S	5.75	0.56	2.42	125	Up-to-date model
54_78Xvarh7O	5.00	0.56	2.42	125	Same as 54_77Xvarh7S, but the proton flux is not adjusted
54_78Xvarh7O_Ts100	5.00	0.56	2.42	100	Same as 54_78Xvarh7O, but the spin temperature of H I gas is assumed to be 100 K
54_78Xvarh7O_Ts100000	5.00	0.56	2.42	100000	Same as 54_78Xvarh7O, but the spin temperature of H I gas is assumed to be 100000 K

[†]Proton and electron fluxes ($10^{-9} \text{ cm}^{-2} \text{ sr}^{-1} \text{ s}^{-1} \text{ MeV}^{-1}$) are normalized at energies of 100 GeV and 34.5 GeV, respectively.

“54_77Xvarh7S” is the most up-to-date (as of June 2009) model in the collaboration. The injection parameters of CR protons and electrons are adjusted to reproduce the LAT observations in high-latitude regions ($|b| \geq 10^\circ$). The spectral index of the injected CR electrons² is also adjusted to the value observed by the LAT (Abdo et al., 2009d). “54_78Xvarh7O” is the same as “54_77Xvarh7S”, but the normalization of proton flux is reverted to that of “54_5gXvarh7S”. In order to see the effect from optical depth correction (see equation (2.4)), we also prepared similar two models in which T_s is changed to 100 K or 100000 K. The latter is an extremely optically thin case. In all models, X_{CO} is assumed to depend on distance from the Galactic center (Strong et al., 2004b) due to the gradient of metallicity, and is approximated by a step function given by

$$X_{\text{CO}} = \begin{cases} 0.4 \times 10^{20} & (R \leq 3.5 \text{kpc}) \\ 0.6 \times 10^{20} & (3.5 \text{kpc} < R \leq 5.5 \text{kpc}) \\ 0.8 \times 10^{20} & (5.5 \text{kpc} < R \leq 7.5 \text{kpc}) \\ 1.5 \times 10^{20} & (7.5 \text{kpc} < R \leq 9.5 \text{kpc}) \\ 10 \times 10^{20} & (9.5 \text{kpc} < R). \end{cases} \text{ cm}^{-2} (\text{K km s}^{-2})^{-1} \quad (5.8)$$

Therefore, in the GALPROP calculation, X_{CO} at the Orion clouds is $1.5 \times 10^{20} \text{ cm}^{-2} (\text{K km s}^{-2})^{-1}$. This is a reasonable approximation compared to our simple analysis (Table 5.3).

5.4 Analyses of the Orion Clouds

Following the preliminary analysis made in Subsection 5.2.2, we study the further details, the gamma-ray emission from the Orion MCs, in an attempt to obtain information on the MCs as well as the CR properties therein. After subtracting MC-unrelated gamma-ray components (Subsection 5.4.1), the spectra of Orion A and Orion B are derived separately, together with their mass estimation (Subsection 5.4.2). Then, utilizing the LAT angular response, we compare the gamma-ray surface brightness with the spatial distributions of the CO line (Subsection 5.4.3) and dust extinction (Subsection 5.4.4).

²This value changes to ~ 3 after propagation processes.

5.4.1 Extraction of the Clouds

In order to extract the emission associated with the Orion clouds, we must model and remove the H I, IC and the isotropic components. For this purpose, we simulated gamma-ray count cubes of the H I and IC components using GALPROP, taking into account the LAT PSF and incident gamma-ray angles. These count cubes have infinite photon statistic. The simulation results are binned in 120×120 pixels of $0.25^\circ \times 0.25^\circ$ in Galactic coordinates, and in a logarithmic series of 16 energy bins between 200 MeV and 20 GeV. We divided them by an exposure cube of the same three-dimensional bins to obtain intensity cubes convolved with the LAT PSF. Energy-integrated maps of the IC and H I components, obtained by projecting the GALPROP results into the sky plane, are shown in Figures 5.11a and 5.11b, respectively. The former is almost flat and fainter compared to the latter. Since the figures are already convolved with the PSF, the small structure found in Figure 2.12d are smeared out.

We then subtracted the IC and H I intensity cubes, from the observed total count cube corrected for the exposure cube. Energy-integrated intensity maps, before and after of this subtraction, are shown in Figures 5.11d and 5.11e, respectively. Thus, at this stage, Figure 5.11e includes emissions from H₂ gas, the isotropic components, and point sources, assuming that the subtraction process is accurate enough. We finally subtracted the isotropic component from Figure 5.11e. Since no first-principle calculation is applicable to the isotropic component (including the instrumental background), we determined it from the residual emission in “background regions” which are defined with dashed lines in Figure 5.15a. These regions do not include significant point sources, and are more than 3° away from the surrounding point sources and the Orion clouds. The obtained intensity of the isotropic component and the extracted final intensity maps are shown in Figures 5.11c and 5.11f, respectively. The same analysis in the energies above 1 GeV gave results shown in Figure 5.12.

The accuracy of determining the normalization of π^0 and bremsstrahlung emissions from H I gas is estimated to be 10% and 20%, respectively. We discuss their normalizations in Section 5.5 later. To study the effect from these uncertainties, we repeated the same extraction process with different normalizations; 1.17, 1.17×1.1 , and 1.17×0.9 for H I π^0 emission, while 1.2, 1.5, and 1.8 for bremsstrahlung.

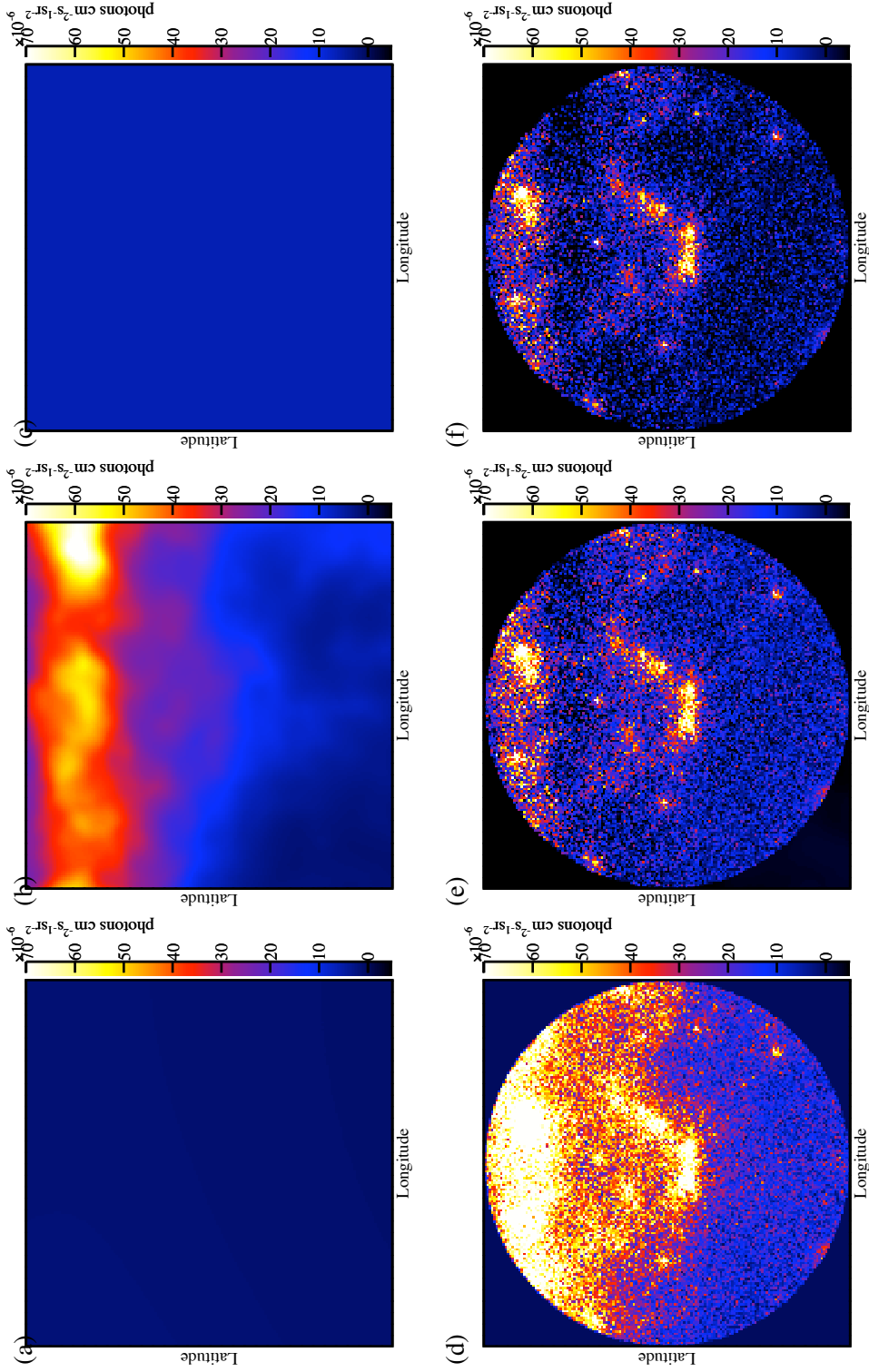


Figure 5.11: Observed and modeled gamma-ray intensity maps above 200 MeV. (a) A modeled intensity map of IC emission. (b) A modeled intensity map of H I ($\pi^0 + \text{bremsstrahlung}$). (c) An intensity map. (d) The observed intensity map. (e) An intensity map after subtracting the IC and H I components. (f) An intensity map after further subtracting the isotropic component from (e). All figures are corrected for exposure.

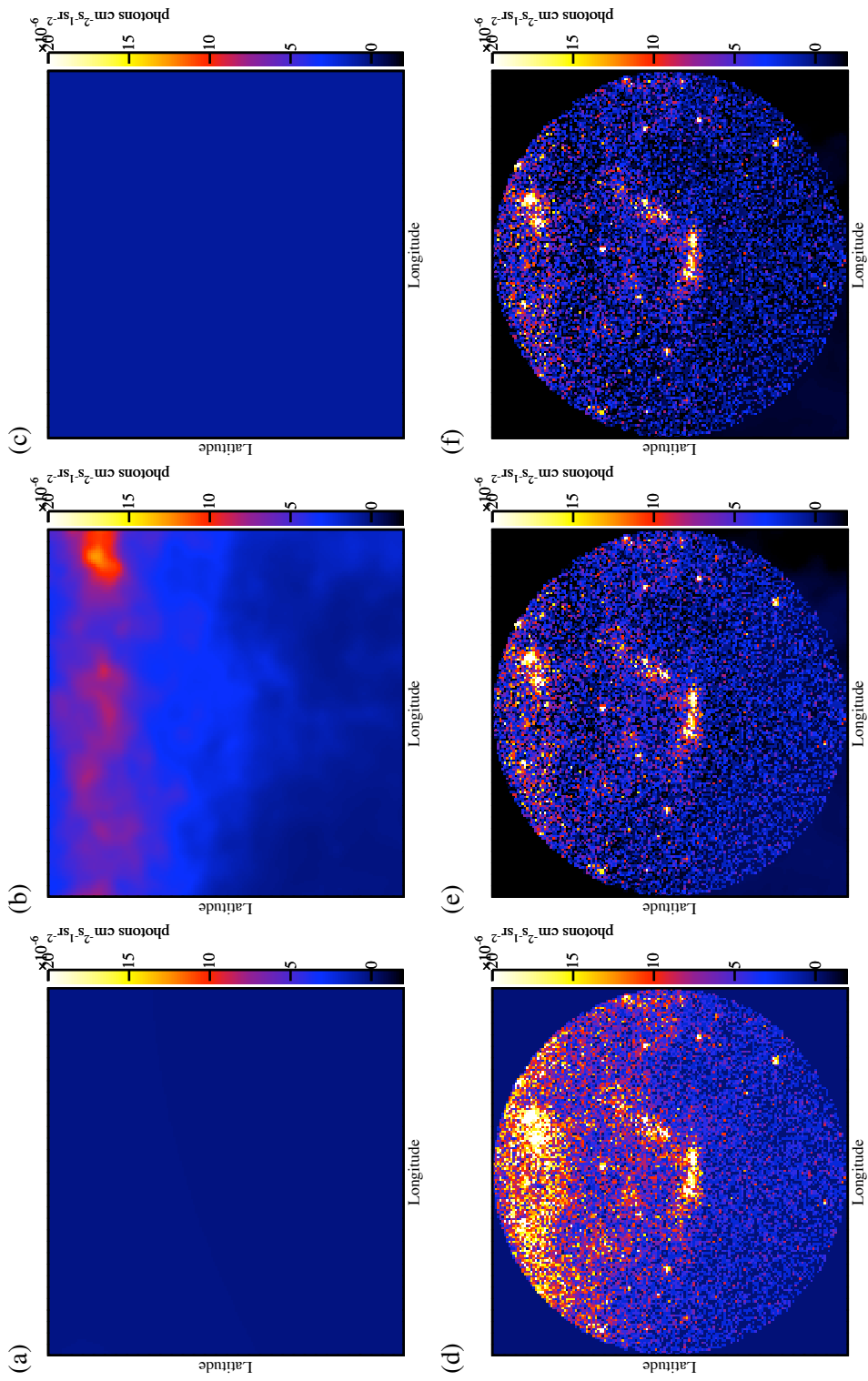


Figure 5.12: Same as Figure 5.11, but in energies above 1 GeV.

5.4.2 The Energy Spectra and Total Masses of the Orion A and B Clouds

In this section, we analyze the energy spectra of the Orion A and B clouds for two purposes. One is to confirm if the spectral shapes can be explained by the π^0 model with finer bin sizes than those used in Section 5.2. The other is to calculate the total masses of the clouds³. So far, their masses have been calculated using an empirical X_{CO} and a CO map, but the possible nonuniformity of X_{CO} may affect these estimates. If their spectra are consistent with the π^0 model, we are able to calculate their masses assuming CR spectra and a distance to the clouds.

The Galactic positions of the two clouds are estimated to be $(R, Z) \sim (8.8 \text{ kpc}, -0.14 \text{ kpc})$ if we assume the Solar position to be $(R, Z) = (8.5, 0)$ (Kerr & Lynden-Bell, 1986), and the distance to the clouds to be 400 pc. The distance was chosen according to recent precise parallax observations of the Orion nebula (Menten et al., 2007; Sandstrom et al., 2007; Hirota et al., 2007; Kim et al., 2008) (see Table 2.4). The CR flux is considered to be decreased as R or Z increase. In fact, we have determined the CR normalization factor of the region to be $0.87 \pm 0.05 - 0.93 \pm 0.05$ in Section 5.2. Furthermore, a GALPROP simulation, performed for the Orion cloud location, predicts CR normalization of 92% relative to that at the Solar position as shown in Figure 5.13. We thus adopt 0.92 to be a typical normalization factor in the region, and calculate the π^0 gamma-ray emissivity using it.

We integrated all the photons inside the region of Orion A and B, of which the boundaries are defined in Figure 5.15a. Figure 5.14 shows the derived energy spectra of the clouds. We fitted them with the π^0 and bremsstrahlung components, of which the normalizations were both set free. The obtained reduced χ^2 are 16.7/14 for Orion A and 14.7/14 for Orion B. Thus the gamma-ray emission mechanism of the Orion clouds are consistent with our π^0 model. The results derived here are essentially the same as given in Figure 5.6, except that the two clouds have been separated, and that the IC and isotropic components are derived in the different way.

Since the normalization of our π^0 emission model is directly proportional to the target baryonic mass, the fitting results in Figure 5.14 can be readily converted into the cloud mass. The calculation yields

$$M_A = (78.1 \pm 8.4_{\text{(stat)}} \pm 4.9_{(\pi^0)} \pm 0.4_{\text{(Brems)}}) \times 10^3 M_{400} \quad (5.9)$$

$$M_B = (38.4 \pm 5.8_{\text{(stat)}} \pm 2.9_{(\pi^0)} \pm 0.2_{\text{(Brems)}}) \times 10^3 M_{400}, \quad (5.10)$$

where M_{400} is defined as

$$M_{400} \equiv \left(\frac{d}{400 \text{ pc}} \right)^2 M_\odot. \quad (5.11)$$

Here the first error terms show the statistical errors in the fitting, the second ones are systematic uncertainties in determining the normalization of π^0 emission of H I gas, and the third ones are those of bremsstrahlung emission.

The best-fit masses of the clouds increase (decrease) by about 10% when we decrease (increase) the normalization of the H I π^0 component. This is because the mass column densities of H I and H₂ gases toward the clouds are comparable. As shown in Table 5.5, the uncertainty of the normalization of the bremsstrahlung component does not affect the best-fit masses, although it changes the spectral shape below several 100 MeV. The shaded ribbons show the typical systematic error of the LAT itself. It is estimated to be 5% at 500 MeV, and 10% at 100 MeV and 10 GeV.

5.4.3 Correlation with CO

In Subsection 5.2.2 and Figure 5.10, we found an indication that the gamma-ray surface brightness of the Orion MCs may not necessarily correlate tightly with the CO intensity distribution. However, this could be an artifact of the finite PSF. Therefore, let us compare the extracted gamma-ray intensity map (Figures 5.11f and 5.12f) more closely with the CO distribution. For this purpose, we simulated a 200 MeV

³“Mass” includes all components of which their density is not proportional to the 21 cm line emission; H₂, He, and metals.

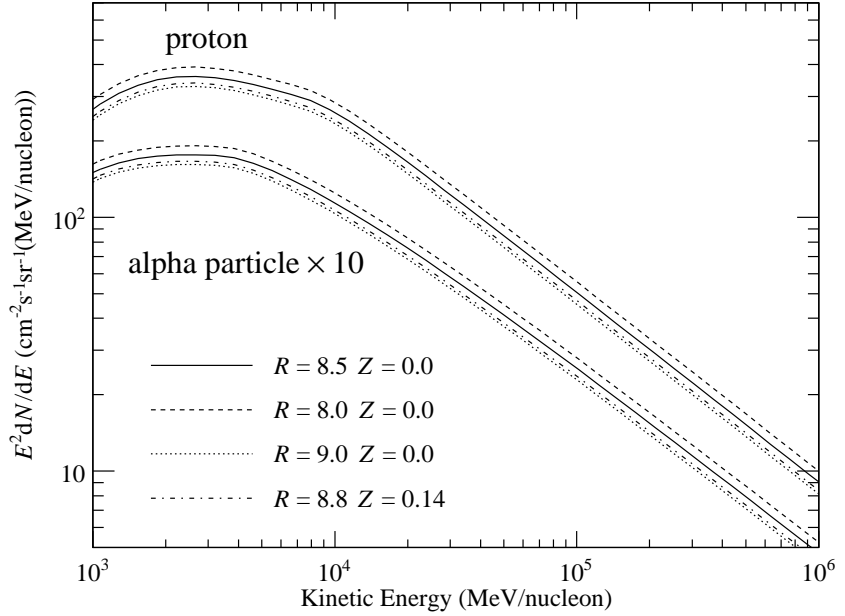


Figure 5.13: CR proton and alpha-particle spectra ($\times 10$) predicted by GALPROP model for selected Galactic locations. (solid) $R = 8.5$ kpc, $Z = 0$ kpc, (dashed) $R = 8.0$ kpc, $Z = 0$ kpc, (dotted) $R = 9.0$ kpc, $Z = 0$ kpc, (dot-dashed) the Orion region $R = 8.8$ kpc, $Z = \pm 0.14$ kpc. R is the radius from the Galactic center and Z the distance from the Galactic plane.

Table 5.5: The masses of the Orion clouds in unit of M_{400} . Statistical errors are shown.

π^0	H I Normalization	Orion A (M_{400})	Orion B (M_{400})
	Bremsstrahlung		
1.17×0.9	1.5	83.0 ± 8.4	41.3 ± 5.8
1.17×1.0	1.5	78.1 ± 8.4	38.4 ± 5.8
1.17×1.1	1.5	73.2 ± 8.4	35.4 ± 5.8
1.17×1.0	1.2	78.5 ± 8.4	38.6 ± 5.8
1.17×1.0	1.8	77.8 ± 8.4	38.2 ± 5.8

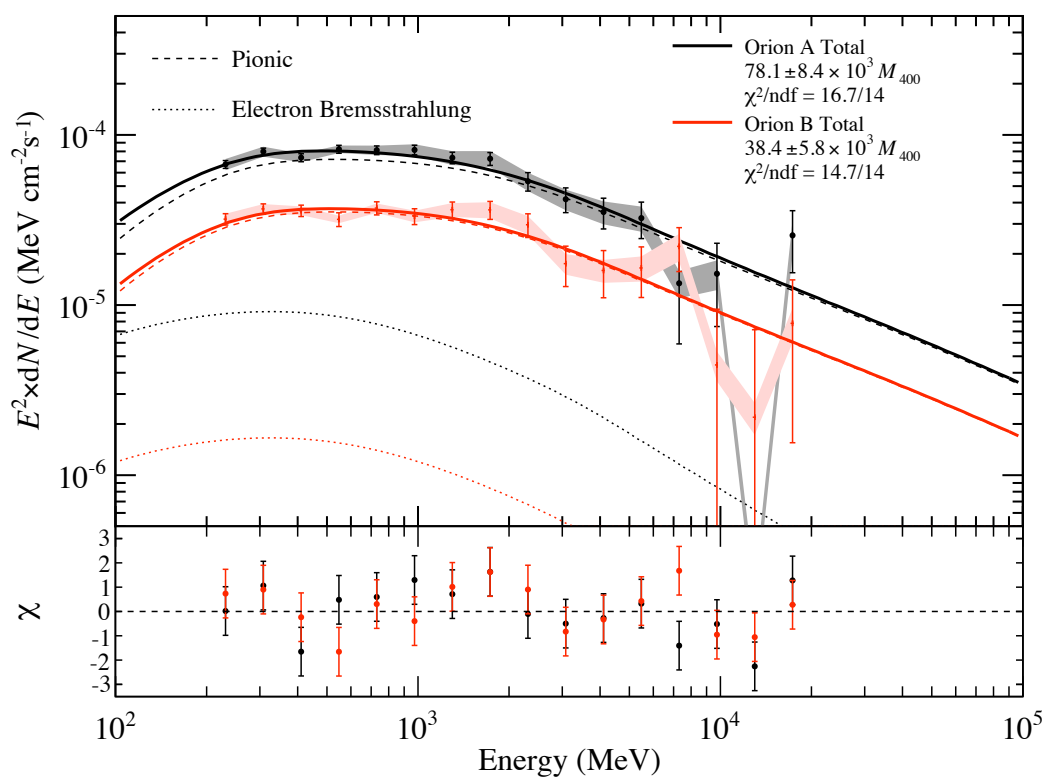


Figure 5.14: Gamma-ray spectra of the Orion clouds in the $\nu F \nu$ presentations. Shaded ribbons show the LAT systematic errors.

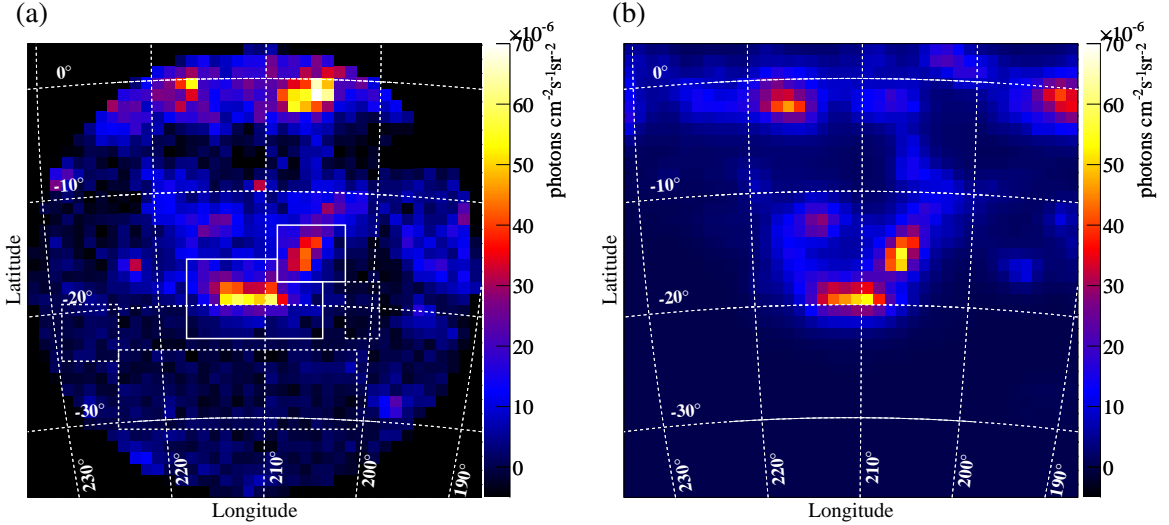


Figure 5.15: Comparison of the observed and simulated gamma-ray maps in energies between 200 MeV and 20 GeV. (a) Same as Figure 5.11f, but rebinned into $1^\circ \times 1^\circ$ pixels. Solid lines illustrate the boundary definition of the Orion A and B clouds. Rectangles of dashed lines show the background regions. (b) A simulated gamma-ray map from the CO map assuming a constant X_{CO} of $1.5 \times 10^{20} \text{ cm}^{-2}(\text{K km s}^{-2})^{-1}$.

~ 20 GeV gamma-ray intensity map that is expected if the gamma-ray intensity is exactly proportional to the CO intensity, by using the W_{CO} map, a constant X_{CO} of $1.5 \times 10^{20} \text{ cm}^{-2}(\text{K km s}^{-2})^{-1}$, and a constant CR flux. Figures 5.15a and 5.15b show the observed intensity map and the simulated one, respectively. The latter is convolved with the LAT PSF. We rebinned these maps in $1^\circ \times 1^\circ$ pixels to reduce the statistical fluctuations of the observed map. The boundaries of the two clouds are defined with solid lines in Figure 5.15a.

We correlated these maps pixel by pixel, and created scatter plots as shown in Figure 5.16. Unlike in Section 5.2, the horizontal axis hereafter represents the observed gamma-ray counts (after removing the MC-unrelated components), while the vertical axis gives gamma-ray counts predicted by the W_{CO} distribution if X_{CO} takes a constant value at $1.5 \times 10^{20} \text{ cm}^{-2}(\text{K km s}^{-2})^{-1}$. Thus, we reconfirm the several effects noticed in Subsection 5.2.2 in reference to Figure 5.10 (i.e., deviations from simple proportionality). In addition, the scatter plot appears to differ between the two clouds, and even within the Orion A. The pixels of the Orion A cloud are subdivided into two regions, $l > 212^\circ$ and $212^\circ > l$ (hereafter as Orion A₊ and A₋ regions, respectively).

As shown in Figure 5.16 by straight lines, we fitted the data points with a linear function as

$$y = p_0 + p_1 I_{\gamma, > 200 \text{ MeV}} \quad (5.12)$$

where $I_{\gamma, > 200 \text{ MeV}}$ and y are the observed and predicted gamma-ray counts, respectively. When the effects of changing the H I-component intensity by $\pm 10\%$ for π^0 and $\pm 20\%$ for bremsstrahlung as a systematic errors, the fitting results are summarized as

$$\begin{aligned} p_{1,A} &= 0.87 \pm 0.02_{\text{(stat)}} \pm 0.12_{\text{(\pi}^0\text{)}} \pm 0.01_{\text{(Brems)}} \\ p_{1,A_+} &= 0.71 \pm 0.03_{\text{(stat)}} \pm 0.06_{\text{(\pi}^0\text{)}} \pm 0.00_{\text{(Brems)}} \\ p_{1,A_-} &= 0.95 \pm 0.03_{\text{(stat)}} \pm 0.08_{\text{(\pi}^0\text{)}} \pm 0.01_{\text{(Brems)}} \\ p_{1,B} &= 1.16 \pm 0.05_{\text{(stat)}} \pm 0.09_{\text{(\pi}^0\text{)}} \pm 0.00_{\text{(Brems)}}. \end{aligned} \quad (5.13)$$

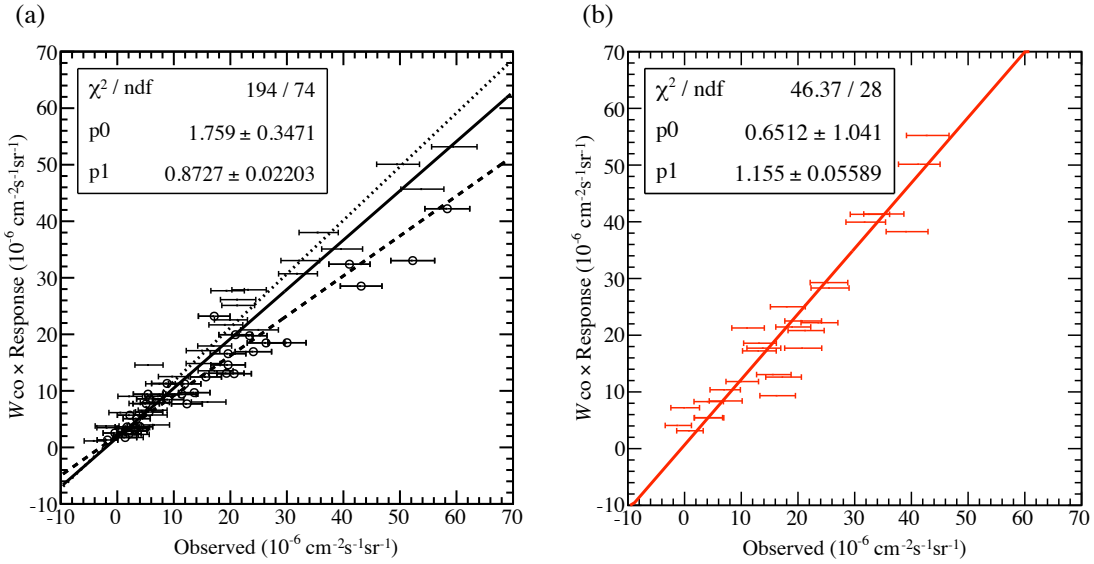


Figure 5.16: Pixel-by-pixel scatter plots between the two panels of Figure 5.15. Data are fitted with equation (5.12). (a) Orion A. A solid line shows the best fit line of all data points. Dashed and dotted are of $l > 212^\circ$ and $212^\circ > l$, respectively. Open circles correspond to pixels in the region of $l > 212^\circ$. (b) Orion B.

Here, $p_{1,A}$, p_{1,A_+} , p_{1,A_-} , and $p_{1,B}$ are the best-fit first-order coefficients of the Orion A, A_+ , A_- , and B regions. Table 5.6 summarizes the obtained fitting results with χ^2/ndf . Note that all the systematic errors move toward the same direction when H I normalizations change.

The obtained χ^2/ndf and corresponding probabilities P for Orion A, A_+ , A_- , and B regions are 194./74 ($P = 1.1 \times 10^{-12}$), 60.3/33 ($P = 0.0026$), 74.6/39 ($P = 0.00052$), and 46.4/28 ($P = 0.016$), respectively. Thus the χ^2 test for the Orion A, and significantly different slopes for three subdivided regions confirm the result in Subsection 5.2.2, namely, the observed gamma-ray surface brightness is not proportional to the assumed X_{CO} and CR flux. The probabilities for the latter three regions are not acceptable either, but their correlations are not necessarily linear relations in small subdivided regions.

Since the W_{CO} -based simulation intensity was created with a constant X_{CO} of $1.5 \times 10^{20} \text{ cm}^{-2} (\text{K km s}^{-2})^{-1}$, $1.5 \times 10^{20}/p_1$ correspond to X_{CO} in each region. Thus, equation (5.14) can be converted as given by

$$\begin{aligned} X_{\text{CO},A_+} &= (2.11 \pm 0.09_{(\text{stat})} \pm 0.18_{(\pi^0)} \pm 0.00_{(\text{Brems})}) \times 10^{20} \text{ cm}^{-2} (\text{K km s}^{-2})^{-1} \\ X_{\text{CO},A_-} &= (1.58 \pm 0.05_{(\text{stat})} \pm 0.13_{(\pi^0)} \pm 0.02_{(\text{Brems})}) \times 10^{20} \text{ cm}^{-2} (\text{K km s}^{-2})^{-1} \\ X_{\text{CO},B} &= (1.29 \pm 0.06_{(\text{stat})} \pm 0.10_{(\pi^0)} \pm 0.00_{(\text{Brems})}) \times 10^{20} \text{ cm}^{-2} (\text{K km s}^{-2})^{-1}. \end{aligned} \quad (5.14)$$

In order to remove the uncertainty of low-energy spectra and the effect of the LAT PSF, we also performed the same process with the energy band limited between 1 GeV and 20 GeV; the results are given in Figures 5.17 and 5.18. The best-fit slopes are listed in Table 5.7. The obtained correlation slopes in the 4 regions are given by

$$\begin{aligned} p_{1,A} &= 0.82 \pm 0.03_{(\text{stat})} \pm 0.07_{(\pi^0)} \pm 0.00_{(\text{Brems})} \\ p_{1,A_+} &= 0.67 \pm 0.04_{(\text{stat})} \pm 0.06_{(\pi^0)} \pm 0.00_{(\text{Brems})} \\ p_{1,A_-} &= 0.90 \pm 0.04_{(\text{stat})} \pm 0.08_{(\pi^0)} \pm 0.00_{(\text{Brems})} \\ p_{1,B} &= 1.19 \pm 0.08_{(\text{stat})} \pm 0.10_{(\pi^0)} \pm 0.00_{(\text{Brems})}. \end{aligned} \quad (5.15)$$

Table 5.6: Correlation slopes between observed intensity and a CO model above 200 MeV. Data in braces are χ^2/ndf .

π^0	H I Normalization	Orion A	Orion A_+ ($212^\circ > l$)	A_- ($l > 212^\circ$)	Orion B
	Bremsstrahlung				
1.17×0.9	1.5	0.80 ± 0.02 (200./74)	0.64 ± 0.02 (62.4/33)	0.87 ± 0.03 (78.4/39)	1.06 ± 0.05 (47.6/28)
1.17×1.0	1.5	0.87 ± 0.02 (194./74)	0.71 ± 0.03 (60.3/33)	0.95 ± 0.03 (74.6/39)	1.16 ± 0.05 (46.4/28)
1.17×1.1	1.5	0.95 ± 0.02 (189./74)	0.77 ± 0.03 (59.3/33)	1.03 ± 0.05 (72.3/39)	1.25 ± 0.06 (45.3/28)
1.17×1.0	1.2	0.86 ± 0.02 (199./74)	0.70 ± 0.03 (62.0/33)	0.94 ± 0.03 (77.8/39)	1.15 ± 0.06 (47.4/28)
1.17×1.0	1.8	0.88 ± 0.02 (190./74)	0.71 ± 0.03 (59.7/33)	0.96 ± 0.03 (72.8/39)	1.16 ± 0.06 (45.4/28)

The best-fit values in equations (5.14) and (5.15) are not different significantly. The probability of χ^2/ndf of each region improved ($P = 0.055, 0.043$, and 0.095 for A_+ , A_- , and B regions, respectively). However, this may be due to larger statistic errors than that of Figure 5.16.

As shown in Figure 5.19, we also fitted the correlations with quadratic functions

$$y = p_0 + p_1 I_{\gamma, > 1 \text{ GeV}} + p_2 I_{\gamma, > 1 \text{ GeV}}^2 \quad (5.16)$$

to examine the plots for non-linear relations. While the inclusion of the quadratic term did not improve the fit significantly in the Orion A data, the best-fit function shows concave shape only in the Orion B region. The obtained best-fit coefficients p_1 are listed in Table 5.8, and summarized as

$$\begin{aligned} p_{1,A} &= 0.80 \pm 0.06_{(\text{stat})} \pm 0.08_{(\pi^0)} \pm 0.01_{(\text{Brems})} \\ p_{1,A_+} &= 0.66 \pm 0.06_{(\text{stat})} \pm 0.07_{(\pi^0)} \pm 0.01_{(\text{Brems})} \\ p_{1,A_-} &= 0.99 \pm 0.09_{(\text{stat})} \pm 0.09_{(\pi^0)} \pm 0.01_{(\text{Brems})} \\ p_{1,B} &= 0.78 \pm 0.16_{(\text{stat})} \pm 0.10_{(\pi^0)} \pm 0.02_{(\text{Brems})}. \end{aligned} \quad (5.17)$$

By allowing $p_2 \neq 0$, the value of p_1 has become consistent between Orion A and Orion B, while at the same time, p_1 for A_+ and A_- are still inconsistent. The obtained χ^2/ndf for Orion B in equations (5.15) and (5.17) are $38.2/28$ ($P = 0.095$) and $34.2/27$ ($P = 0.183$) which are both acceptable. We cannot distinguish these two fittings with current photon statistics. However, if the concave shape of Figure 5.19b is real, this suggests that the gamma-ray emissivity tends saturate toward the core of Orion B, and may explain the discrepancy between the observed gamma-ray count and W_{CO} -based simulation.

If the non-linear relation is partially explained by strong magnetic fields inside MC cores, and magnetic reflection of CRs, the discrepancy between the observed gamma-ray count and W_{CO} may become larger in a lower energy band. This is because the gyroradii of charged CRs are proportional to their energies, and thus higher-energy particles are more possible to penetrate denser gas. As shown in Figure 5.20, we hence created additional scatter plots using photons in the energy limited between 200 MeV and 1 GeV. However, significant difference between Figures 5.18 and 5.20 is not found.

5.4.4 Correlation with Dusts

As an alternative indicator of MCs, we may utilize the amount of interstellar dusts, which in turn is represented by the visual extinction (A_V) map produced by Dobashi et al. (2005) using the star counting

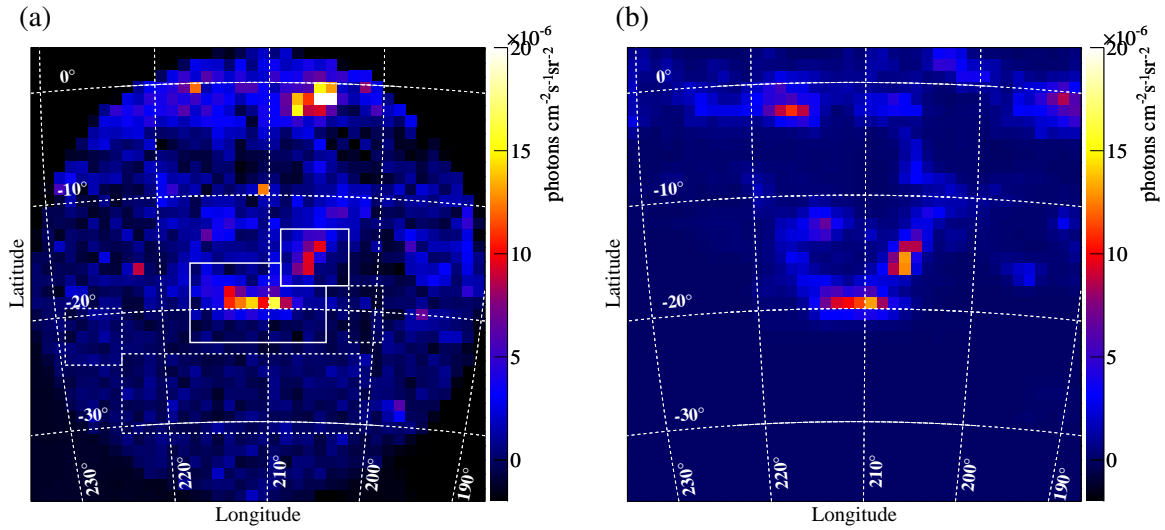


Figure 5.17: Same as Figure 5.15, but in energies above 1 GeV.

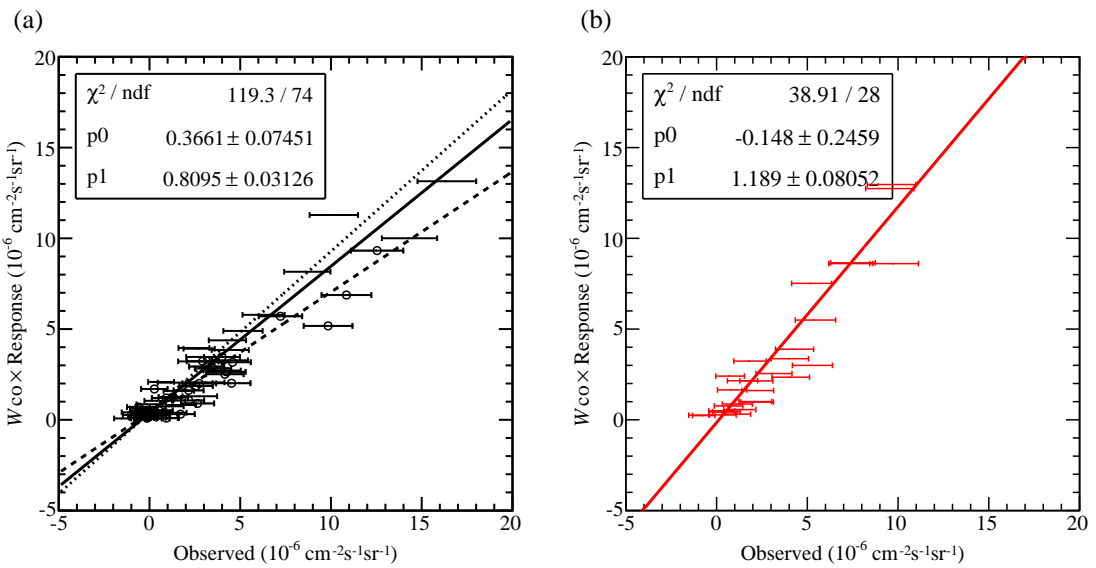


Figure 5.18: Same as Figure 5.16, but in energies above 1 GeV.

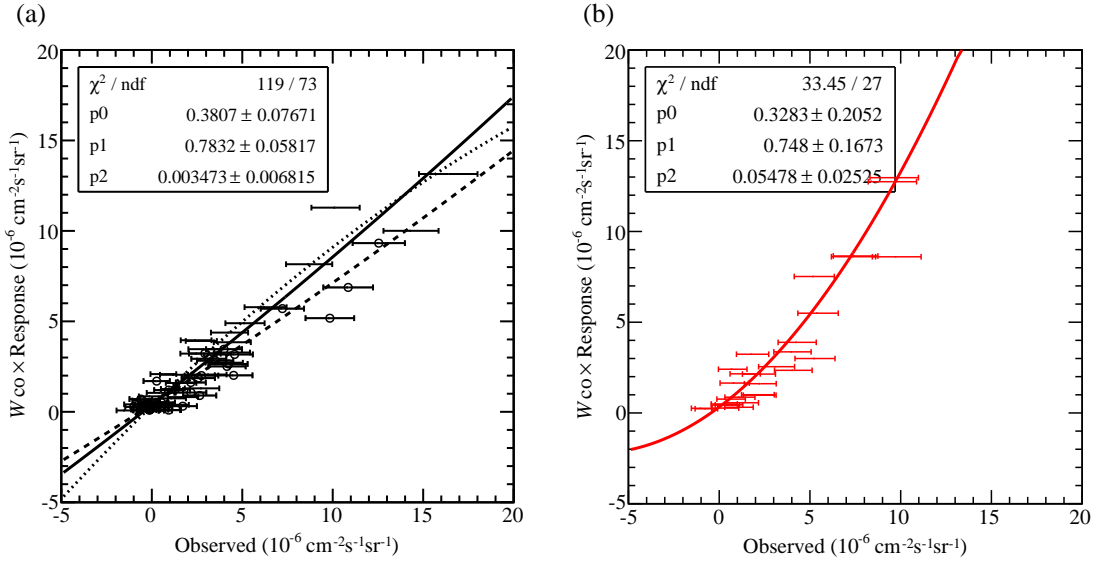


Figure 5.19: Same as Figure 5.18, but the data are fitted with equation (5.16).

Table 5.7: Same as Table 5.6, but only using events of with energies above 1 GeV.

H I Normalization		Orion A	Orion A ₊ ($212^\circ > l$)	A ₋ ($l > 212^\circ$)	Orion B
π^0	Bremsstrahlung				
1.17×0.9	1.5	0.74 ± 0.03 (120./74)	0.61 ± 0.03 (47.0/33)	0.81 ± 0.04 (56.7/39)	1.09 ± 0.07 (39.0/28)
1.17×1.0	1.5	0.82 ± 0.03 (118./74)	0.67 ± 0.04 (46.9/33)	0.90 ± 0.04 (55.3/39)	1.19 ± 0.08 (38.2/28)
1.17×1.1	1.5	0.89 ± 0.03 (116./74)	0.74 ± 0.04 (46.9/33)	0.98 ± 0.05 (54.2/39)	1.30 ± 0.09 (37.5/28)
1.17×1.0	1.2	0.81 ± 0.03 (119./74)	0.67 ± 0.04 (46.9/33)	0.89 ± 0.04 (56.1/39)	1.19 ± 0.08 (38.6/28)
1.17×1.0	1.8	0.82 ± 0.03 (117./74)	0.67 ± 0.04 (46.9/33)	0.90 ± 0.05 (54.7/39)	1.20 ± 0.08 (37.8/28)

Table 5.8: Same as Table 5.7, but using equation (5.16).

$H\ I$ Normalization π^0	Bremsstrahlung	Orion A	Orion A_+ ($212^\circ > l$)	A_- ($l > 212^\circ$)	Orion B
1.17×0.9	1.5	0.72 ± 0.05 (119./73)	0.59 ± 0.06 (46.9/32)	0.90 ± 0.7 (55.5/38)	0.68 ± 0.15 (33.5/27)
1.17×1.0	1.5	0.80 ± 0.06 (117./73)	0.66 ± 0.06 (46.8/32)	0.99 ± 0.09 (53.9/38)	0.78 ± 0.16 (33.0/27)
1.17×1.1	1.5	0.88 ± 0.02 (116./73)	0.73 ± 0.04 (46.9/32)	1.09 ± 0.09 (52.5/38)	0.88 ± 0.17 (32.5/27)
1.17×1.0	1.2	0.79 ± 0.06 (118./73)	0.65 ± 0.07 (46.8/32)	0.98 ± 0.09 (54.7/38)	0.76 ± 0.16 (33.3/27)
1.17×1.0	1.8	0.81 ± 0.06 (117./73)	0.67 ± 0.06 (56.9/32)	1.00 ± 0.08 (53.1/38)	0.80 ± 0.16 (32.7/27)

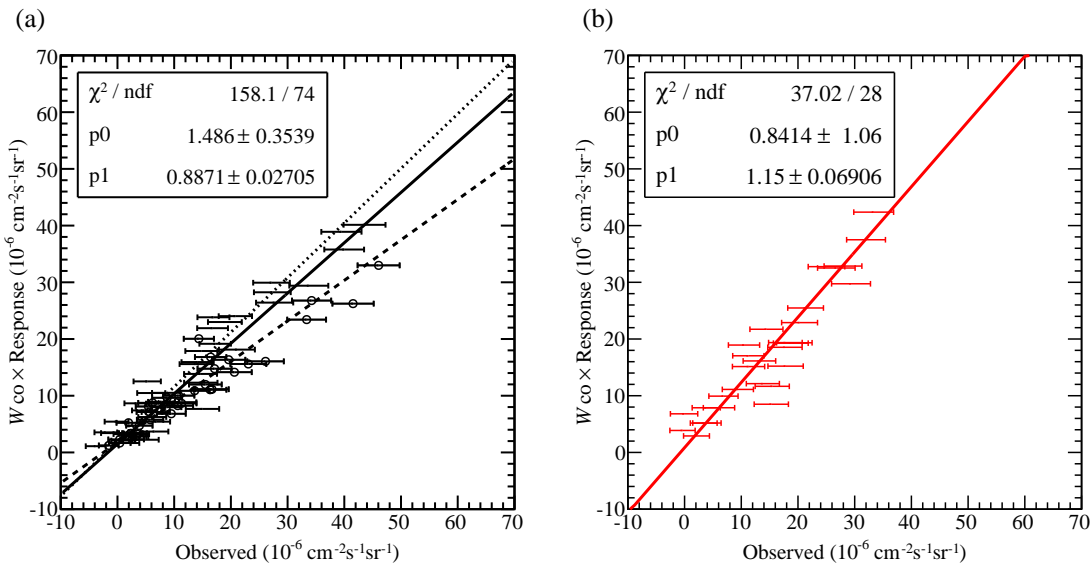


Figure 5.20: Same as Figure 5.16, but in energies between 200 MeV and 1 GeV.

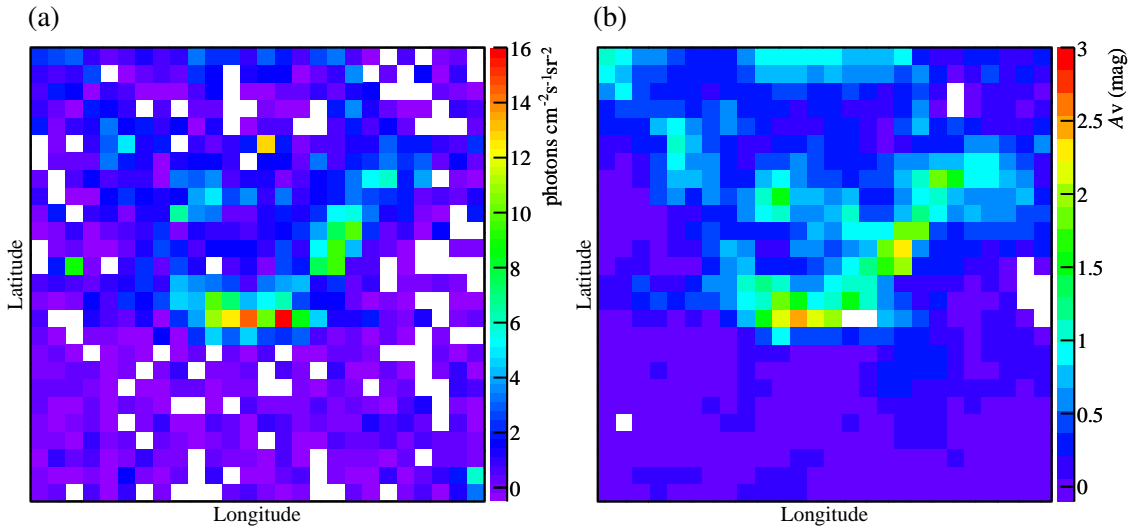


Figure 5.21: (a) Same as Figure 5.17a, but only 26×26 pixels are shown. White pixels are negative due to statistical fluctuations. (b) The A_V map by Dobashi et al. (2005) rebinned into $1 \times 1^\circ$ pixels. Data in white pixels are not available due to bright stars.

technique (Figure 2.12e). If the dust to gas ratio is approximately constant inside MCs, and the property of dust grains (grain size and extinction coefficient) is not affected by gas density or temperature, the A_V map will be a better “mass tracer” of MCs. However, interstellar dusts also exists inside H I gas. Thus, the A_V map contains not only MCs, but also H I gas in the background and foreground. For example, comparing Figures 2.12d and 2.12d, we can observe similar structure around $(l, b) = (205^\circ, -30^\circ)$, $(l, b) = (220^\circ, -15^\circ)$, and the Galactic plane. Moreover, the star count technique is not applicable to a region where optical emission from stars and nebula is too bright. Therefore, the A_V data of the Orion A core (the Orion nebula) is not available. As a result, the A_V map may be in some sense complementary to the CO map. It shows a “bright” part around $(l, b) = (215^\circ, -25^\circ)$, while CO intensity is less bright in the same region.

It is not trivial to remove the H I component from the A_V map. However, if we consider H I to provide an approximately uniform offset on small scales ($\sim 5^\circ$), we can still study the correlation between the gamma-ray intensity and A_V . The effect by the offset can be reduced when we set p_0 free. We hence rebinned Figure 2.12e into $1^\circ \times 1^\circ$ pixels as shown in Figure 5.21; The rebinned A_V map contains two invalid pixels at the Orion A core which are not used in the present analysis.

We correlated Figures 5.21a and 5.21b pixel by pixel, and created a scatter plot as shown in Figure 5.22. Unlike Figure 5.18, we can see similar distributions of data points between Orion A and B, and between A_+ and A_- . This suggests that the observed gamma-ray intensity and A_V are raised by the same origin.

We fitted them with equations (5.12) and (5.16) as shown in Figure 5.22 and 5.23, respectively. Table 5.9 summarizes the best-fit p_1 for each region. When we use the linear function, the best-fit p_1 becomes similar values within 15%. However, the probability of χ^2/ndf of A_+ , A_- , and B are 0.02, 0.0002, and 0.0005, respectively. While in equation (5.15), the ratio between p_{1,A_+} and $p_{1,B}$ is 1.78, that of the correlation with A_V is only 1.06. However, by fitting the best-fit three p_1 with a constant value, we obtain $\langle p_1 \rangle = 0.228 \pm 0.008$ ($\chi^2/\text{ndf} = 14.2/2$; $P = 0.0008$) which is not consistent with an assumption of a constant p_1 .

The quadratic function improved χ^2/ndf compared to the linear function. The probability of χ^2/ndf

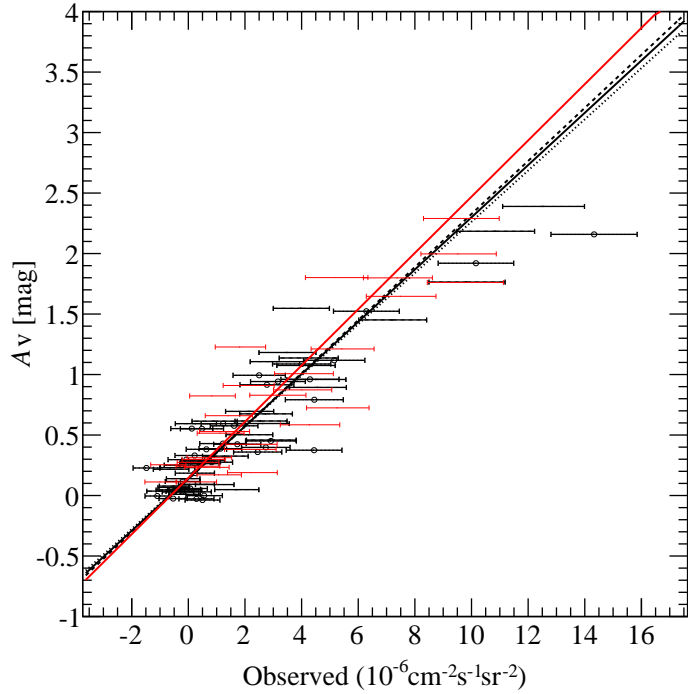


Figure 5.22: Correlations between the observed gamma-ray intensity and A_V . Black and red points show data of the Orion A and B regions, respectively. Black open circles indicate the left part of Orion A. Black solid, black dashed, black dotted, and red lines are the best fit functions for Orion A, the left part of Orion A, the right part of Orion A, and Orion B, respectively.

of A_+ , A_- , and B are 0.05, 0.001, and 0.0004, respectively. If we fit the best-fit p_1 with a constant again, we obtain $\langle p_1 \rangle = 0.257 \pm 0.015$ ($\chi^2/\text{ndf} = 0.10/2$; $P = 0.95$) with a large p -value. All best-fit functions become convex, however, their linear terms are consistent with each other, and they show similar shapes in the A_V range below ~ 2 . Although the quadratic fittings show non-linear tendency in the $A_V > 2$ regions, the results suggest that A_V is a better “mass tracer” in less dense gas regions than W_{CO} maps. The nonlinearity in dense regions ($A_V > 2$) is considered to be caused by systematic errors of the A_V map⁴.

5.5 The Maximum Likelihood Analysis

The maximum likelihood method is the standard analysis method officially adopted in the *Fermi*/LAT collaboration. The method is known to be more powerful and appropriate than the χ^2 method, when analyzing data of low photon statistics by fully considering the strongly energy-dependent PSF (Mattox et al., 1996). If our emission models are perfect spatially and spectrally, a likelihood fitting will converge within statistical fluctuations. By using the method, we can confirm the discrepancy between the gamma-ray intensity and W_{CO} map. We also examine if the assumed spin temperature of H I gas change the results in the previous sections. We first describe about the standard analysis method in Subsection 5.5.1, and perform likelihood analyses in Subsections 5.5.2 and 5.5.3.

⁴The star counting technique is affected by bright star light in dense MC cores.

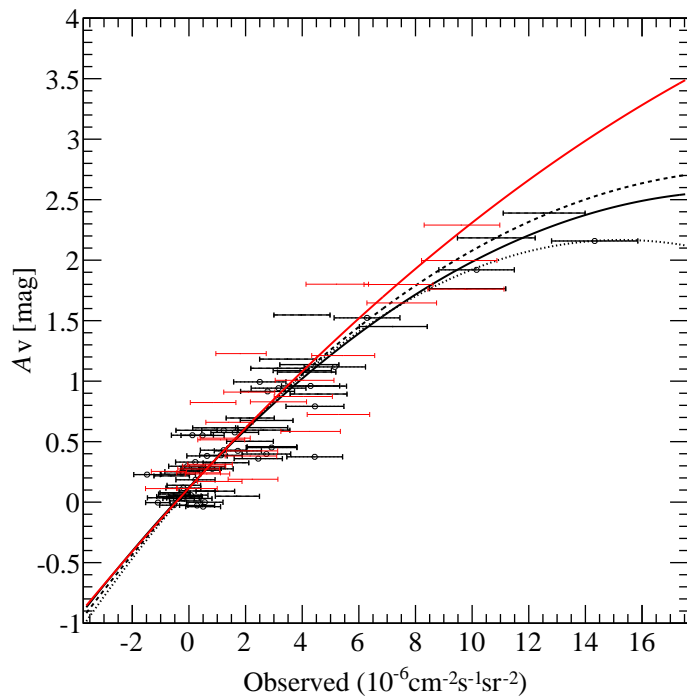


Figure 5.23: Same as Figure 5.22, but fitted with quadratic functions.

Table 5.9: Correlation slopes p_1 between the observed gamma-ray intensity and A_V .

Function	Orion A	$A_+ (l > 212^\circ)$	$A_- (212^\circ > l)$	Orion B
$y = p_0 + p_1 I_{\gamma, > 1 \text{ GeV}}$	0.209 ± 0.009 (123./67)	0.219 ± 0.013 (51.6/33)	0.192 ± 0.013 (68.1/32)	0.232 ± 0.017 (59.0/28)
$y = p_0 + p_1 I_{\gamma, > 1 \text{ GeV}} + p_2 I_{\gamma, > 1 \text{ GeV}}^2$	0.244 ± 0.013 (113./66)	0.261 ± 0.021 (45.8/32)	0.251 ± 0.025 (60.4/31)	0.255 ± 0.035 (58.4/27)

5.5.1 Science Tools and *gtlike*

Distributed to public by NASA⁵⁶, *Science Tools* is the standard software package commonly used to analyze the *Fermi*/LAT data. It offers useful commands and libraries which enable users to analyze the data easily. In the simplest analyses of steady point sources, users are required to follow the steps listed below to calculate the energy spectra of targeting point sources with the maximum likelihood method.

1. Event Selection

First, we obtain an event data set which includes photon-like events inside our ROI. Each event has information of its reconstructed arrival direction and energy, as well as the trigger time. In addition to the data set, we also need flight data containing a history of the LAT direction, elevation, geographic coordinates and time.

2. Exposure Calculation

Second, we calculate energy-dependent and coordinates-dependent exposures (exposure cube⁷). This can be done by referring to the energy- and angle-dependent LAT responses, and to the LAT attitude information mentioned in 1.

3. Diffuse Model Selection

In an ordinary point source analysis, we defines a diffuse emission model which behaves as a background against point sources. As described in Section 5.1, the model is usually constructed using GALPROP except for the isotropic components. On the other hand, in a diffuse source analysis, a diffuse emission model of our targeting source also needs to be given. In our case, we modeled gamma-ray emission from the Orion MCs using a W_{CO} map.

4. Point Source Selection

In addition to the diffuse emission, there exist galactic or extragalactic gamma-ray point sources. Those inside or nearby the ROI are collected, and their spectral shapes are determined by fitting the data with appropriate spectral models.

5. Maximum Likelihood Fitting

Using the maximum likelihood method, the spectral shapes of point sources and the normalization of the diffuse emission are optimized to best reproduce the observed photon count map. *gtlike* (Glast Tool LIKElihood), which is one of the commands in *Science Tools*, performs this optimization. A brief explanation of the maximum likelihood method is given in appendix B.

Unlike the first-cut analysis performed in Section 5.2, a *gtlike* analysis takes into account the contributions from point sources and the LAT PSF. Although the maximum likelihood method can yield a set of model parameters that are best favored by the data, it cannot tell to what extent the model can reproduce the data. In addition, the result is of little meaning if the selected model is wrong.

5.5.2 *gtlike* results on ROI 2

We first performed a *gtlike* analysis on the data set 2 employing the emission model “54_77Xvarh7S”. This model is known to roughly reproduce the observed LAT emission map except for the Galactic plane and small structure of dense gases (Strong, 2009). It assumes $X_{\text{CO}} = 1.5 \times 10^{20} \text{ cm}^{-2}(\text{K km s}^{-2})^{-1}$, which is not much different from what we found in Section 5.2 through our simple analysis. Thus, we did not change the ratio among emission components (Ⓐ, Ⓑ, Ⓒ, Ⓓ, and Ⓔ) listed in Table 5.1, while left

⁵<http://fermi.gsfc.nasa.gov/ssc/>

⁶Version v9r13p0 is used in the present analyses.

⁷Hereafter we refer to 2D images as “map”s, and 3D (2D space + energy) images as “cube”s.

Table 5.10: A likelihood result[†] of “54_77Xvarh7S”. Fitting parameters of point sources are not listed.

Component	Normalization	N_0 ($10^{-7} \text{cm}^{-2}\text{s}^{-2}\text{sr}^{-2}\text{MeV}^{-1}$)	Γ
“54_77Xvarh7S”	1.0120 ± 0.0006	–	–
Isotropic	–	1.9717 ± 0.0032	2.3303 ± 0.0009

[†]Errors are statistical only.

free the overall normalization of “54_77Xvarh7S”. We assumed that (C), (F), (I), and (J) can be combined into a single power law given by

$$\frac{dN}{dE} = N_0 \left(\frac{E}{100 \text{ MeV}} \right)^{-\Gamma}, \quad (5.18)$$

where E is the gamma-ray energy, Γ is a photon index, and N_0 is a normalization factor. Both N_0 and Γ are free parameters. The normalization of “54_77Xvarh7S” was set free. In addition to these diffuse and isotropic components, there exist point sources detected at high significance levels ($> 5\sigma$) by the LAT team internally. Among them, we included those within a radius of 20° from the center of the ROI, and assumed that their energy spectra are described by power laws.

Through the *gtlike* analysis of the data set 2 described above, we have obtained the optimized parameters as given in Table 5.10, and the fitting results as summarized in Figure 5.24. In the figure, panel (a) shows the observed 200 MeV – 20 GeV count map binned into $0.25^\circ \times 0.25^\circ$ pixels, while (b) represents the “best fit” model prediction (with infinite photon statistics), implied by the parameters in Table 5.10, the exposure cubes, and the LAT PSF⁸. Thus, the best-fit numerical model, consisting of “54_77Xvarh7S”, an isotropic background, and 23 point sources, reproduce the general appearance of the LAT count map in the 200 MeV – 20 GeV rang. However, Figure 5.24c, namely the data vs. model difference, clearly shows significant positive excess at the left part of Orion A, and negative excess at Orion B. Figures 5.24d and 5.24e show the same residuals in 8 sliced bands parallel to the horizontal axis. We can see that the fitting result reproduces the observed count map in lower 5 bands, while reduced χ^2 exceed 2 in upper 3 bands which include the Orion clouds⁹. The model vs. data mismatch typically amounts to $\sim 10 - 20\%$ in the Orion A and B regions.

Figure 5.25 compares the observed spectrum, against the optimized spectra of all considered sources; the diffuse model, the isotropic component, and point sources. In spite of the $\sim 10 - 20\%$ discrepancy in the surface brightness distribution, the spectrum fitting works well. This is because, in general, the maximum likelihood method progresses to make model spectra match with the observed total spectrum, even if there exist spatial discrepancy.

⁸From the EGRET observations, Sreekumar et al. (1998) obtained the isotropic component as $N_0 = 1.73 \pm 0.08$ and $\Gamma = 2.10 \pm 0.03$.

⁹The maximum likelihood method performs an optimization of fitting parameters, but it does not test the given hypothesis unlike the χ^2 fitting. Although we listed χ^2/ndf for reference in Figure 5.24e, in fact, ndf (number of degrees of freedom) cannot be defined in the method directly. The given ndf in Figure 5.24e are the same as the number of bins of sliced bands.

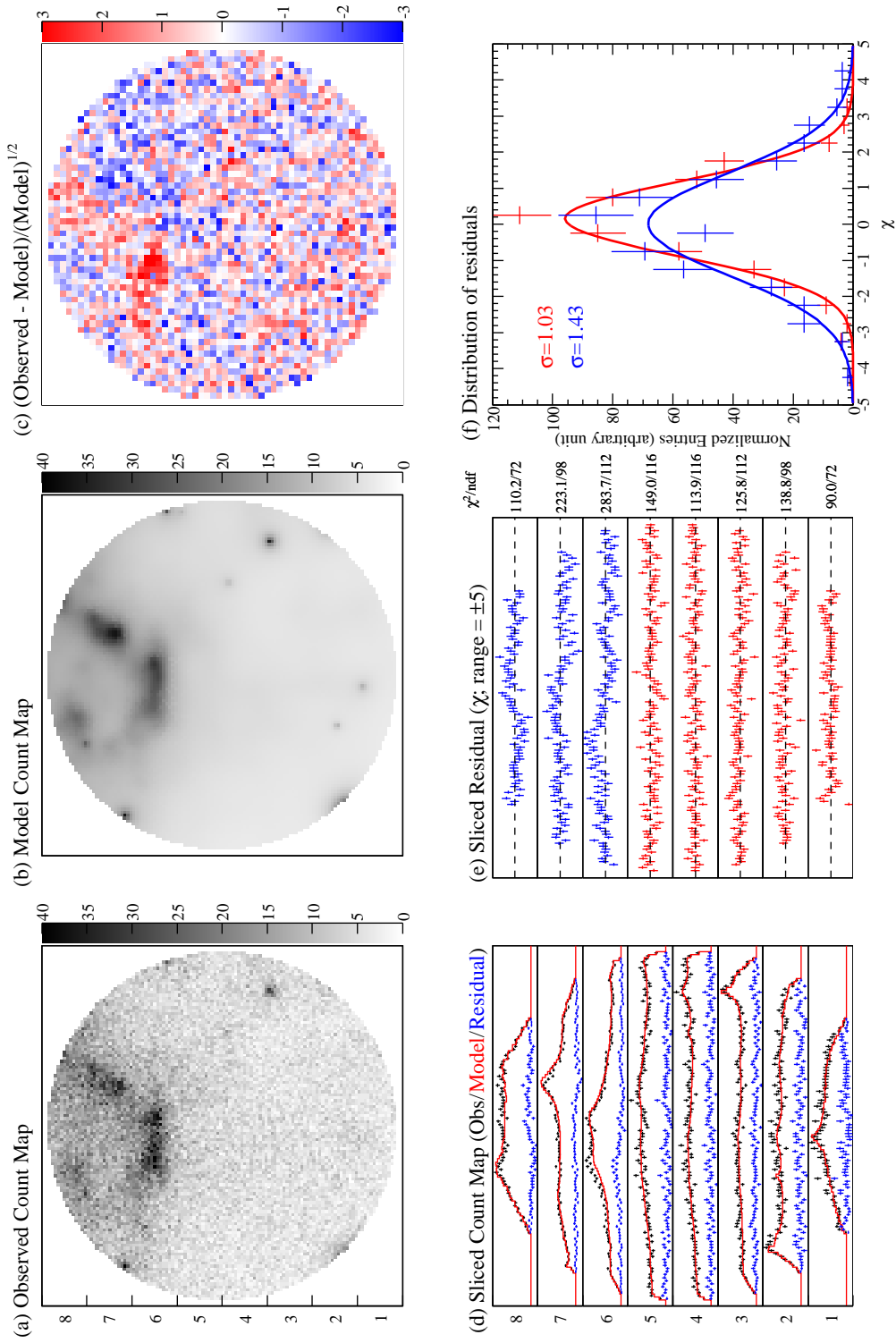


Figure 5.24: Results of the *gtlike* analysis of the data set 2, using the model “54_77Xvarh7S”. (a) The 200 MeV – 20 GeV count map of the data set 2 binned into 120×120 pixels. (b) A count map predicted by the best-fit model. (c) The residual map, $(\text{observed} - \text{model})/\sqrt{\text{model}}$, binned into 60×60 pixels. (d) Sliced count maps of the observed (black) and the model (red). Each band (1 – 8) is a projection of 120×15 pixels onto the x axis. Blue points show the residual (observed - model). (e) Same as the blue data points in panel (d), but the scale of the y axis is χ in the range between -3 and 3 . Two colors, blue and red, refer to panel (f). Values on the right side are χ^2 and the number of bins of each band. (f) Distributions of χ in upper 3 bands (blue) and lower 5 bands (red).

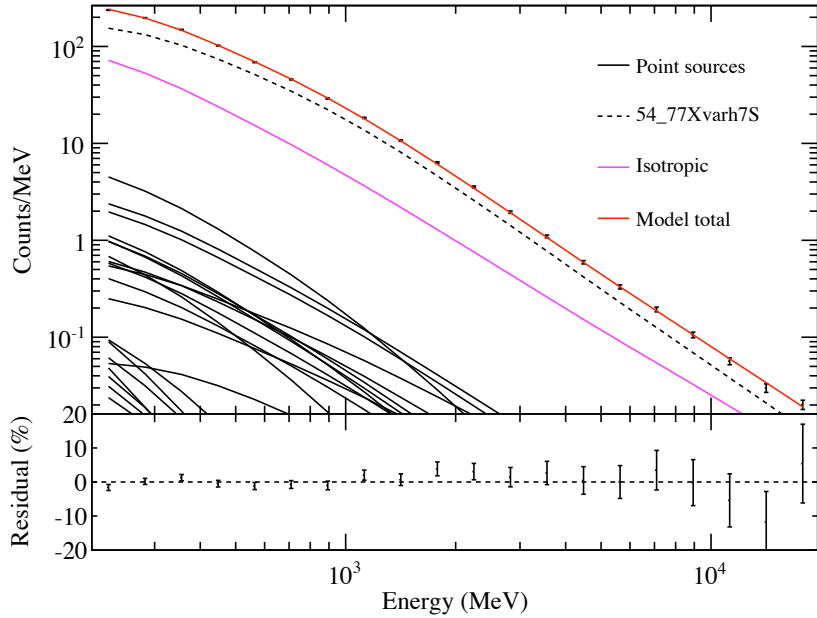


Figure 5.25: The total count spectrum of the data set 2 (black dots), compared with the best-fit model (red curve) including “54_77Xvarh7S” (black dashed curve). The counts are not corrected for the exposure.

5.5.3 Attempts of model improvement

The *gtlike* analysis has reconfirmed our inferences made in Section 5.2. That is, the overall gamma-ray emission from the Orion region is indeed dominated by π^0 signals from ISM, but its surface brightness exhibits $\sim 10 -- 20\%$ deviation from the simplest assumption of a constant X_{CO} and a constant CR flux. Let us attempt to better reproduce the observation by improving the emission models (Table 5.4).

So far, we have employed the emission model “54_77Xvarh7S”, which uses a constant X_{CO} as given by equation (5.8); namely, the ratio between H I and H₂ emissions is fixed. This assumption may well be too simplified and may become one of the causes of the residual. We hence repeated the *gtlike* fit with the “54_78Xvarh7O” model, in which the normalizations of π^0 and bremsstrahlung components of both H I and H₂ were set free. Table 5.11 shows the resultant fitting parameters of this model. We further allowed the IC emission to have a free normalization, and obtained the results in Table 5.12. However, as can be seen from the residual maps and the best fitted spectra shown in Figures C.1, C.2, C.3, and C.4, the residual at the Orion clouds did not improve in either case, in spite of additional fitting parameters.

Comparing Table 5.11 with 5.12, we find that the best fit normalization of the π^0 component of H I and H₂ can easily change by $\sim 10\%$, while the fitting result did not change significantly. When the normalization of the IC emission is set free, its best fit value became 3 times larger than the GALPROP prediction. At the same time, the normalization of the isotropic component converged on a smaller value compared to that of Table 5.11. We thus take two lessons from these attempts. One is that the data cannot constrain the individual emission components to better than $\sim 10\%$, because they have rather similar shapes. Considering this, as well as the intrinsic $\sim 10\%$ uncertainty involved in the emissivity calculations (Section 5.3), we must assign ~ 10 and $\sim 20\%$ systematic uncertainties to the π^0 and bremsstrahlung emission from the region, respectively. The other lesson is that the data vs. model mismatch, observed in the surface brightness maps, cannot be eliminated by simply changing the value of X_{CO} , or adjusting the electron contributions.

The *gtlike* results described so far utilized the H I map which was constructed assuming a spin tem-

Table 5.11: A likelihood result of “54_78Xvarh7O”. Fitting parameters of point sources are not listed.

Component	Normalization	N_0 ($10^{-7}\text{cm}^{-2}\text{s}^{-1}\text{sr}^{-2}\text{MeV}^{-1}$)	Γ
π^0 (H I)	1.069 ± 0.003	–	–
π^0 (H ₂)	1.032 ± 0.005	–	–
Bremsstrahlung (H I)	1.769 ± 0.009	–	–
Bremsstrahlung (H ₂)	1.098 ± 0.015	–	–
Isotropic	–	1.975 ± 0.006	2.281 ± 0.002

Table 5.12: A likelihood result of “54_78Xvarh7O”. Same as Table 5.11, but the normalization of IC emission was set free.

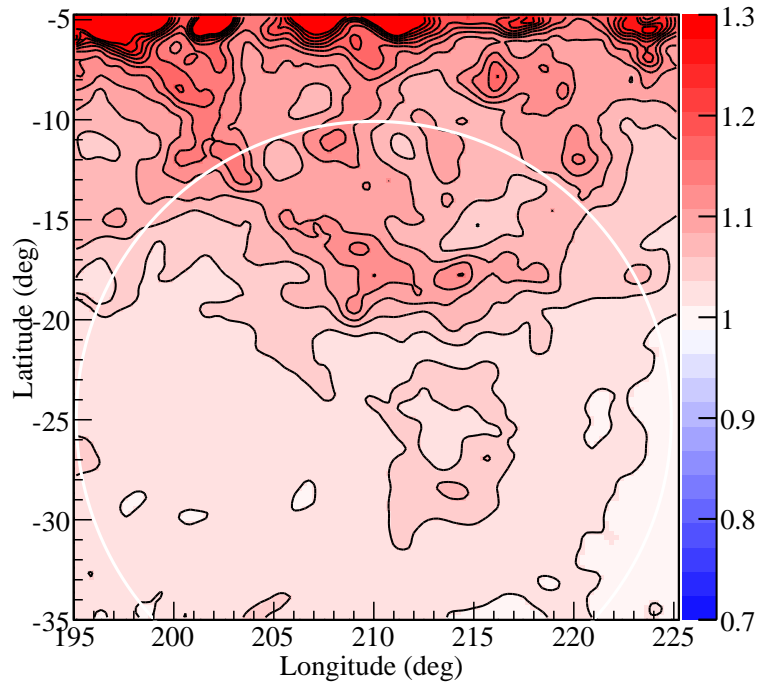
Component	Normalization	N_0 ($10^{-7}\text{cm}^{-2}\text{s}^{-1}\text{sr}^{-2}\text{MeV}^{-1}$)	Γ
π^0 (H I)	1.172 ± 0.008	–	–
π^0 (H ₂)	1.046 ± 0.012	–	–
Bremsstrahlung (H I)	1.392 ± 0.024	–	–
Bremsstrahlung (H ₂)	0.994 ± 0.040	–	–
IC	2.945 ± 0.029	–	–
Isotropic	–	1.488 ± 0.020	2.420 ± 0.008

perature of 125 K. The residuals in Figures 5.24, C.2, and C.1 may be caused by this assumption because, as explained in Subsection 2.2.1, optical-depth correction for the H I column density depends on the assumed spin temperature. We hence constructed two more H I maps assuming $T_s = 100$ K or $T_s = 100000$ K, according to equation (2.4). Figure 5.26 shows these H I maps relative to that with $T_s = 125$ K. The difference between these maps is more than 10% in the region of $b > -20^\circ$, while less than 5% in the lower region where H I density is relatively low compared to the upper region. These alternative assumptions yielded two new models, “54_78Xvarh7O.Ts100” and “54_78Xvarh7O.Ts100000” (Table 5.4). However, as shown in Table C.1 and C.2, and Figures C.5, C.6, C.7, and C.8, the *gtlike* fits using these models gave essentially the same results as before.

5.5.4 Summary of the *gtlike* analysis

From the results obtained with the maximum likelihood method and several emission models, we have confirmed the results in the previous sections that the simple assumption of a constant X_{CO} and a uniform CR distribution inside MCs is not correct. We still have uncertainty in determining the normalizations of π^0 and bremsstrahlung emissions from H I gas which should be subtracted when we analyze only the Orion clouds. In addition to our *gtlike* result, a different normalization factor is derived by other member in the LAT team by a “global fitting” which uses all photon data in high-latitude region ($|b| > 10^\circ$). Table 5.13 shows the normalization factors obtained in our analysis and his. The latter method is less affected by small structure of MCs, however it uses all the emission coming from different coordinates of the Galaxy. Since these three normalization factors are within $\pm 10\%$, we use 1.17 as a nominal normalization factor for π^0 emission with $\pm 10\%$ systematic error. This factor, +17% is similar to the neglected contribution from heavier particles in GALPROP. On the contrary, the variation of the factor for bremsstrahlung component is large. We adopt 1.50 as a nominal value with $\pm 20\%$ systematic error.

(a) $T_s=100/T_s=125$



(b) $T_s=100000/T_s=125$

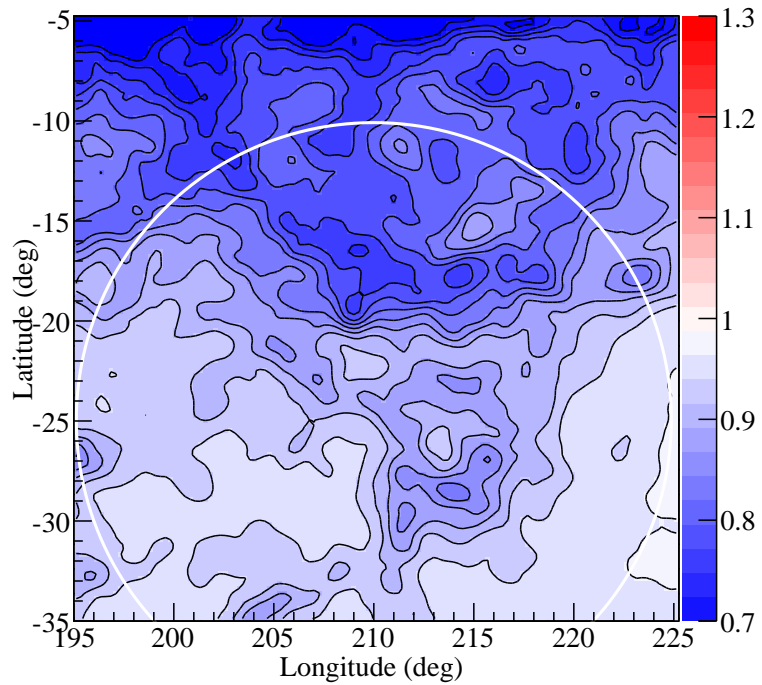


Figure 5.26: Effects of the assumed spin temperature T_s on the derived H I map. (a) The ratio between the H I map constructed with $T_s = 100$ K to that with $T_s = 125$ K. (b) The ratio between $T_s = 100000$ K and $T_s = 125$ K maps. The white circle shows ROI 2.

Table 5.13: Summary of *gtlike* results of the model “54_78Xvarh7O”. The result of “global fitting” is also listed.

H I Normalization		ROI	IC normalization
π^0	Bremsstrahlung		
1.069 ± 0.003	1.769 ± 0.009	2	Fixed
1.172 ± 0.008	1.392 ± 0.024	2	Free
1.280 ± 0.004	1.280 ± 0.004	$ b > 10^\circ$	Free

These normalization uncertainties are already included in Section 5.4.

5.5.5 Significance map

As shown in Figures 5.24, C.1, C.2, C.5, and C.6, there exist negative and positive excesses at the Orion B and A₊ regions, respectively. These excesses are connected to the non-linear relation between W_{CO} and gamma-ray intensity, as presented in the previous sections. Here we present the significance map of the positive excess in the A₊ region.

By putting a virtual “point source” of a single power law in the region, we calculated a test statistic (TS) at each point in the 0.25° grid using the maximum likelihood method (see appendix B). The obtained significance ($\sqrt{\text{TS}}$) map in the region is shown in Figure 5.27a. The most significant position in the map is $(l, b) = (213.14^\circ, -18.917^\circ)$. If we assume this excess as a real point source, its error radii (68%, 95%, 99%) are $(0.20^\circ, 0.24^\circ, 0.32^\circ)$, respectively, while there is not a potential gamma-ray source candidate inside the 99% radius (Healey et al., 2008; Green, 2009; Liu et al., 2007, 2006; Manchester et al., 2005; Roberts, 2004). The obtained best-fit power law index is -2.526 ± 0.008 which is similar to the spectral shape of π^0 gamma rays.

The significance map clearly shows extended structure much larger than the error radii, and thus, this excess is not a point-source like. In Figures 5.27b, 5.27c, and 5.27d, contour lines of 1σ intervals are overlaid on different maps of the region. As already discussed above, this region is less bright in the CO line, while bright in gamma ray and A_V . Comparing Figures 5.27b and 5.27d, we can observe that the extended structure of the significance map traces the outskirts of the Orion A cloud which is not detected by CO, but detected by A_V . Thus, we conclude that the positive excess in the Orion A₊ region is not a point source contamination, but one of existence proofs of a mass distribution not traced by CO observations.

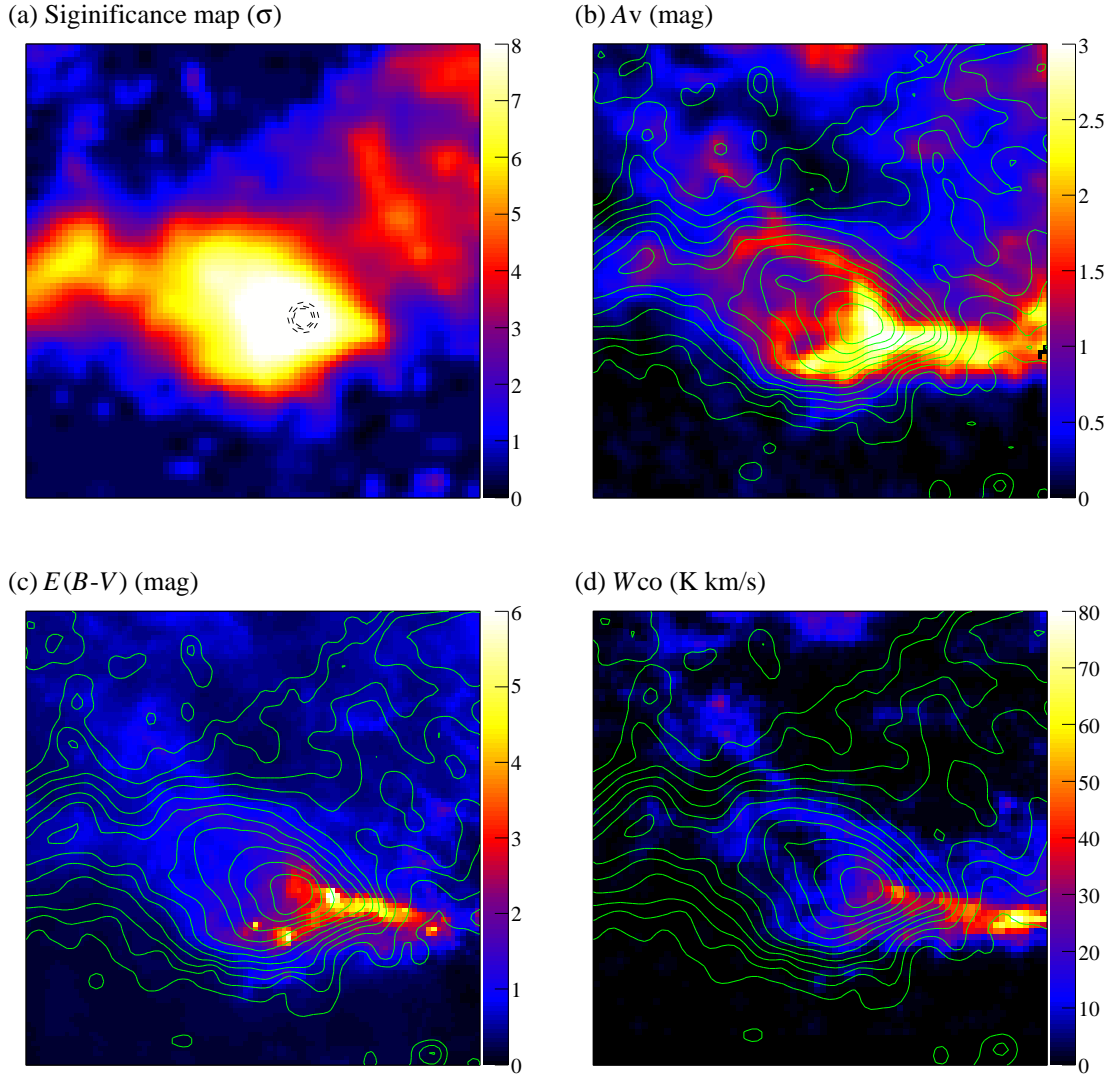


Figure 5.27: (a) The significance map of the Orion A₊ region in the 0.25° grid. Three circles show 68%, 95%, 99% radii of the most significant position, respectively. (b), (c), (d) The contours of the significance in one- σ intervals is superposed on an A_V map by Dobashi et al. (2005), a dust map by Schlegel et al. (1998), and a CO map by Dame et al. (2001), respectively.

Chapter 6

DISCUSSION

6.1 Cosmic Rays and π^0 Gamma Rays

6.1.1 Diffuse gamma-ray spectra of H I and H₂ gases

The observed gamma-ray spectra from H I and H₂ gases in the Orion region are consistent with the expected emissivity calculation in the energy range between 200 MeV and 20 GeV (Figure 5.6). We did not see the “GeV excess”-like spectral shape in the result, and thus, the EGRET “GeV excess” is considered to have been caused by an instrumental effect. Figure 6.1 shows a comparison between the EGRET observations of the Orion region (Digel et al., 1999) and our results¹. We calculated a π^0 gamma-ray emissivity model assuming a combination of recent works; π^0 cross sections by Kamae et al. (2006); Gaisser & Schaefer (1992); Mori (2009), an H I map by the LAB survey (Kalberla et al., 2005), and CR spectra adopted by GALPROP. The spectral index of the latter is 2.75. Therefore, that of the CR spectra in the Orion region is considered to be of similar value.

6.1.2 CR flux in the Orion region

When we fit the observed gamma-ray emissivity spectrum of H I gas with the expected model without the lowest energy point, the best-fit normalization factor becomes 0.92 ± 0.05 (Subsection 5.2.1) which corresponds to the relative CR flux at the Orion region, while the assumed CR spectra at the Earth (Figure 2.2), the LAT response, the H I map, and π^0 model all have 5 to 10% systematic uncertainties. If these systematic errors can be ignored, the scaling factor indicates that the CR flux in the Orion region is $8 \pm 5\%$ less than that observed at the Earth. The line-of-sight velocity of the clouds studied by CO observations are known to vary from 2 km/s to 15 km/s (Wilson et al., 2005). Those of H I gas in ROI 2 are also concentrated in the same velocity range (Kalberla et al., 2005). Thus, most of the H I gas in ROI 2 is considered to be associated with the Orion MCs; namely, the clouds are encapsulated in the H I gas. If we assume 400 pc to be a typical distance to these gases, and $(l, b) \sim (210^\circ, -20^\circ)$ to be their typical Galactic coordinates, their Galactocentric locations become $(R, Z) \sim (8.8 \text{ kpc}, -0.15 \text{ kpc})$. Thus what we measured is a line-of-sight averaged CR density near the Galactic location. It is noteworthy that GALPROP predicts similar CR normalization of $\sim 92\%$ in this region (see Figure 5.13).

¹Digel et al. (1999) calculated the gamma-ray emissivity from H I and H₂ gases simultaneously using an energy bin-by-bin maximum likelihood method assuming a spatially constant X_{CO} , while we calculated H I emissivity first, then subtracted them from all the photons in ROI 2 (Section 5.2). Thus, the lowest energy bin of our emissivity from H₂ is strongly affected by the statistical fluctuation of that of H I.

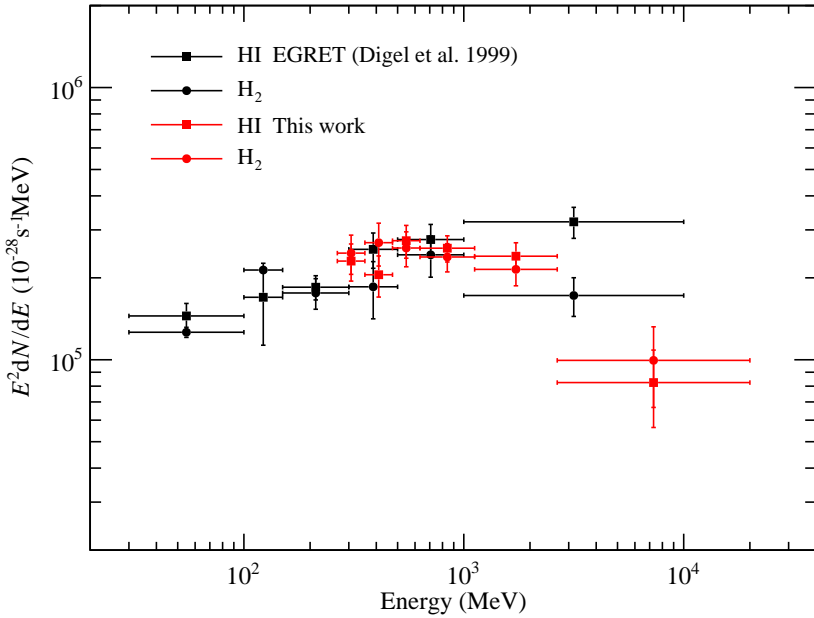


Figure 6.1: A comparison of gamma-ray emissivity of H I and H₂ gases between EGRET (Digel et al., 1999) and this work. The second lowest energy point of H₂ of the EGRET shows a 2σ upper limit. Red filled circles are scaled with a nominal constant X_{CO} of 1.5×10^{20} .

6.2 Total Masses of the Orion Molecular Clouds

Total molecular masses, one of the basic properties of MCs, have been estimated under the assumption of a constant X_{CO} inside clouds. If we adopt the obtained X_{CO} of 2.11×10^{20} in the Orion A₊ region, the total mass in the region becomes $\sim 40\%$ larger than old estimations using X_{CO} of 1.5×10^{20} . Such an underestimation of mass is considered to have been routinely done when one uses only a CO map and a constant X_{CO} . Indeed, Boulanger et al. (1998) pointed out that the difference between total masses of MCs obtained from CO observations and IR dust observations independently, became an order of magnitude at maximum, because IR emissivity is independent from CO formation or excitation. Meanwhile, IR emissivity is strongly affected by the temperature of the host cloud, and its calibration is difficult. In fact, Dobashi et al. (2005) pointed out that ISM dust structure obtained from IR observations and visual extinction showed different IR to A_V ratio of up to ~ 3 .

The gamma-ray emission from ISM can be now explained by hadronic interactions between CRs and the gas without considering other emission mechanisms. Thus, we can estimate the total masses of MCs assuming their distances from the Earth and the CR flux at their position. Unlike CO or IR dust observations, gamma-ray emissivity is not affected by the gas condition. Thus, π^0 gamma-ray emission is expected to be a more reliable tool to estimate the masses of MCs.

In Table 6.1, the obtained masses are compared with those estimated by radio observations. What we can observe from the Earth is only surface brightness of gamma rays or the CO line emission. Thus, in both observations, calculated masses are proportional to the square of the assumed distance as shown in equation (5.11). In addition, the mass estimation by gamma-ray observations depends on assumed CR flux, while that by CO observations depends on an assumed X_{CO} . However, if the CR flux and X_{CO} are constant, the mass ratio between Orion A and Orion B should be constant even when using different observation techniques. In the present gamma-ray observations, we obtained 2.03 ± 0.38 as

Table 6.1: A comparison of the total masses of the Orion A and B clouds obtained by several authors. Only statistical errors are shown with our result. Values by Wilson et al. (2005) have been adjusted to a distance of 400 pc. They calculated the masses assuming a constant X_{CO} of 1.8×10^{20} and a scale factor 1.36 for He and metals. Their mass of Orion B is scaled by 0.85 because their boundary definition of Orion B is wider than that of ours. The results by the NANTEX observations of ^{12}CO and ^{13}CO by Mizuno et al. (2003) are listed, while the parameters (distance, X_{CO} , boundary) they used are unknown. Calculation by Cambrésy (1999) using an A_V map was scaled by $(400/500)^2$ to adjust the distance to 400 pc. Only the sum of the two cloud masses is available in the literature.

Orion A	Orion B	Method	Reference
$(78.1 \pm 8.4) \times 10^3 M_{400}$	$(38.4 \pm 5.8) \times 10^3 M_{400}$	Gamma rays	This work
$80.9 \times 10^3 M_{400}$	$53.0 \times 10^3 M_{400}$	^{12}CO	Wilson et al. (2005)
$79 \times 10^3 M_{\odot}$	$28 \times 10^3 M_{\odot}$	^{12}CO	Mizuno et al. (2003)
$62 \times 10^3 M_{\odot}$	$20 \times 10^3 M_{\odot}$	^{13}CO	Mizuno et al. (2003)
$192 \times 10^3 M_{400} (\text{A} + \text{B})$		A_V	Cambrésy (1999)

Table 6.2: Comparison of X_{CO}

Region	$X_{\text{CO}}(10^{20})$	Method	References
Orion A + B, Mono R2	2.6 ± 1.2	Gamma rays	Bloemen et al. (1984)
Orion A + B, Mono R2	1.35 ± 0.15	Gamma rays	Digel et al. (1999)
$ b < 10^\circ$	1.56 ± 0.05	Gamma rays	Hunter et al. (1997)
$5^\circ < b < 30^\circ$	1.8 ± 0.3	IR Dust	Dame et al. (2001)
Ursa Major & Camelopardalis	1.3 ± 0.2	IR Dust	Reach et al. (1998)
Orion A ($l > 212^\circ$)	$2.11 \pm 0.09 \pm 0.18$	Gamma rays	This work
Orion A ($l < 212^\circ$)	$1.58 \pm 0.05 \pm 0.13$	Gamma rays	This work
Orion B	$1.29 \pm 0.06 \pm 0.10$	Gamma rays	This work

the mass ratio between Orion A and B assuming constant CR fluxes in the region, while Wilson et al. (2005) obtained 1.53 assuming a constant X_{CO} of 1.8×10^{20} . The difference between gamma-ray and CO observations is due to the nonuniformity of X_{CO} inside the clouds. If we scale the total mass of Orion A and B obtained by Wilson et al. (2005) with a X_{CO} of 1.5×10^{20} , it becomes $111.6 \times 10^3 M_{400}$ which is consistent with our estimate of $(116.5 \pm 10.2) \times 10^3 M_{400}$.

6.3 Nonlinear Relation between CO and Gamma-Ray Intensities

X_{CO} has been calculated by “solving” equation (5.3) by many authors. Their methods can be separated into mainly two groups. The first one uses gamma-ray intensity and emissivities for $\Phi(l, b, E)$, $A(E)$, and $B(E)$, respectively, as was shown in Section 5.2. The other uses IR emissivity and IR dust maps instead. Each of them should be correct, if X_{CO} , gamma-ray emissivity, and IR emissivity are constant in ROIs. However, as we shown, the assumption of a constant X_{CO} is not appropriate even for a small scale (~ 50 pc), and therefore, we did not derive X_{CO} in the same method performed in the EGRET observations. Table 6.2 summarizes X_{CO} obtained by several authors using regions in the Solar vicinity.

Our analysis in Section 5.2 supports these listed typical values (see Table 5.3), and thus $X_{\text{CO}} \sim 1.5 \times 10^{20}$ works as a first approximation in the Solar vicinity to obtain an overview of MCs. However

we found that the assumption of a constant X_{CO} in a MC was not necessarily correct.

6.3.1 CO vs. A_V

There are some possibilities that explain the nonlinear relation between the observed gamma-ray intensity and W_{CO} distribution. One of them is that there exists thin gas region which is not traced by the CO map but by A_V . We found that the correlation between gamma-ray intensity and A_V shows better linear relation compared to that of CO, and that the significance distribution of gamma-ray excess in the Orion A clouds which is not predicted by CO observations, is similar to the structure of the Orion A₊ region traced by A_V . Therefore, the nonlinear relation between the gamma-ray count and W_{CO} is partially explained by the A_V map and the possible existence of thin gas not detected by CO observations. In the thin tail of the Orion clouds, formation or excitation of CO molecules are considered to be not fully progressed.

6.3.2 Point source contribution

Point source contributions from unknown gamma-ray objects may explain the discrepancy as formerly discussed. It is not possible to estimate the contribution from weak point sources at unknown locations (we included them in the isotropic component in Chapter 5). Therefore, we surveyed positions of gamma-ray point source candidates. Figure 6.2 shows X-ray images of the Orion region obtained by three different X-ray telescopes; *Swift/BAT* (Tueller et al., 2008), ROSAT PSPC (Voges et al., 1999), and RXTE (Revnivtsev et al., 2004). These surveys cover the energy range between 0.1 keV and 195 keV. Their results show that there exist only 4 major X-ray sources in the region; the Orion A core, the Orion B core, and two Seyfert galaxies. The X-ray emission from MC cores is considered to be due to hot plasma, and thus is not related to gamma-ray emission. Nonexistence of an X-ray counterpart at the positive excess region does not necessarily mean that there is not a strong gamma-ray point source inside the clouds. However, the X-ray surveys are supporting materials decreasing the possibility of a point source contamination.

In addition to known X-ray sources, we surveyed several astronomical catalogs including potential gamma-ray sources; Blazars (Healey et al., 2008), SNRs (Green, 2009), low-mass X-ray binaries (Liu et al., 2007), high-mass X-ray binaries (Liu et al., 2006), pulsars (Manchester et al., 2005), and pulsar wind nebulae (Roberts, 2004). None of them overlaps the Orion clouds except for PMN J0542-0013.

With current limited photon statistic and the LAT PSF, we cannot extract weak point sources inside the clouds, even if they exist. However, the fact that there exists no gamma-ray candidate in the clouds is important, and thus we may ignore the contributions from undetected point sources for the present.

6.3.3 Nonuniformity of Cosmic Rays

We still cannot explain the nonlinearity in dense gas regions (cores of Orion A and B), i.e. $y \gtrsim 50$ data in Figure 5.16. If the formation and excitation of CO is fully developed around these cores, the data of dense regions should be fitted with a linear function. Let us consider possibilities which can explain this problem.

First, the CO line is known to be optically thick inside dense MC cores, and hence other emission lines such as ^{13}CO ($J = 1 - 0$) have been used to study such regions. However, if we take into account the optical thickness, the discrepancy from a liner relation at the cores of Orion A and B will become larger. As shown in Figures 5.24a and 5.24b, the predicted emission from the Orion B core is more intense than that of Orion A, while the observed intensity shows the opposite. Thus, brighter Orion B will become more bright, and optical-depth correction will not explain the discrepancy.

The second possibility is photodissociation of CO due to ultraviolet photons emitted from young stars inside MC cores. Quantitative estimation of this effect is not trivial. However, since W_{CO} at the

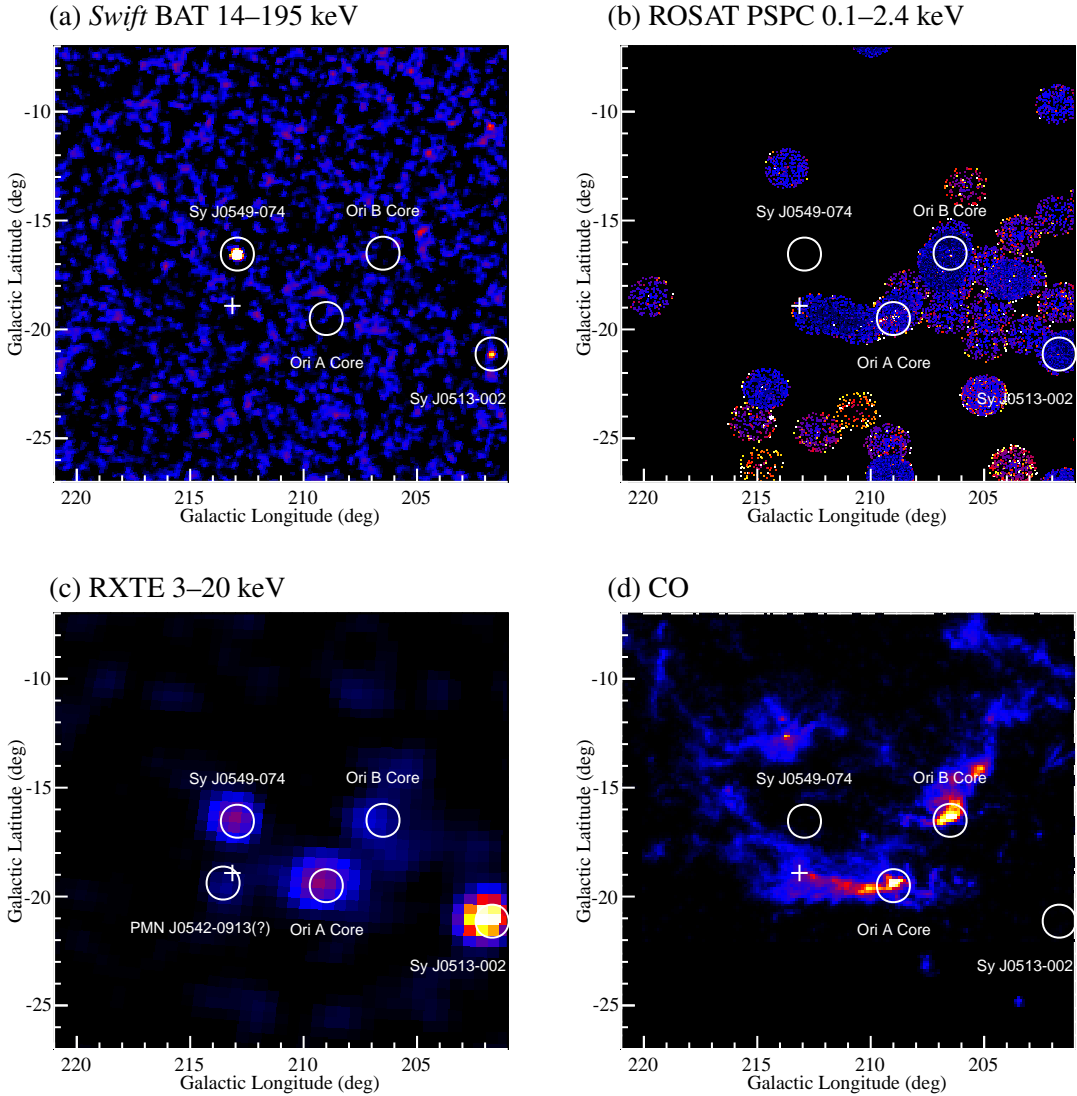


Figure 6.2: X-ray observations of the Orion region. The white cross shows the best fit position of the point source “candidate” obtained in Section 5.5.5. (a) The *Swift/BAT* image in the energy range of 14–195 keV (Tueller et al., 2008). Two Seyfert galaxies (Sy J0549-074 and Sy J0513-002) are bright. On the contrary, the cores of the Orion clouds are dark in this hard X-ray band. (b) The *ROSAT PSPC* image in the energy range of 0.1–2.4 keV (Voges et al., 1999). Young stars in the cores emit soft X-rays. (c) The *RXTE* image in the energy band of 3–20 keV (Revnivtsev et al., 2004). The two Seyfert galaxies and the cores are both bright. The position of a blazer PMN J0542-0913 is also overlaid. (d) A CO image as a reference (Dame et al., 2001)

cores of Orion A and B are comparable level ($\sim 200 \text{ K km s}^{-1}$), the effect inside them will be to similar extent, and will not explain the discrepancy either.

The third possibility is nonuniformity of the CR density inside MCs. Uniformity or nonuniformity of the CR density inside MCs have been discussed by several authors. For example, Dogiel et al. (2005) proposed a possibility of CR acceleration inside MCs. Magnetic reflection of CRs inside MCs was discussed by Aharonian (2001) to explain the “GeV excess”. Although there is not an established theoretical prediction of CR propagation inside MCs, non-uniform CR density inside MCs is possible. On the contrary, theoretical calculations of cosmic-ray reflection by strong magnetic fields inside molecular clouds were also performed by Cesarsky & Völk (1978) and Chandran (2000). Their conclusions are that cosmic rays can enter dense clouds and keep their spectral shapes and density. However, the actual CR distribution, especially in the most dense regions such as the cores of Orion A and B, is still unknown. There is no observational study showing CR nonuniformity or uniformity at the $\sim 50 \text{ pc}$ scale.

To examine if CR reflection can be seen in our data, we created a gamma-ray count map of energies above 1 GeV as shown in Figure 6.3, where we used only events converted in “thin” layers of the LAT tracker. By using only “thin”-layer events, the PSF is improved to $\sim 0.2^\circ$. The Figure is binned into $0.2^\circ \times 0.2^\circ$ pixels. Although statistical fluctuation in the Figure is rather large, we can see the structure of the Orion A and B clouds, and see count excesses corresponding to MC cores. However, the Orion B core (indicated with a green arrow) is $\sim 0.2^\circ$ away from the highest count region (the two adjacent pixels of 9 counts). The current limited photon statistics does not allow us to conclude that CRs cannot penetrate into dense MC cores. However, this remains as one possibility to explain the nonlinearity between the gamma-ray and CO intensity.

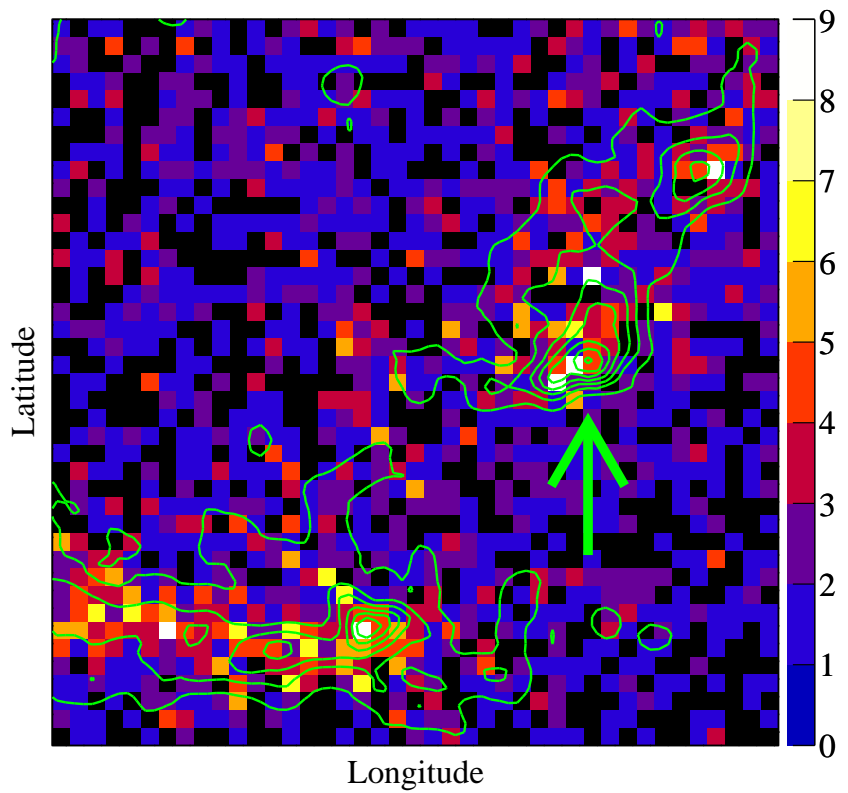


Figure 6.3: The observed gamma-ray count map using only “thin”-layer events of the energies above 1 GeV. Green contours show W_{CO} in 20 K km s^{-1} intervals.

Chapter 7

CONCLUSION

In the present thesis, we analyzed the Orion region using the *Fermi*/LAT data of gamma-ray observations. The obtained results are summarized as follows.

1. Diffuse gamma-ray emission in the energy range between 200 MeV and 20 GeV is well explained by an emissivity prediction using the most up-to-date calculation based on a π^0 model, a survey data of H I gas, and interstellar CR spectra at the Solar system predicted by GALPROP. Normalizing the obtained data with the predicted model, we obtained a best-fit normalization of $92 \pm 5\%$ ($\chi^2/\text{ndf} = 5.32/5$). It shows $8 \pm 5\%$ less gamma-ray emissivity than that at the Earth, while the assumed CR spectra, π^0 model, and H I observations are all thought to have systematic errors of $\sim 10\%$. The result shows that the CR spectra and fluxes ever observed at the Earth are not special, but typical ones in the Galaxy. The “GeV excess” seen in the EGRET observations is considered to be an instrumental effect.
2. The spectral shapes of gamma rays from the Orion A and B clouds are also consistent with π^0 emission model. Thus, the π^0 emission can be used to calculate the total masses of molecular clouds. Assuming interstellar CR fluxes at the locations of the clouds, we obtained their integrated masses to be

$$M_A = (78.1 \pm 8.4_{(\text{stat})} \pm 4.9_{(\pi^0)} \pm 0.4_{(\text{Brems})}) \times 10^3 M_\odot \quad (7.1)$$

$$M_B = (38.4 \pm 5.8_{(\text{stat})} \pm 2.9_{(\pi^0)} \pm 0.2_{(\text{Brems})}) \times 10^3 M_\odot, \quad (7.2)$$

where the distances to the clouds are assumed to be 400 pc. Due to the nonuniformity of X_{CO} , we observed $\sim 50\%$ higher mass density in the outskirts of the Orion A cloud than the expected mass from CO observations.

3. The obtained masses are consistent with previous works based on CO observations. However, the spatial distribution of the observed gamma-ray intensity is not in a simple linear relation with that of CO intensity assuming a constant conversion factor of 1.5×10^{20} . The best-fit slopes for their correlations in different three regions are given by

$$p_{1,A+} = 0.71 \pm 0.03_{(\text{stat})} \pm 0.06_{(\pi^0)} \pm 0.00_{(\text{Brems})} \quad (7.3)$$

$$p_{1,A-} = 0.95 \pm 0.03_{(\text{stat})} \pm 0.08_{(\pi^0)} \pm 0.01_{(\text{Brems})} \quad (7.4)$$

$$p_{1,B} = 1.16 \pm 0.05_{(\text{stat})} \pm 0.09_{(\pi^0)} \pm 0.00_{(\text{Brems})}. \quad (7.5)$$

Thus, our simple assumption of a constant conversion factor or a uniform CR density is not correct.

4. We studied correlations between the gamma-ray intensity and a visual extinction (A_V) map, and found that best-fit slopes were almost constant in the three region, while they showed nonlinear

relations in dense region ($A_V > 2$). Therefore, at least in thin gas regions, both gamma-ray and A_V observations are able to trace gas which are not detected by CO observations. The formation or excitation of CO is considered to be not fully progressed in such regions.

5. The nonlinearity in dense MC cores is still not explained by item 4. This may be explained by exclusion of CRs inside dense MC cores, while current limited photon statistics does not allow us to examine this effect in detail.

APPENDIX

A Kinematics

A.1 Threshold kinetic energy for pion production

The threshold kinetic energy E_{th} of the incident proton in a p - p collision that produces only one pion, can be converted to the mass of the pion in the center of mass system (CMS). Since \sqrt{s} is conserved in Lorentz transformations between the CMS and the laboratory system (LS), following equations are equal.

$$\begin{aligned} s_{\text{CMS}} &= (m_\pi + 2m_p)^2 \\ s_{\text{LS}} &= \{(E_{\text{th}} + m_p) + m_p\}^2 - \left\{ \sqrt{(E_{\text{th}} + m_p)^2 - m_p^2} \right\}^2, \end{aligned} \quad (\text{A.1})$$

therefore we obtain

$$E_{\text{th}} = 2m_\pi \left(1 + \frac{m_\pi}{4m_p} \right) = \begin{cases} 279.7 \text{ MeV} & \text{for } \pi^0 \\ 289.5 \text{ MeV} & \text{for } \pi^\pm \end{cases}. \quad (\text{A.2})$$

A.2 Gamma-ray energy distribution in π^0 decay

Two gamma rays created in a π^0 decay have same momenta in opposite directions in the CMS of the π^0 . Their angular distribution in the CMS is isotropic and therefore the differential cross section is constant in $\cos \theta$ space

$$\frac{d\sigma}{d(\cos \theta)} = \text{constant}, \quad (\text{A.3})$$

where θ is separation angle between the direction of π^0 momentum in the LS and the photon momenta in the CMS.

The energy of two photons are equal to $m_{\pi^0}/2$ in the CMS. Therefore they can be written as below in the LS after Lorentz transformation.

$$\begin{aligned} E_1 &= \gamma_{\pi^0} \left(\frac{m_{\pi^0}}{2} + \beta_{\pi^0} \cos \theta \frac{m_{\pi^0}}{2} \right) \\ E_2 &= \gamma_{\pi^0} \left(\frac{m_{\pi^0}}{2} - \beta_{\pi^0} \cos \theta \frac{m_{\pi^0}}{2} \right), \end{aligned} \quad (\text{A.4})$$

where E_1 and E_2 are boosted photon energies, γ_{π^0} and β_{π^0} are the γ factor and the speed of the π^0 .

From equation (A.3) and (A.4), we obtain following relations.

$$\frac{dN}{dE} = \text{constant} \quad (\text{A.5})$$

$$\begin{aligned}
\frac{\log E_{\max} + \log E_{\min}}{2} &= \frac{\log \gamma_{\pi^0} \frac{m_{\pi^0}}{2} (1 + \beta_{\pi^0}) + \log \gamma_{\pi^0} \frac{m_{\pi^0}}{2} (1 - \beta_{\pi^0})}{2} \\
&= \log \frac{m_{\pi^0}}{2} \\
&= \log(67.5 \text{ MeV})
\end{aligned} \tag{A.6}$$

Therefore the energy distribution of π^0 -decay gamma rays is always symmetric in $\log E$ scale around $\log E = \log(67.5 \text{ MeV})$ (see figure 2.9).

B Maximum Likelihood Method

Maximum likelihood method has been used in the field of gamma-ray astrophysics, due to the limited photon statistic and the strong energy dependence of the instrumental response of celestial gamma-ray detectors (Mattox et al., 1996). This technique maximizes the “likelihood” to obtain the spectral information of gamma-ray sources instead of calculating χ^2 .

The source model function of gamma-ray flux, $S(E, \hat{p})$ at each celestial coordinates \hat{p} , can be written as

$$S(E, \hat{p}, t) = \sum_i s_i(E, t) \delta(\hat{p} - \hat{p}_i) + S_{\text{BG}}(E, \hat{p}, t), \tag{B.7}$$

where E is energy, t is time, $s_i(E, t)$ is the flux of the i th point source, δ is delta function, and S_{BG} is diffuse emission. In a practical case, this function must be folded with the instrumental response function $R(E', \hat{p}'; E, \hat{p})$ as follows.

$$M(E', \hat{p}', t) = \int_{\text{SR}} dE d\hat{p} R(E', \hat{p}', t; E, \hat{p}) S(E, \hat{p}, t), \tag{B.8}$$

where

$$R(E', \hat{p}', t; E, \hat{p}) = A(E, \hat{p}, \vec{L}(t)) D(E'; E, \hat{p}, \vec{L}(t)) P(\hat{p}'; E, \hat{p}, \vec{L}(t)). \tag{B.9}$$

A , D and P are affective area, energy dispersion and point spread function, respectively. SR denotes the source region containing all the sources that can contribute to the region of interest (ROI). $\vec{L}(t)$ is the direction of the space craft. If we analyze steady sources, t can be dropped from the flux terms in the above equations.

If we divide the space into small pixels, the expected photon count μ in a pixel can be written as

$$\mu = M(E', \hat{p}', t) \Delta E' \Delta \hat{p}' \Delta t. \tag{B.10}$$

Thus the probability of detecting n photons inside the pixel, upon an assumption of a Poisson random process, can be written as

$$P(n; \mu) = \frac{\mu^n e^{-\mu}}{n!}. \tag{B.11}$$

Our aim is to optimize the source model S to maximize this probability, and thus we introduce a joint probability called likelihood \mathcal{L} , and log likelihood $\ln \mathcal{L}$.

$$\begin{aligned}
\mathcal{L} &= \prod_i P_i(n_i; \mu_i) \\
\ln \mathcal{L} &= \sum_i \ln P_i(n_i; \mu_i) \\
&= \sum_i \{n_i \ln(M_i \Delta E' \Delta \hat{p}' \Delta t) - M_i \Delta E' \Delta \hat{p}' \Delta t - \ln(n_i!)\} \\
&= \sum_i \{n_i \ln(M_i \Delta E' \Delta \hat{p}' \Delta t) - \ln(n_i!)\} - N_{\text{pred}},
\end{aligned} \tag{B.12}$$

where i denotes the pixel number and N_{pred} is the number of predicted photons. In the limit of infinitesimal pixel size, n is always 0 or 1. Therefore $\ln \mathcal{L}$ can be simplified as

$$\ln \mathcal{L} = \sum_j M_j(E'_j, \hat{p}'_j, t_j) - N_{\text{pred}}, \quad (\text{B.13})$$

where j denotes the event numbers.

Since \mathcal{L} is a function of model parameters $\vec{\lambda}$, obtaining the maximum log likelihood is to find a set of parameters which satisfies

$$\frac{\partial \ln \mathcal{L}}{\partial \vec{\lambda}} = 0 \quad (\text{B.14})$$

in the parameter space.

In an analysis of a point source, our interests are to know how significant the source detection is and how uncertain the estimate of the source flux. The significance of the detection of the source is given by a comparison between two models; A null hypothesis H_0 which does not include the source, and an alternative hypothesis H_1 in which there is the source. The test statistic TS between H_0 and H_1 is given by

$$\text{TS} \equiv 2(\ln \mathcal{L}_1 - \ln \mathcal{L}_0), \quad (\text{B.15})$$

where \mathcal{L}_1 and \mathcal{L}_0 are the likelihood of H_1 and H_0 , respectively. By Wilks's theorem, the probability of TS is known to be asymptotically distributed as χ^2 in H_1 (Wilks, 1938) if the number of photons being studied is $\gtrsim 20$ (Mattox et al., 1996). Thus $\text{TS}^{1/2}$ can be used as a measure of the significance in the source detection analysis. $\text{TS} = 25$ is an equivalent of 5σ detection.

C Results of *gtlike*

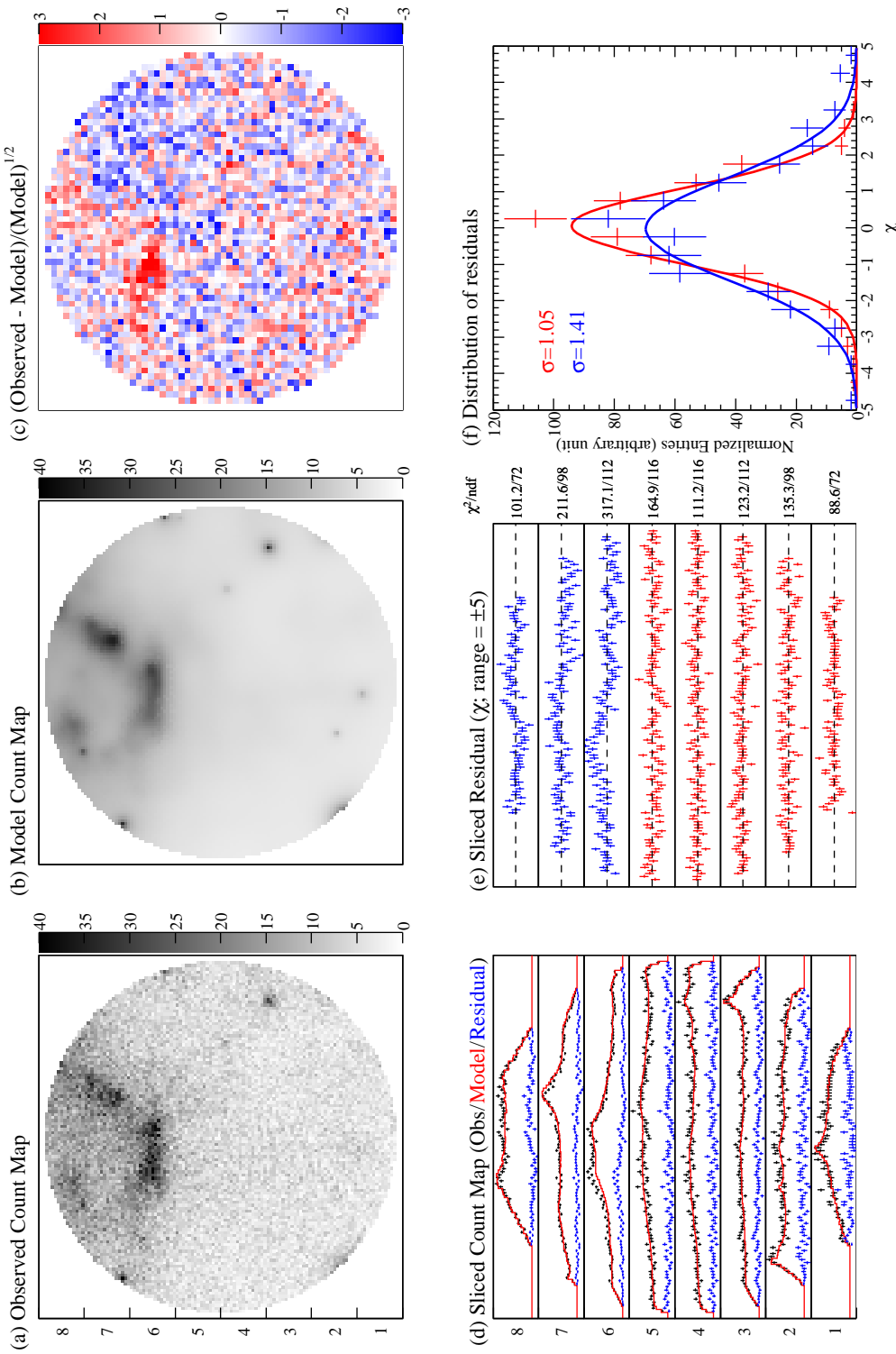


Figure C.1: Results of the *gtlike* analysis of the data set 2, using the model “54_78Xvarh7O”.

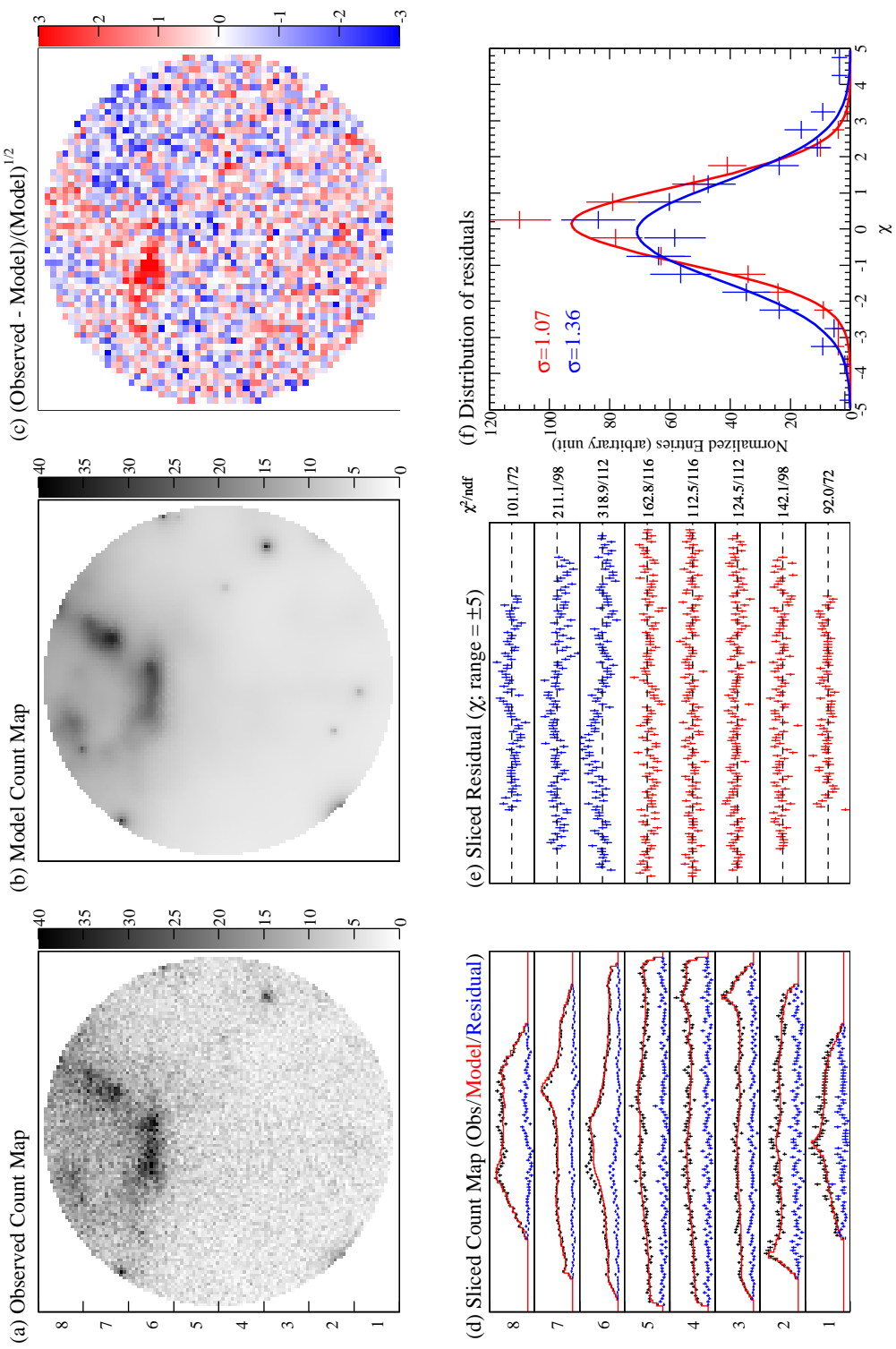


Figure C.2: Results of the *gtlike* analysis of the data set 2, using the model “54_78Xvar7O”. The normalization of the IC component was set free.

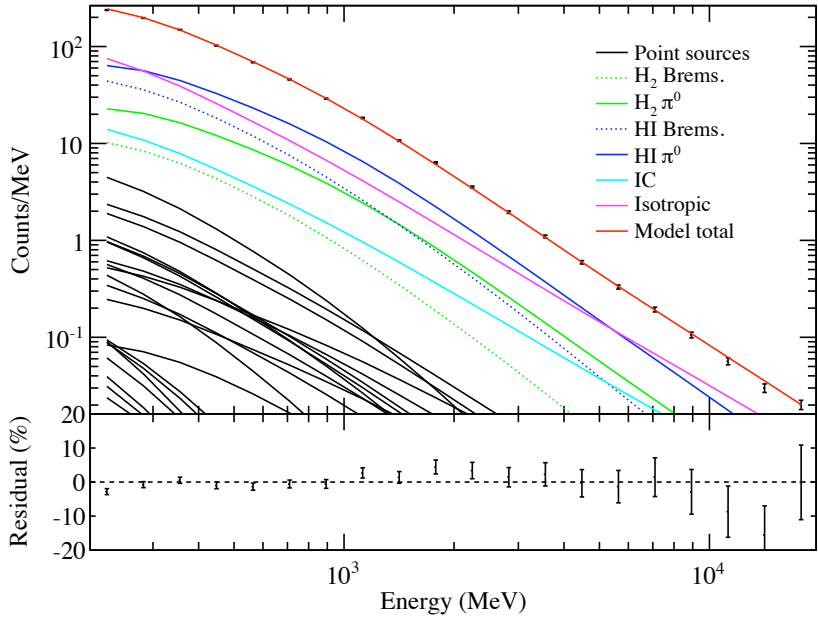


Figure C.3: The total count spectrum of the data set 2 (black dots), compared with the best-fit model (red curve) including “54_78Xvarh7O” (black dashed curve). The counts are not corrected for the exposure.

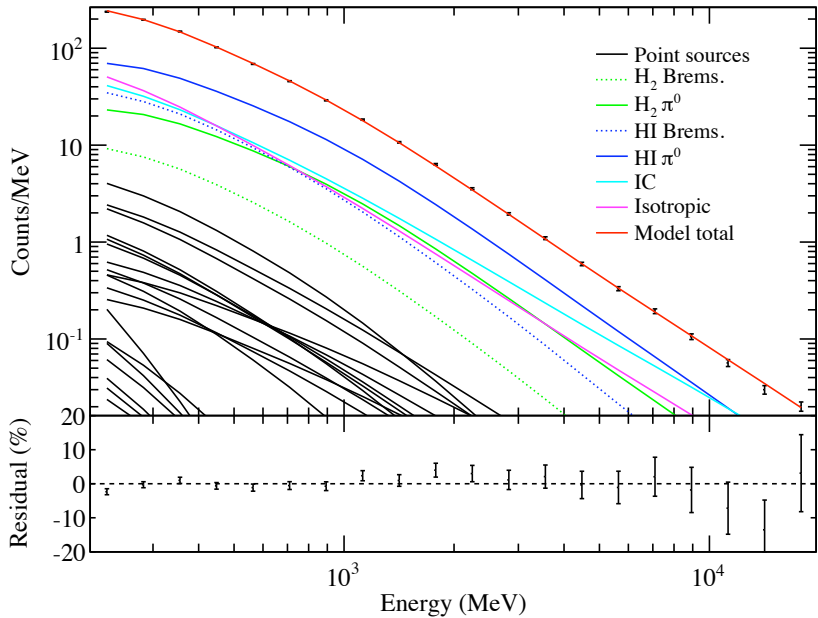


Figure C.4: The total count spectrum of the data set 2 (black dots), compared with the best-fit model (red curve) including “54_78Xvarh7O” (black dashed curve). The counts are not corrected for the exposure. The normalization of the IC component was set free.

Table C.1: A likelihood result of “54_78Xvarh7O_Ts100”.

Component	Normalization	N_0 ($10^{-7} \text{cm}^{-2}\text{s}^{-1}\text{sr}^{-2}\text{MeV}^{-1}$)	γ
π^0 (H I)	1.106 ± 0.005	–	–
π^0 (H ₂)	1.043 ± 0.009	–	–
Bremsstrahlung (H I)	1.402 ± 0.016	–	–
Bremsstrahlung (H ₂)	0.916 ± 0.028	–	–
Isotropic	–	1.976 ± 0.011	2.279 ± 0.003

Table C.2: A likelihood result of “54_78Xvarh7O_Ts100000”.

Component	Normalization	N_0 ($10^{-7} \text{cm}^{-2}\text{s}^{-1}\text{sr}^{-2}\text{MeV}^{-1}$)	γ
π^0 (H I)	1.189 ± 0.012	–	–
π^0 (H ₂)	1.025 ± 0.004	–	–
Bremsstrahlung (H I)	2.581 ± 0.009	–	–
Bremsstrahlung (H ₂)	1.299 ± 0.006	–	–
Isotropic	–	1.577 ± 0.023	2.238 ± 0.005

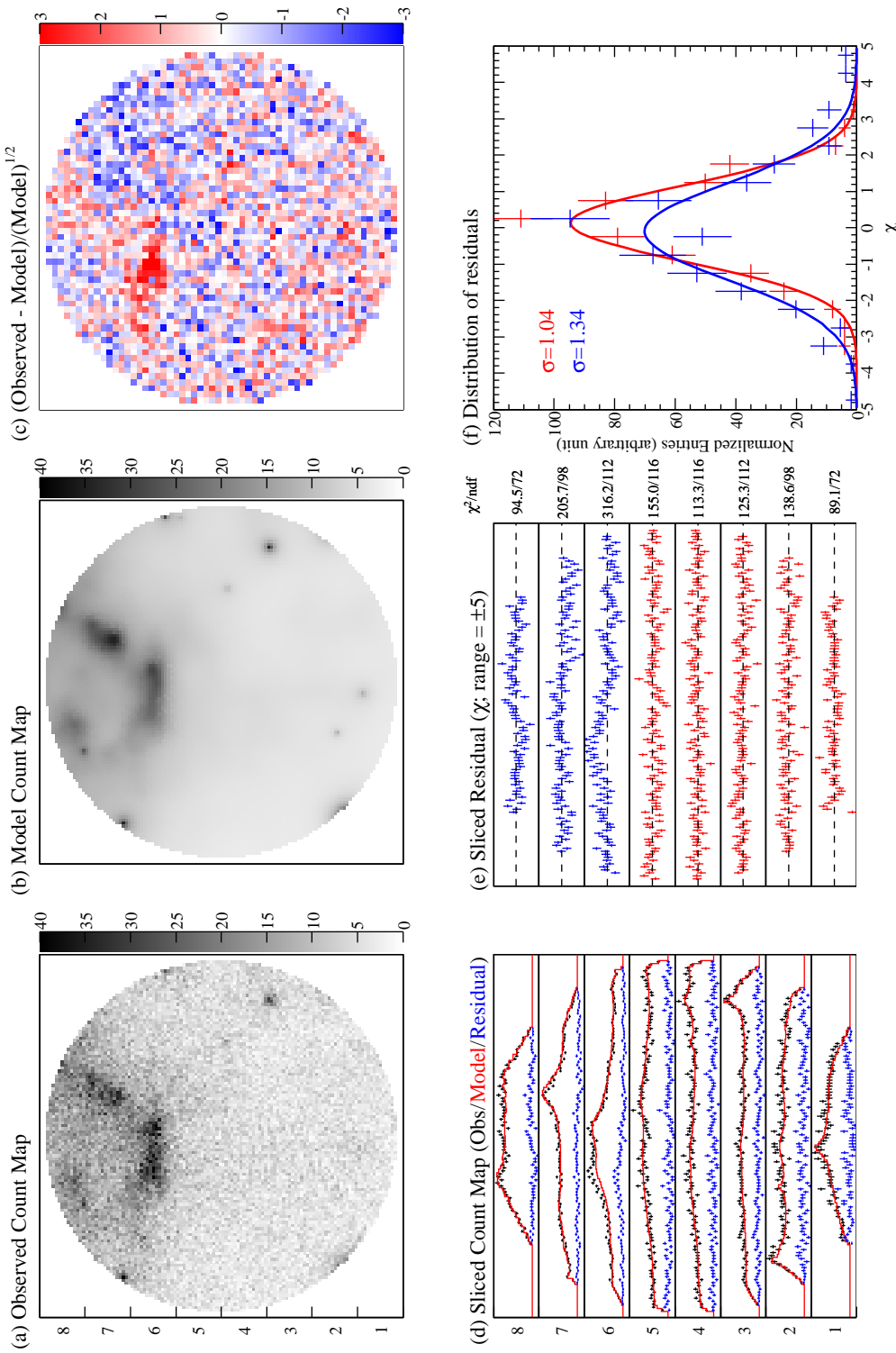


Figure C.5: Results of the *gtlike* analysis of the data set 2, using the model “54_78Xvarh7O_Ts100”.

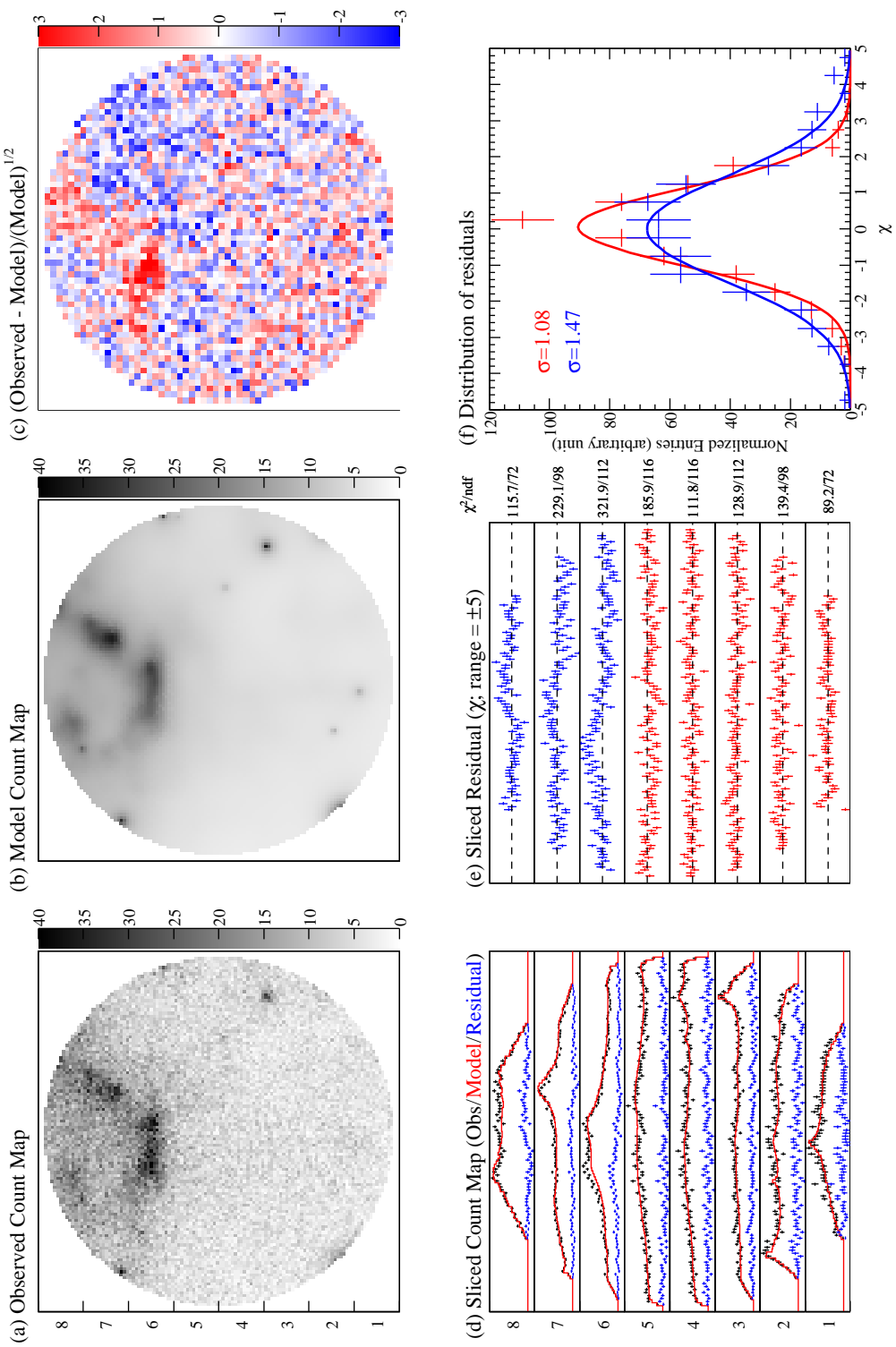


Figure C.6: Results of the *gtlike* analysis of the data set 2, using the model “54_78Xvarh7O_Ts100000”.

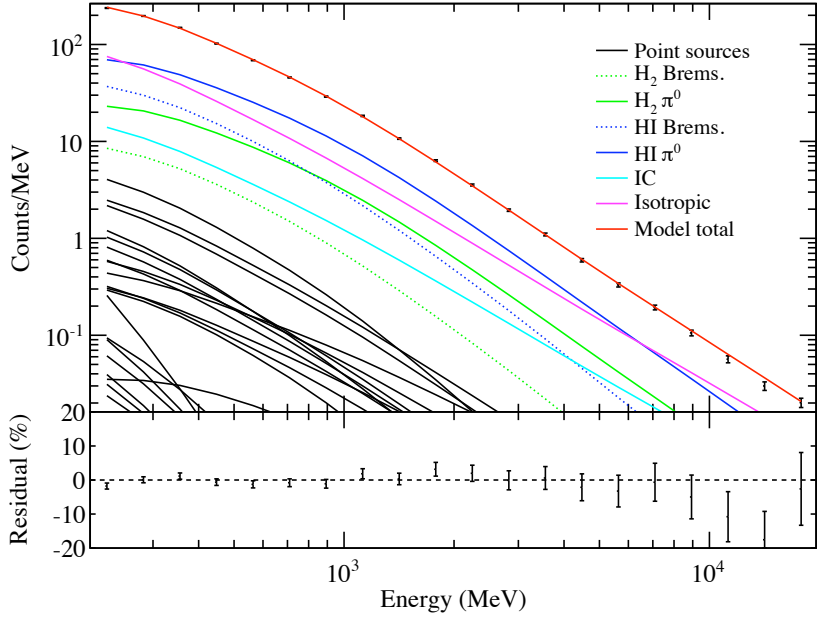


Figure C.7: The total count spectrum of the data set 2 (black dots), compared with the best-fit model (red curve) including “54_78Xvarh7O_Ts100” (black dashed curve). The counts are not corrected for the exposure. The normalization of the IC component was set free.

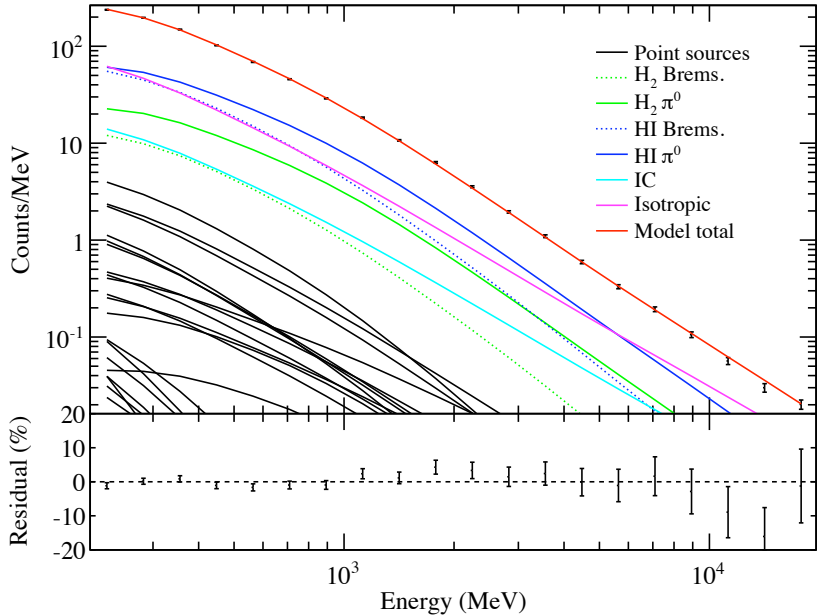


Figure C.8: The total count spectrum of the data set 2 (black dots), compared with the best-fit model (red curve) including “54_78Xvarh7O_Ts100000” (black dashed curve). The counts are not corrected for the exposure. The normalization of the IC component was set free.

Acknowledgement

It is a pleasure to thank the many people who made this thesis possible. I wish to express my gratitude, first, to my supervisor Prof. Kazuo Makishima for his continuous support and encouragement during this research. At many stages, I benefited from his advice and discussions on physics and data analyses. His careful editing greatly improved this thesis.

I would like to thank Prof. Tune Kamae (SLAC) who first suggested me to choose the theme of this thesis. I have learned many things from his inspired insight into physics and astronomy. He offered me a very comfortable environment for my research at SLAC.

I wish thank to Dr. Kazuhiro Nakazawa and all the students in Makishima-Nakazawa group. They have supported my research since the first days in the group.

I would also like to thank Prof. Yasushi Fukazawa, Dr. Tsunefumi Mizuno, Dr. Hide Katagiri, Dr. Hiromitsu Takahashi (Hiroshima Univ.), Dr. Hiro Tajima, Dr. Seth Digel, Dr. Markus Ackermann, Dr. Yasunobu Uchiyama, Dr. Masaaki Hayashida, Dr. Takaaki Tanaka (SLAC), and Dr. Masanori Ohno (ISAS/JAXA) in the *Fermi*/LAT collaboration. Their advice and discussions enormously improved my understanding of astrophysics and data analyses of the LAT data.

I am grateful to Dr. Andrew Strong (Max-Planck) and Dr. Igor Moskalenko (Stanford) who provided me the source code of GALPROP. Sharing their deep knowledge about cosmic-ray physics and gamma-ray astronomy was very helpful.

To my family, whom I am eternally indebted to for everything you have provided and done for me with unreserved selflessness in order for me to achieve my aspirations. You have given me the tools to succeed and without your enduring commitment to me, this thesis would not have been possible. I am grateful that you have been the backbone of my support and I sincerely give you all my praise and gratitude.

Finally, to my wife, I dedicate this thesis to you, in an effort to express my gratitude for all your unconditional support you have shown me. The patience you demonstrated and the sacrifices you made so that I could complete this research are never taken for granted. I am truly blessed to have you in my life and will continue to show you the same dedication and love which you have shown me.

References

- Abbasi, R. U., et al. 2008, Phys. Rev. Lett., 100, 101101
- Abdo, A. A., et al. 2009a, in preparation
- . 2009b, arXiv:0904.2226
- . 2009c, Astrophys. Jour. Suppl. Ser., 183, 46
- . 2009d, Phys. Rev. Lett., 102, 181101
- Aharonian, F., et al. 2008, Phys. Rev. Lett., 101, 261104
- . 2007, Astron. Astrophys., 464, 235
- Aharonian, F. A. 2001, Space Sci. Rev., 99, 187
- Aharonian, F. A., et al. 2004, Nature, 432, 75
- . 2009, arXiv:0905.0105
- Alcaraz, J., et al. 2000a, Phys. Lett. B, 490, 27
- . 2000b, Phys. Lett. B, 494, 193
- . 2000c, Phys. Lett. B, 484, 10
- Alves, J. F., Lada, C. J., & Lada, E. A. 2001, Nature, 409, 159
- Amsler, C., et al. 2008, Phys. Lett. B, 667, 1
- Apanasenko, A. V., et al. 2001, Astropar. Phys., 16, 13
- Arimoto, N., Sofue, Y., & Tsujimoto, T. 1996, Pub. Astron. Soc. Japan, 48, 275
- Ashmore, A., Cocconi, G., Diddens, A. N., & Wetherell, A. M. 1960, Phys. Rev. Lett., 5, 576
- Atwood, W. B. 1993, NASA STI/Recon Technical Report N, 94, 27740
- Atwood, W. B. 1994, Nucl. Instr. Meth. Phys. Res. A, 342, 302
- Atwood, W. B., et al. 2009, Astrophys. Jour., 697, 1071
- . 2000, Nucl. Instr. Meth. Phys. Res. A, 446, 444
- Barwick, S. W., et al. 1998, Astrophys. Jour., 498, 779
- Bell, A. R. 1978, Mon. Not. R. Astron. Soc., 182, 147

- Belli, F., et al. 2007, Nucl. Instr. Meth. Phys. Res. A, 570, 276
- Bellotti, R., et al. 1999, Phys. Rev. D, 60, 052002
- Berezhko, E. G., & Volk, H. J. 2004, Astrophys. Jour., 611, 12
- Białas, A., Bleszyński, M., & Xzyż, W. 1976, Nucl. Phys. B, Part. Phys., 111, 461
- Blandford, R. D., & Ostriker, J. P. 1978, Astrophys. Jour., 221, L29
- Bloemen, J. B. G. M. 1985, Astron. Astrophys., 145, 391
- Bloemen, J. B. G. M., Caraveo, P. A., Hermsen, W., Lebrun, F., Maddalena, R. J., Strong, A. W., & Thaddeus, P. 1984, Astron. Astrophys., 139, 37
- Boezio, M., et al. 2000, Astrophys. Jour., 532, 653
- Boulanger, F., Bronfman, L., Dame, T. M., & Thaddeus, P. 1998, Astron. Astrophys., 332, 273
- Cambrésy, L. 1999, Astron. Astrophys., 345, 965
- Caraveo, P. A., et al. 1980, Astron. Astrophys., 91, L3
- Carruthers, G. R. 1970, Astrophys. Jour., 161, L81
- Cesarsky, C. J., & Völk, H. J. 1978, Astron. Astrophys., 70, 367
- Chandran, B. D. G. 2000, Astrophys. Jour., 529, 513
- Clark, G. W., Garmire, G. P., & Kraushaar, W. L. 1968, Astrophys. Jour., 153, L203
- Cronin, J. W., Gaisser, T. K., & Swordy, S. P. 1997, Scientific American, 276, 32
- Dame, T. M., Hartmann, D., & Thaddeus, P. 2001, Astrophys. Jour., 547, 792
- Dame, T. M., et al. 1987, Astrophys. Jour., 322, 706
- de Boer, W., Sander, C., Zhukov, V., Gladyshev, A. V., & Kazakov, D. I. 2005, Astron. Astrophys., 444, 51
- Dermer, C. D. 1986, Astron. Astrophys., 157, 223
- Dickey, J. M., & Lockman, F. J. 1990, Ann. Rev. Astron. Astrophys., 28, 215
- Digel, S. W., Aprile, E., Hunter, S. D., Mukherjee, R., & Xu, F. 1999, Astrophys. Jour., 520, 196
- Digel, S. W., Hunter, S. D., & Mukherjee, R. 1995, Astrophys. Jour., 441, 270
- do Couto e Silva, E., et al. 2001, Nucl. Instr. Meth. Phys. Res. A, 474, 19
- Dobashi, K., Uehara, H., Kandori, R., Sakurai, T., Kaiden, M., Umemoto, T., & Sato, F. 2005, Pub. Astron. Soc. Japan, 57, S1
- Dogiel, V. A., Gurevich, A. V., Istomin, Y. N., & Zybin, K. P. 2005, Astrophys. Space. Sci., 297, 201
- Esposito, J. A., Hunter, S. D., Kanbach, G., & Sreekumar, P. 1996, Astrophys. Jour., 461, 820
- Ewen, H. I., & Purcell, E. M. 1951, Nature, 168, 356

- Fermi, E. 1949, Physical Review, 75, 1169
- Ferrière, K. M. 2001, Rev. Mod. Phys., 73, 1031
- Frühwirth, R. 1987, Nucl. Instr. Meth. Phys. Res. A, 262, 444
- Funk, S. 2008, Adv. Space Res., 41, 464
- Gaisser, T. K. 1990, Cosmic Rays and Particle Physics (Cambridge University Press)
- Gaisser, T. K., & Schaefer, R. K. 1992, Astrophys. Jour., 394, 174
- Ginzburg, V. L., & Syrovatskii, S. I. 1964, The Origin of Cosmic Rays (Oxford : Pergamon Press)
- Gleeson, L. J., & Axford, W. I. 1968, Astrophys. Jour., 154, 1011
- Green, D. A. 2009, A Catalogue of Galactic Supernova Remnants (2009 March version)
- Greiner, I. A., Casandjian, J.-M., & Terrier, R. 2005, Science, 307, 1292
- Haino, S., et al. 2004, Phys. Lett. B, 594, 35
- Hartman, R. C., et al. 1999, Astrophys. Jour., 123, 79
- Healey, S. E., et al. 2008, Astrophys. Jour., 175, 97
- Heiles, C. 1976, Ann. Rev. Astron. Astrophys., 14, 1
- Hess, V. F. 1912, Physikalische Zeitschrift, 13, 1084
- Hillas, A. M. 2005, Journal of Physics G: Nuclear and Particle Physics, 31, R95
- Hirota, T., et al. 2007, Pub. Astron. Soc. Japan, 59, 897
- Huang, C.-Y., Park, S.-E., Pohl, M., & Daniels, C. D. 2007, Astropar. Phys., 27, 429
- Hunter, S. D., et al. 1997, Astrophys. Jour., 481, 205
- Kalberla, P. M. W., Burton, W. B., Hartmann, D., Arnal, E. M., Bajaja, E., Morras, R., & Pöppel, W. G. L. 2005, Astron. Astrophys., 440, 775
- Kalman, R. E. 1960, Transactions of the ASME Journal of Basic Engineering, 82, 34
- Kamae, T., Karlsson, N., Mizuno, T., Abe, T., & Koi, T. 2006, Astrophys. Jour., 647, 692
- Kelner, S. R., Aharonian, F. A., & Bugayov, V. V. 2006, Phys. Rev. D, 74, 034018
- Kerr, F. J., & Lynden-Bell, D. 1986, Mon. Not. R. Astron. Soc., 221, 1023
- Kim, M. K., et al. 2008, Pub. Astron. Soc. Japan, 60, 991
- Kniffen, D. A., Hartman, R. C., Thompson, D. J., Bignami, G. K., Fichtel, C. E., Turner, T., & Ogelman, H. 1974, Nature, 251, 397
- Koyama, K., Petre, R., Gotthelf, E., Hwang, U., Matsuura, M., Ozaki, M., & Holt, S. 1995, Nature, 378, 255
- Liu, Q. Z., van Paradijs, J., & van den Heuvel, E. P. J. 2006, Astron. Astrophys., 455, 1165

- . 2007, *Astron. Astrophys.*, 469, 807
- Manchester, R. N., Hobbs, G. B., Teoh, A., , & Hobbs, M. 2005, *Astron. Jour.*, 129, 1993
- Mattox, J. R., et al. 1996, *Astrophys. Jour.*, 461, 396
- Meegan, C., et al. 2007, in American Institute of Physics Conference Series, Vol. 921, The First GLAST Symposium, ed. S. Ritz, P. Michelson, & C. A. Meegan, 13–18
- Mellinger, A. 2008, Star Forming Regions along the Milky Way: A Panoramic View, ed. B. Reipurth (Astronomical Society of the Pacific), 1–18
- Menn, W., et al. 2000, *Astrophys. Jour.*, 533, 281
- Menten, K. M., Reid, M. J., Forbrich, J., & Brunthaler, A. 2007, *Astron. Astrophys.*, 474, 515
- Mizuno, N., Aoyama, H., Onishi, T., Mizuno, A., & Fukui, Y. 2003, in ASP Conference Series, ed. J. M. De Buizer & N. S. van der Blieck, Vol. 287, 47–51
- Mizuno, T., Kamae, T., Godfrey, G., Handa, T., Thompson, D. J., Lauben, D., Fukazawa, Y., & Ozaki, M. 2004, *Astrophys. Jour.*, 614, 1113
- Mori, M. 1997, *Astrophys. Jour.*, 478, 225
- . 2009, *Astropar. Phys.*, 31, 341
- Moskalenko, I. V., Digel, S. W., Porter, T. A., Reimer, O., & Strong, A. W. 2007, Nuclear Physics B - Proceedings Supplements, 173, 44 , proceedings of the 7th UCLA Symposium on Sources and Detection of Dark Matter and Dark Energy in the Universe, Proceedings of the 7th UCLA Symposium on Sources and Detection of Dark Matter and Dark Energy in the Universe
- Muller, C. A., & Oort, J. H. 1951, *Nature*, 168, 357
- Nakanishi, H., & Sofue, Y. 2003, *Pub. Astron. Soc. Japan*, 55, 191
- Naumann-Godó, M., Beilicke, M., Hauser, D., Lemoine-Goumard, M., & de Naurois, M. 2008, in High Energy Gamma-Ray Astronomy: Proceedings of the 4th International Meeting on High Energy Gamma-Ray Astronomy, ed. F. A. Aharonian, W. Hofmann, & F. Rieger, Vol. 1085, 304–307
- Orth, C. D., & Buffington, A. 1976, *Astrophys. Jour.*, 206, 312
- Panov, A. D., et al. 2007, *Bulletin of the Russian Academy of Sciences: Physics*, 71, 494
- Porter, T. A., Moskalenko, I. V., Strong, A. W., Orlando, E., , & Bouchet, L. 2008, *Astrophys. Jour.*, 682, 400
- Porter, T. A., & Protheroe, R. J. 1997, *Journal of Physics G: Nuclear and Particle Physics*, 23, 1765
- Reach, W. T., Wall, W. F., , & Odegard, N. 1998, *Astrophys. Jour.*, 507, 507
- Revnivtsev, M., Sazonov, S., Jahoda, K., & Gilfanov, M. 2004, *Astron. Astrophys.*, 418, 927
- Roberts, M. S. E. 2004, The Pulsar Wind Nebula Catalog (March 2005 version)
- Rybicki, G. B., & Lightman, A. P. 1979, Radiative processes in astrophysics (Wiley-Interscience)
- Sandstrom, K. M., Peek, J. E. G., Bower, G. C., Bolatto, A. D., & Plambeck, R. L. 2007, *Astrophys. Jour.*, 667, 1161

- Schlegel, D. J., Finkbeiner, D. P., & Davis, M. 1998, *Astrophys. Jour.*, 500, 525
- Shikaze, Y., et al. 2007, *Astropar. Phys.*, 28, 154
- Sreekumar, P., et al. 1998, *Astrophys. Jour.*, 494, 523
- Stecker, F. W. 1970, *Astrophys. Space. Sci.*, 6, 377
- Stone, E. C., Cummings, A. C., McDonald, F. B., Heikkila, B. C., Lal, N., & Webber, W. R. 2005, *Science*, 309, 2017
- Strong, A. W. 2009, Proc. 31st Int. Cosmic Ray Conf.
- Strong, A. W., Moskalenko, I. V., , & Reimer, O. 2004a, *Astrophys. Jour.*, 613, 962
- Strong, A. W., & Moskalenko, I. V. 1998, *Astrophys. Jour.*, 509, 212
- Strong, A. W., Moskalenko, I. V., & Reimer, O. 2000, *Astrophys. Jour.*, 537, 763
- Strong, A. W., Moskalenko, I. V., Reimer, O., Digel, S., & Diehl, R. 2004b, *Astron. Astrophys.*, 422, L47
- Takeda, M., et al. 2003, *Astropar. Phys.*, 19, 447
- Thompson, D., et al. 2002, *IEEE Trans. Nucl. Sci.*, 49, 1898
- Thompson, D. J., Bignami, G. F., Fichtel, C. E., & Kniffen, D. A. 1974, *Astrophys. Jour.*, 190, L51
- Thompson, D. J., Fichtel, C. E., Hartman, R. C., Kniffen, D. A., & Lamb, R. C. 1977, *Astrophys. Jour.*, 213, 252
- Tielens, A. G. G. M., & Hollenbach, D. 1985, *Astrophys. Jour.*, 291, 722
- Tueller, J., et al. 2008, *Astrophys. Jour.*, 681, 113
- Uchiyama, Y. 2003, PhD thesis, The University of Tokyo
- Uchiyama, Y., Aharonian, F. A., Tanaka, T., Takahashi, T., & Maeda, Y. 2007, *Nature*, 449, 576
- Voges, W., et al. 1999, *Astron. Astrophys.*, 349, 389
- Wilks, S. S. 1938, *Annals of Mathematical Statistics*, 9, 60
- Wilson, B. A., Dame, T. M., Masheder, M. R. W., & Thaddeus, P. 2005, *Astron. Astrophys.*, 430, 523
- Wilson, C. D. 1995, *Astrophys. Jour.*, 448, L97
- Wilson, R. W., Jefferts, K. B., & Penzias, A. A. 1970, *Astrophys. Jour.*, 161, L43